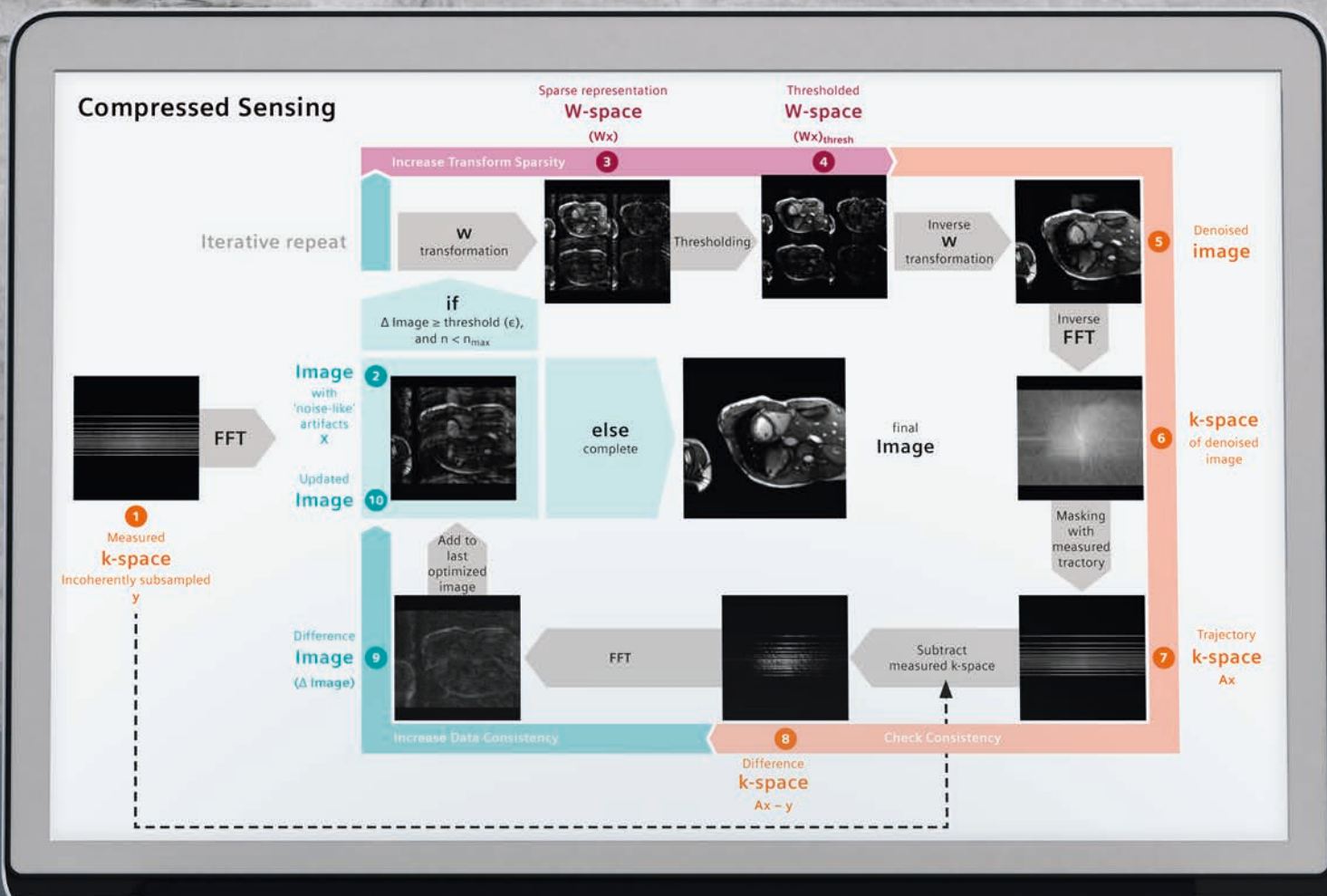


MAGNETOM Flash

The Magazine of MRI

Compressed Sensing Supplement

Not for distribution in the US



Compressed Sensing
Christoph Forman
Page 08

Exercise Cardiac MRI, a Clinical Reality with Compressed Sensing
Wendy Strugnell
Page 16

Compressed Sensing: Application to TOF MRA
Tomohisa Okada
Page 36

Improving Dynamic MRA: Iterative TWIST
Bernd Wintersperger
Page 40

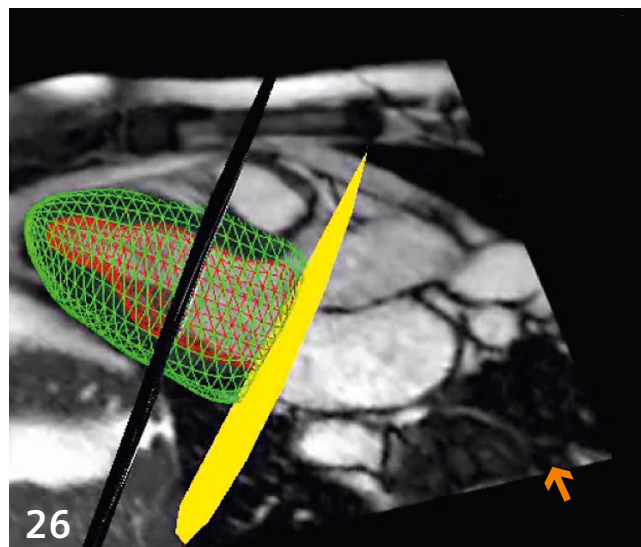
Detection of Insulinomas using Compressed Sensing
Kwadwo Antwi
Page 51

Free-breathing DCE-MRI of the Kidney using GRASP
Philipp Riffel
Page 56

Content



10 Compressed Sensing¹:
a Paradigm Shift in MRI



26 Compressed Sensing¹ for the
Assessment of Left Ventricular Function



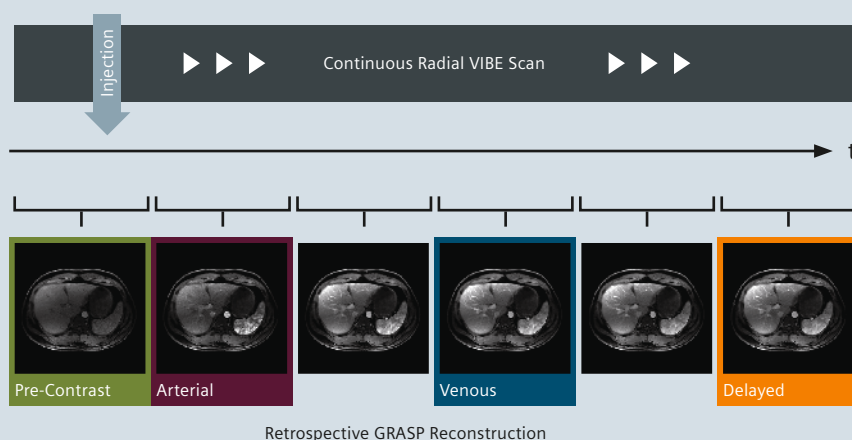
Learn from the experience of other MAGNETOM users

The MAGNETOM World is the community of Siemens MR users worldwide, providing you with relevant clinical information. Here you will find application tips and protocols to optimize your daily work. Lectures and presentations from experts in the field will allow you to be exposed to new ideas and alternative clinical approaches.

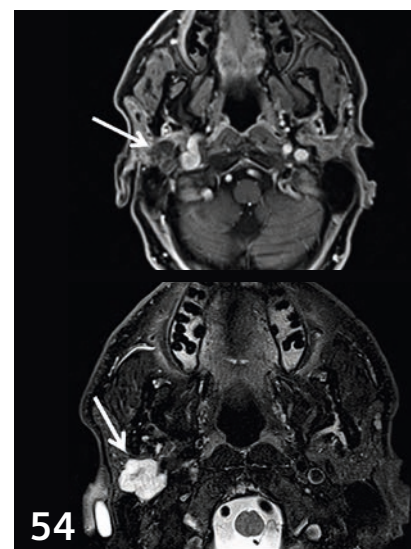
Put the advantages of the
MAGNETOM World to work for you!

www.siemens.com/magnetom-world

- 4 Compressed Sensing¹ –
the Flowchart
*Mathias Blasche, et al.,
Siemens Healthineers,
Erlangen, Germany*
- 8 Compressed Sensing¹:
a Paradigm Shift in MRI
*Christoph Forman, et al.,
Siemens Healthineers,
Erlangen, Germany*
- 14 Compressed Sensing¹ –
a Metaphor
*Mathias Blasche,
Siemens Healthineers,
Erlangen, Germany*
- 16 Exercise Cardiac MRI, a Clinical
Reality with Compressed Sensing¹
*Wendy Strugnell, et al.,
The Prince Charles Hospital,
Brisbane, Australia*
- 21 Accelerated Segmented
Cine TrueFISP of the Heart
on a 1.5T MAGNETOM Aera
Using k-t-sparse SENSE¹
*Maria Carr, et al.,
Northwestern University,
Feinberg School of Medicine,
Chicago, IL, USA*
Reprinted from
MAGNETOM Flash (55) 5/2013
- 26 Preliminary Experiences with
Compressed Sensing Multi-
Slice Cine Acquisitions for the
Assessment of Left Ventricular
Function: CV_sparse WIP¹
*J. Schwitter, et al.,
University Hospital of
Lausanne (CHUV),
Lausanne, Switzerland*
Reprinted from
MAGNETOM Flash (55) 5/2013



44

Compressed Sensing GRASP²MRI of Parotid Tumors with GRASP²

- 36** Compressed Sensing: Application to Time-of-Flight MR Angiography²
Tomohisa Okada, et al., Kyoto University, Japan
- 40** Improving Dynamic MR Angiography: Iterative TWIST²
Bernd J. Wintersperger, et al., University of Toronto, Toronto, Ontario, Canada
- 44** GRASP²: Tackling the Challenges of Abdominopelvic DCE-MRI
Kai Tobias Block, et al., NYU Langone Medical Center, New York, NY, USA
Reprinted from *MAGNETOM Flash* (60) 5/2014
- 51** Case Report: Detection of Insulinomas with High Spatio-temporal Resolution Using Compressed Sensing, Parallel Imaging, and Continuous Golden-Angle Radial Sampling²
Kwadwo Antwi, et al., University Hospital Basel, Basel, Switzerland
- 54** Permeability Imaging of Parotid Tumors with Golden-Angle Radial Sparse Parallel MR Imaging (GRASP)²
Sohil H. Patel, et al., NYU Langone Medical Center, New York, NY, USA
Reprinted from *MAGNETOM Flash* (65) 2/2016
- 56** Free-breathing DCE-MRI of the Kidney using GRASP²
Philipp Riffel, et al., University Medical Center Mannheim, University of Heidelberg, Mannheim, Germany

¹ 510(k) pending. Compressed Sensing Cardiac Cine is not commercially available. Future availability cannot be guaranteed.

² WIP, the product is currently under development and is not for sale in the US and in other countries. Its future availability cannot be ensured.

The information presented in MAGNETOM Flash is for illustration only and is not intended to be relied upon by the reader for instruction as to the practice of medicine. Any health care practitioner reading this information is reminded that they must use their own learning, training and expertise in dealing with their individual patients. This material does not substitute for that duty and is not intended by Siemens Healthcare to be used for any purpose in that regard. The treating physician bears the sole responsibility for the diagnosis and treatment of patients, including drugs and doses prescribed in connection with such use. The Operating Instructions must always be strictly followed when operating the MR System. The source for the technical data is the corresponding data sheets.

Compressed Sensing – the Flowchart

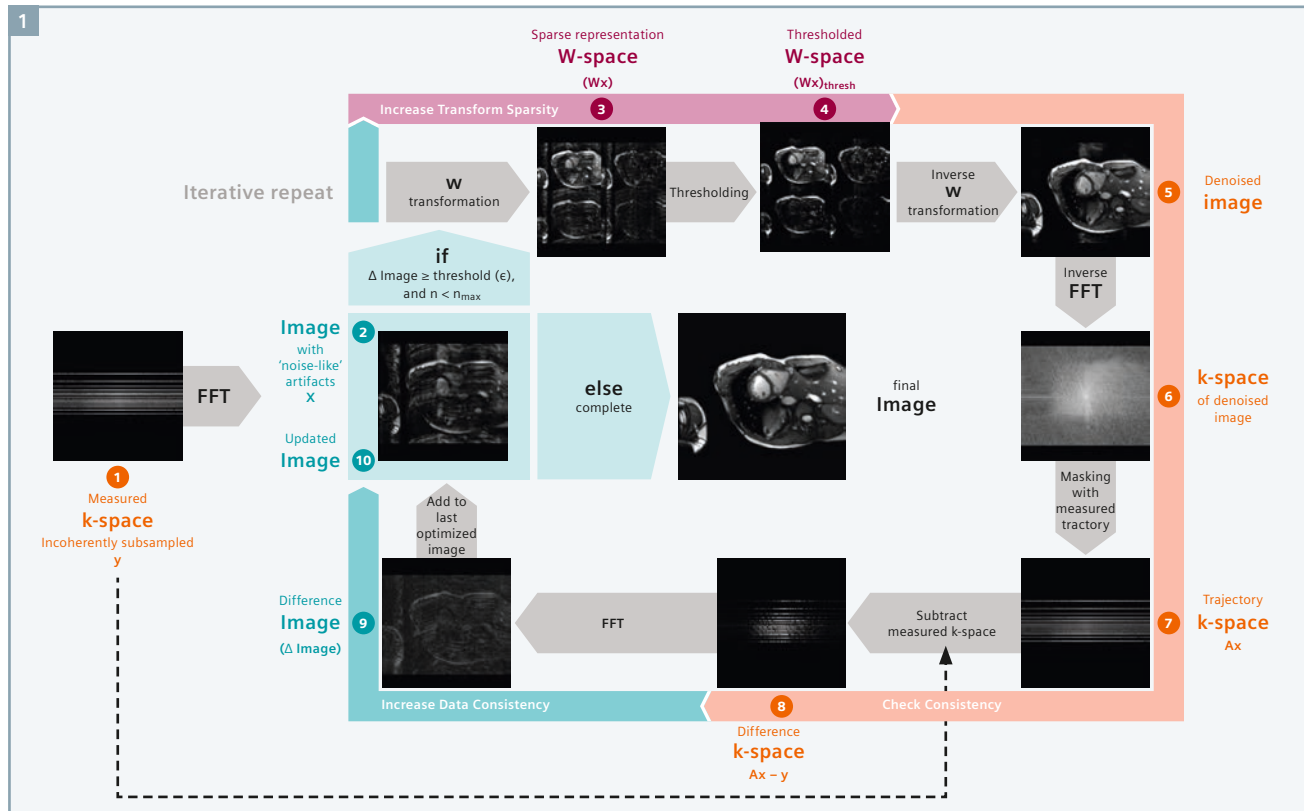
Mathias Blasche; Christoph Forman

Siemens Healthineers, Erlangen, Germany

The three key components of Compressed Sensing (CS)¹ are

1. Incoherent ('random') sub-sampling
2. Transform sparsity
3. Non-linear iterative reconstruction

The Compressed Sensing Flowchart provides a step-by-step visualization of the Compressed Sensing measurement and reconstruction process, explaining where and why these three key components are involved.



1 Compressed Sensing Flowchart. Some 'typical' images of the iterative reconstruction are depicted for visualization purposes.

Abbreviations and terminology

k-space ' y '	Measured data (echoes), sorted in an $m \times n$ matrix; in the formulas denoted as ' y '	A	The transformation A consists of two steps, an inverse FFT and a 'trajectory masking', i.e. only depicting those pixels in k-space that were measured
Image ' x '	Clinical image; in the formulas denoted as ' x '	λ	Weighting factor for the tradeoff between data consistency and transform sparsity
W-space	Different mathematical depiction of the image Examples: Wavelet, Total Variation	$\ ...\ _1$	L1 norm: Sum of all absolute values (here: pixel intensities in W-space)
FFT	(Fast) Fourier transformation; transforms k-space into image space	$\ ...\ _2$	L2 norm, 'Euclidean norm': Square root of sum of squares
FFT ⁻¹	Inverse FFT, transforms image space into k-space		
W	W transformation, transforms image space into W-space		
W ⁻¹	Inverse W Transformation, transforms W-space into image space		

¹ 510(k) pending. Compressed Sensing Cardiac Cine is not commercially available. Future availability cannot be guaranteed.

The Compressed Sensing optimization formula

The following formula describes the optimization process of CS:

$$\min \|Ax - y\|_2^2 + \lambda \|Wx\|_1$$

This means that we are searching for an image x such that the term above is minimized.

The first term describes the 'data consistency'. It minimizes the least-squares difference (L2 norm, $\| \cdot \|_2^2$) between the estimated image x , and the acquired k-space data y . The smaller this (difference) term becomes, the better the consistency.

The second term describes the 'transform sparsity'. It is the L1 norm of the image transformed into a sparse representation (**W**-space). In this term, the sum of the absolute values of the pixels in the transform domain, denoted by the L1 norm ($\| \cdot \|_1$), is minimized. The smaller this L1 norm, the higher the sparsity. λ is an empirical (application-dependent) weighting factor for balancing data consistency vs. sparsity.

Hence, the optimization procedure minimizing this equation seeks to find a solution that fulfills both criteria, data consistency and transform sparsity. This is done in an iterative process.

1. Measured k-space

The first picture is the measured k-space. There are two differences compared to a 'conventional' scan:

1. Strong sub-sampling, i.e. significantly fewer echoes than in a conventional scan. This results in significantly higher scan speed. But since the Nyquist-Shannon sampling theorem [1] is violated, this will result in strong aliasing artifacts.
2. Incoherent ('random') sampling. This is necessary to create a noise-like appearance of the aliasing artifacts (resulting from the sub-sampling). The reason is that these noise-like artifacts (as opposed to structured arti-

facts) can then in a later step of the algorithm be removed with a thresholding procedure in **W**-space (see step 4). The random character of the sampling is essential for the success of the CS reconstruction – "*Randomness is too important to be left to chance*" [2].

The incoherent sampling in CS is different from the (typically) coherent sub-sampling that is used in Parallel Acquisition Techniques, where the (structured) aliasing is removed by means of the knowledge of the coil sensitivity profiles.

The k-space in the formula is denoted as y .

2. Image

As a first step, the (incoherently) subsampled k-space is Fourier transformed into an image.

This image suffers from strong sub-sampling artifacts; but these aliasing artifacts are 'smeared' over the image, due to the incoherence of the sampling in step 1. The aliasing artifacts appear 'noise like'. The better the incoherence of the scan, the more 'homogeneous' the noise-like aliasing artifacts will appear, and the better the CS reconstruction will work.

This image serves as a starting point for the iterative optimization. Since we only covered a small part of k-space in step 1, we do not have the complete information about the image. This image x generated by a straightforward FFT is only one possible solution that is consistent with the measured data – but this solution suffers from strong artifacts. The following iterative process serves to find a better (artifact-free) solution that is also consistent with the measured data y .

The image in the formula is denoted as x .

3. W-space

The image is now transformed into a sparse representation (**W**-space). This is a different 'basis', i.e. a different mathematical

depiction of the image. The goal of this transformation is to locally separate the 'wanted signal' from the noise (artifacts). **W**-space is a better-suited depiction of the image as the sparsity in **W**-space is higher. This means that the image 'informational content' is concentrated in few pixels in **W**-space, while most pixels have only a very low signal.

There are various different transformations that can be beneficial for this purpose. This depends on the application. A Wavelet transformation is a very common choice for MR imaging.

By the way, a Wavelet transformation is utilized in image compression with the JPEG 2000 format [3].

4. Thresholded W-space

After the **W** transformation (e.g. Wavelet transformation), the 'wanted signal' is now to a high degree separated from the noise (artifacts). This allows removing the noise by a thresholding procedure:

- Set all pixels with a value $<$ threshold to zero;
- Subtract the threshold from all other pixel values.

This procedure is called 'soft thresholding'. It has been shown that 'soft thresholding' is beneficial for the solution [4]. The threshold is predefined, optimized for the application.

Since many pixels in **W**-space now have a value of 0, we have fewer non-zero pixels (coefficients). The 'transform sparsity', i.e. the sparsity of the image in **W**-space, is increased.

5. Denoised image

We now transform the **W**-space representation back into image space with the inverse **W** transformation (W^{-1}).

By the thresholding procedure in **W**-space in the last step, we have now an image with less noise. This corresponds to a suppression of the noise-like aliasing artifacts, due to the incoherent sampling we applied in step 1.

However, with this denoising we have also 'fiddled' with the image content. The image has less noise (less artifact power) now, but does not exactly reflect the measurement anymore.

In the next steps 6-8, we will therefore check the image consistency (i.e. how well the denoised image still represents the measurement data).

6. k-space of denoised image

In order to compare the denoised image from step 5 with the measured k-space from step 1, we first apply an inverse Fourier Transformation (FFT^{-1}) to transform the image back to k-space.

Since the image in step 6 was modified, its k-space now consists of all spatial frequencies. This means that we have a 'complete k-space' (all pixels in k-space have non-zero values), as opposed to the measured (subsampled) k-space in step 1 which had only few non-zero values.

7. Trajectory k-space

Now follows a masking process. Remember that we measured only a small part of k-space in step 1. The k-space from step 6, on the other hand, is 'complete'. To compare the two, we filter the k-space (step 6) by only depicting the points (the 'measurement trajectory') of k-space (step 6) that were also measured in k-space (step 1). The rest of k-space (step 6) is set to zero.

The two steps inverse FFT (step 6) and masking (step 7) together are called the '**A** matrix' in the formula. The resulting k-space **Ax** can then be directly compared to the measured k-space **y**.

8. Difference k-space

We now create the 'Difference k-space' by subtracting the k-space **Ax** from step 7 from the measured k-space **y** from step 1.

The difference (**Ax - y**) corresponds to the error (non-consistency) that the thresholding from step 4 has created compared to the measured

k-space **y**. The difference is a 'correction' k-space, so to speak.

9. Difference image

A simple Fourier transformation converts the 'Difference k-space' into a 'Difference image'.

This is used as a correction for the update of the image that we want to optimize.

10. Updated image

The image **x** from step 2 is now updated by adding the correction (difference) image from step 9.

This updated image now has less noise-like artifacts (corresponding to a higher sparsity in W-space) than the image had before the update, due to steps 3 and 4.

At the same time, it was made consistent with the measured k-space from step 1 by means of the correction from steps 8 to 9.

3-10. Iterative reconstruction

Steps 3 to 10 are now repeated. Each iteration will increase the sparsity (in W-space), corresponding to diminishing the aliasing artifacts in image space. At the same time, the consistency of the reconstruction with the measured k-space is taken care of.

This is an alternating optimization of data consistency and transform sparsity, i.e. the two terms in the formula. The factor λ in the formula is a weighting that defines the trade-off between data consistency and sparsity, it is pre-defined and optimized for the application.

As a metaphor:

One can think of scales rocking to and fro (between the optimization of the first term and the optimization of the second term in the formula).

At the same time, the 'center of gravity' (the sum of both terms) is moving down (minimizing both terms in the formula simultaneously). The factor λ in the formula can be thought of as a 'lever', i.e. a shorter (small λ) or longer (large λ) bar of the scales for

the sparsity term as compared to the data consistency term.

The iteration of steps 3 to 10 is repeated until:

- either the least-squares difference of the data consistency term, i.e., the Difference Image (step 9), is smaller than a predefined threshold ϵ ,

$$\|Ax - y\|_2^2 < \epsilon$$

- or a predefined number of iterations N_{\max} is reached.

In the end, we will have an image that is consistent with the measured data, but is denoised (i.e. the noise-like aliasing artifacts have been removed) due to the maximization of the transform sparsity. The final image will (very closely) look as if we had measured k-space completely – but at a much shorter scan time.

Optimization of Compressed Sensing

We have seen that there are many degrees of freedom for the optimization of the Compressed Sensing results. All these need to be taken care of in the application development.

The possible CS acceleration factor depends on the transform sparsity of the dataset. If the acceleration factor is chosen too high ("not justified by the sparsity"), the reconstruction will not yield acceptable results. The possible acceleration factor depends on the application.

The weighting factor λ for the balance between transform sparsity vs. data consistency (as described before) and the threshold for the sparsification in W-space (the soft thresholding in the W-space as discussed earlier) are related to each other in order to achieve optimal results. Also these depend on the application.

All the explanations above are a simplification. There are more 'intricacies' that were not discussed for the sake of simplicity, e.g. how the signals from multiple RF channels are handled, the combination of CS with PAT, higher dimensionality, etc.

The CS Flowchart only shows a depiction of a 2D scan (for the sake of simplicity), but Compressed Sensing can also (and better) be applied for multi-dimensional scans with other k-space trajectories. There are two important aspects for the improvement of the CS performance that define which applications benefit most from CS. These are the “Increase of Sparsity” and the “Increase of Randomness”.

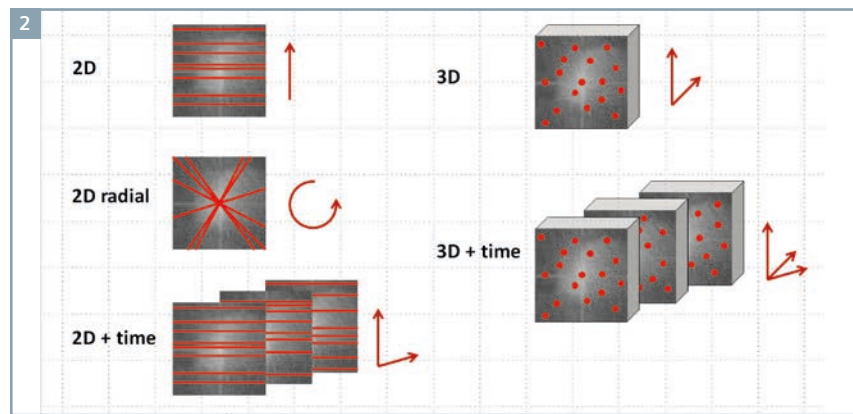
Increase of Sparsity

An “Increase of Sparsity” will enable higher acceleration factors. If the (transform) sparsity of an MR dataset is low, no significant acceleration will be possible, i.e. it will not be possible to remove the noise-like artifacts while preserving an accurate anatomical depiction. For increasing the possible acceleration factor of the scan, a high ‘dimensionality’ of the MR scan helps.

A static 2D scan (like a conventional T2-weighted TSE scan) will typically not have a high sparsity (also not in its Wavelet representation). The achievable acceleration with CS for standard static 2D imaging will therefore not be very high.

But it is very different with e.g. Compressed Sensing Cardiac Cine (2D + time). Along the time dimension, the sparsity is quite high. In CS Cardiac Cine, only little changes are expected between sub-sequent time-frames due to the high temporal resolution and the static anatomy surrounding the heart. This increases the transform sparsity along the time dimension, and therefore high accelerations factors (such as 10) can be achieved in CS Cardiac Cine.

Other examples where the dataset has a high dimensionality and therefore higher sparsity with the potential for



2 Dimensionality, k-space trajectory and degrees of freedom to improve incoherency ('randomness') of the scan.

higher acceleration factors include, for example, 3D scans, dynamic '4D' scans (3D + time) and also diffusion imaging with multiple b-values and or multiple diffusion directions.

Increase of Randomness

Also improving the 'randomness' of the scan will help the performance and the possible acceleration factors of CS.

Figure 2 shows the number of degrees of freedom for different dimensionalities and different k-space trajectories, in order to improve the 'randomness' of the scan.

With static 2D imaging, there is only one degree of freedom, the spacing of the k-space line in phase-encoding direction. The potential for CS acceleration is therefore limited.

With 2D radial imaging, the angle between the different k-space lines can be freely chosen. Each line crosses the center of k-space. There are a couple of advantages for radial imaging vs. cartesian imaging; how-

ever, there are also a couple of disadvantages, such as potential aliasing in both directions and longer reconstruction times. The pros and cons of cartesian vs. radial sampling need to be weighed against each other to find the optimal solution, depending on the application.

2D + time (as in Compressed Sensing Cardiac Cine) also has high dimensionality. There are two degrees of freedom, along the phase-encoding direction and along time. The spatial phase-encoding steps can be chosen differently for each cardiac phase.

Static 3D has two degrees of freedom, since there are two phase-encoding directions. This allows a better 'randomness' than static 2D.

Dynamic 3D has an additional degree of freedom, along time. This high dimensionality of course holds great promise for future developments, already available as WIP packages from Siemens.

Overall, there is a wide potential for future Compressed Sensing applications with high acceleration factors and high clinical relevance.

References

- 1 https://en.wikipedia.org/wiki/Nyquist%E2%80%93Shannon_sampling_theorem
- 2 Marseille GJ, de Beer R, Fuderer M, Mehlkopf AF, van Ormondt D. Nonuniform phase-encode distributions for MRI scan time reduction. J Magn Reson 1996;111:70–75
- 3 https://en.wikipedia.org/wiki/JPEG_2000
- 4 David L. Donoho, De-noising by Soft-Thresholding, <http://statweb.stanford.edu/~donoho/Reports/1992/denoiserelease3.pdf>



Contact

Mathias Blasche
Siemens Healthcare GmbH
Karl-Schall-Str. 6
91050 Erlangen
Germany
Mathias.Blasche@siemens.com

Compressed Sensing: a Paradigm Shift in MRI

Christoph Forman¹; Jens Wetzl²; Carmel Hayes¹; Michaela Schmidt¹

¹ Siemens Healthineers, Magnetic Resonance, Erlangen, Germany

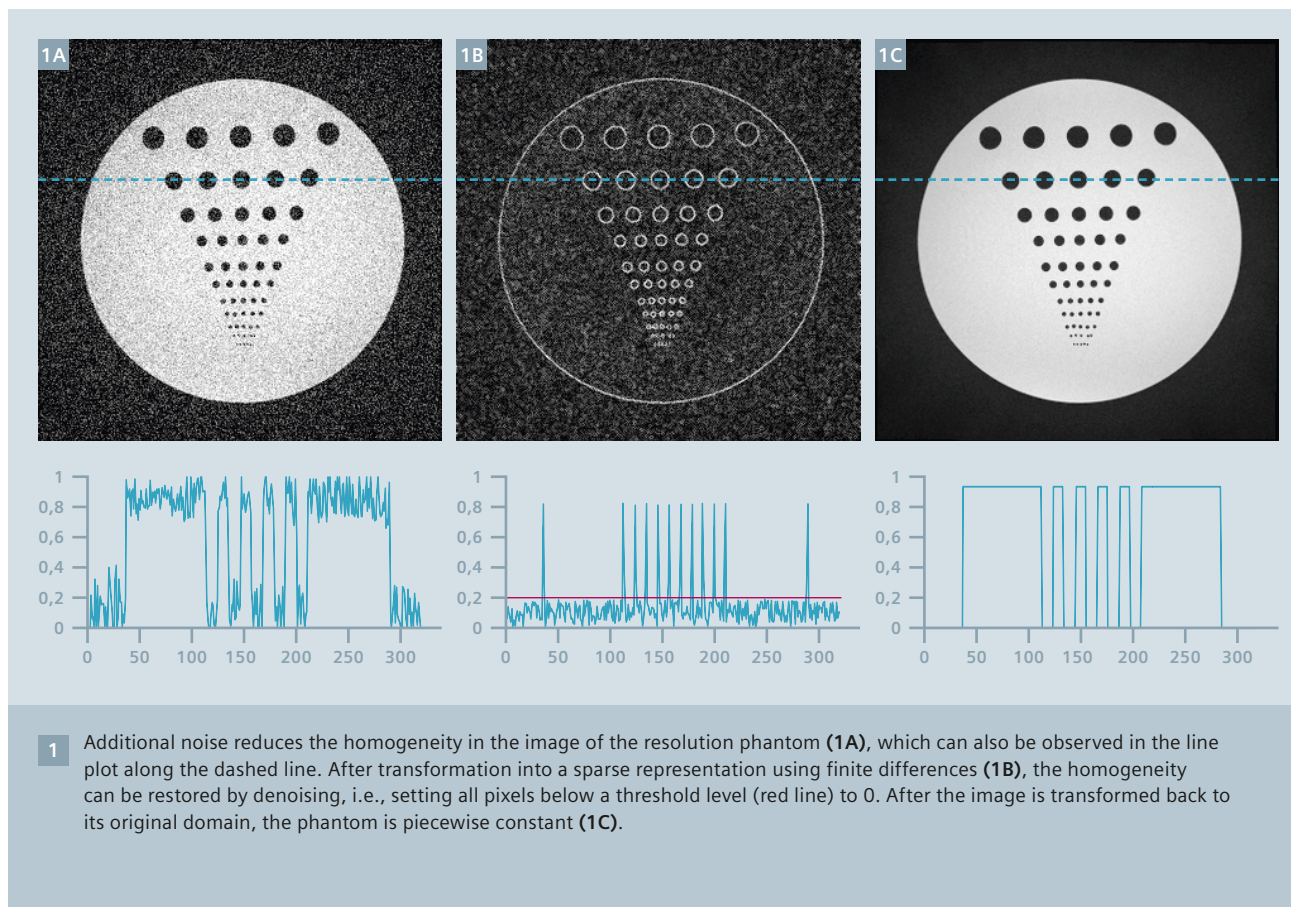
² Pattern Recognition Lab, Friedrich-Alexander-University Erlangen-Nuremberg, Erlangen, Germany

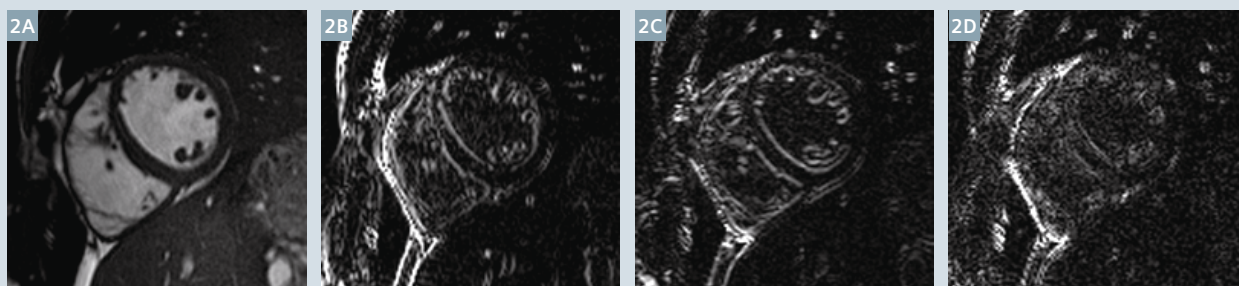
Introduction

Reducing the complexity and length of examinations has been a major direction of research in magnetic resonance imaging (MRI) in recent years. With the introduction of the Dot engines, the complexity of MR examinations could be reduced through automatization and guidance, providing standardized and time-efficient workflows. Consider-

able effort has also been spent on developing methods to speed up data acquisition without degrading image quality. Accelerated imaging is a key factor to enable the visualization of rapid physiological or contrast changes in dynamic imaging. Moreover, short scans reduce the risk of artifacts due to any kind of motion during the scan. A significant

speed-up of data acquisition allows both respiratory and cardiac motion to be frozen while maintaining an adequate temporal and spatial resolution. This in turn results in a high-quality and robust examination even for uncooperative patients, since data acquisition may be performed in free-breathing. Furthermore, reduced scan time and a decreased number of





2 The short-axis view of the heart (2A) is transformed by the wavelet transform to achieve a sparse representation. In addition to the low-resolution representation of the original image, the wavelet transform results in three edge images (2B-2D): While (2B) and (2C) contain the edges in horizontal and vertical direction, respectively, Figure 2D shows the diagonal edge components of the image. In the wavelet domain, the content of the image is sufficiently described by only few coefficients, i.e. the bright pixels.

breath-holds improve patient comfort. Last but not least, accelerated imaging means shorter examinations that can be invested in additional scans, higher resolution, or to improve the overall patient throughput. In this context, parallel imaging and compressed sensing techniques have been proposed to significantly speed up the acquisition time while maintaining diagnostic image quality.

Parallel imaging

Parallel imaging [1, 2] is well established in current clinical practice to speed up data acquisition in a large number of applications. With this technique, scan acceleration is usually achieved by uniformly sub-sampling k -space, for example, by skipping every other line. The resulting aliasing can be unfolded by incorporating the spatial encoding capabilities of multi-coil receiver arrays. However, the scan time reduction is often restricted to moderate acceleration factors between 2 and 4. This limitation is due to the restricted encoding capabilities in terms of number and position of the receiver coils. Additionally, acquiring less data also leads to a reduced signal-to-noise ratio (SNR).

Compressed sensing

In recent years, compressed sensing has gained large scientific attention. Originally, it was proposed as a general concept to accurately reconstruct a signal from a small number of random

measurements [3, 4]. A few years later, compressed sensing¹ was introduced to MRI [5] and successfully combined with parallel imaging [6]. Exploiting the *compressibility* of medical images, this method promises to markedly exceed the acceleration rates that are feasible with parallel imaging. Although compressed sensing has denoising properties, it also has to deal with SNR loss from scan acceleration. Hence, possible acceleration factors scale with the native SNR of the scan. Up to now, the potential of compressed sensing has been shown in a large number of applications from 2D to 5D imaging [7-15].

The successful utilization of compressed sensing is a team play of data acquisition and image reconstruction. In the paper introducing compressed sensing to MRI, three criteria were identified as being essential to ensure successful image recovery from sub-sampled data [5]:

- First, the object that is acquired should have a *sparse representation* after conversion with a mathematical transformation.
- Second, k -space should be sub-sampled such that the aliasing results in *incoherent*, i.e. noise-like, artifacts in the image.
- Finally, image reconstruction requires a *nonlinear, iterative*

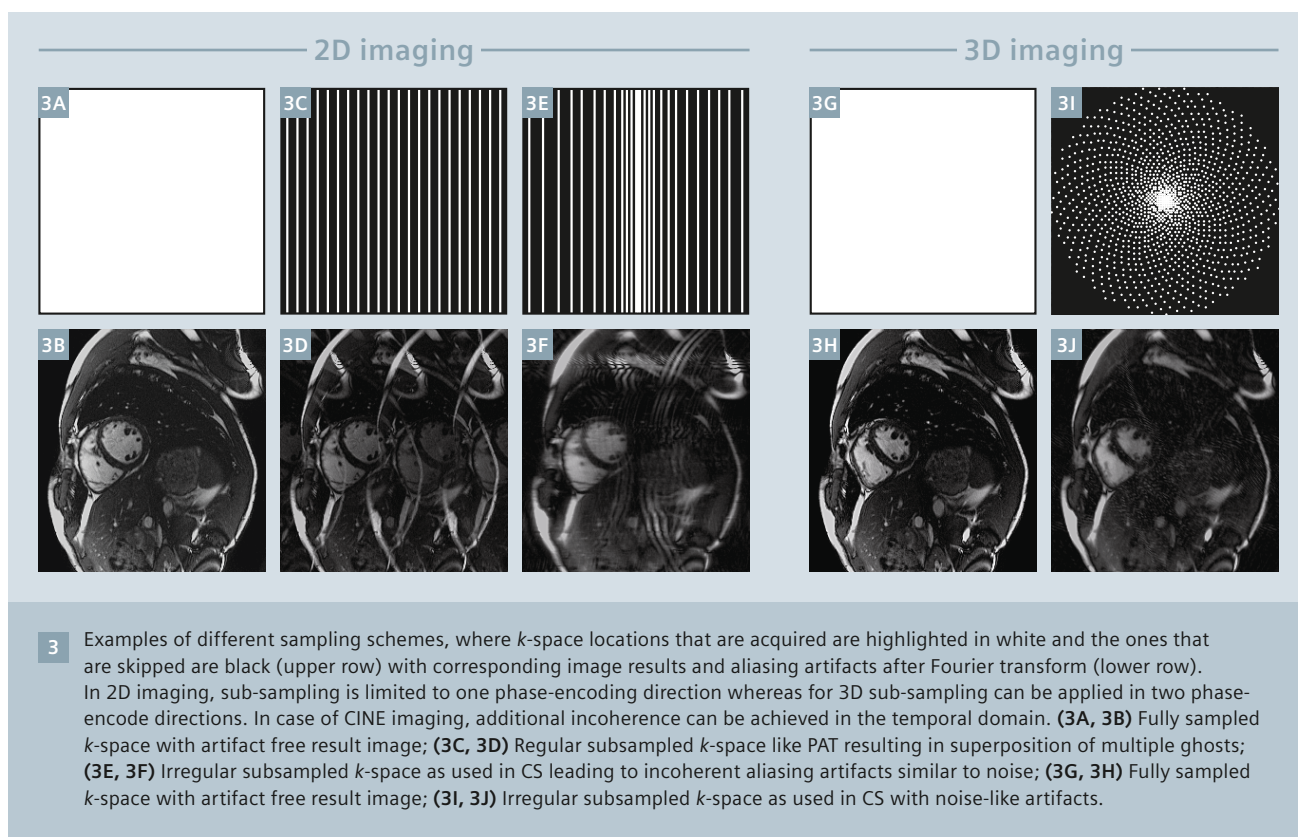
optimization that simultaneously enforces a sparse representation of the resulting image. Thereby, it removes the noise-like artifacts, while it preserves its consistency to the acquired data.

These three essential requirements are discussed in detail below.

Transform sparsity

An image is considered as sparse when its informational content is represented by only a few pixels, while the contribution of the remaining majority of pixels is close to zero. In medical imaging, an angiogram provides a good example for such a sparse representation. However, in MRI, not all images are inherently sparse. But these images can also have a sparse representation utilizing a sparsifying transform. This transform provides an invertible mapping from an image to a sparse representation. Finite differences, i.e. images that contain only edge information, provide a simple technique to achieve a sparse representation, if the image is piecewise constant as shown in Figure 1. Discrete cosine transform and discrete wavelet transform are frequently used in the context of image compression, for example, in JPEG image compression. Utilizing such methods, images may be transformed into a sparse representation (see Fig. 2). In this domain, the content of the image is sufficiently described by only few coefficients,

¹ 510(k) pending. Compressed Sensing Cardiac Cine is not commercially available. Future availability cannot be guaranteed.



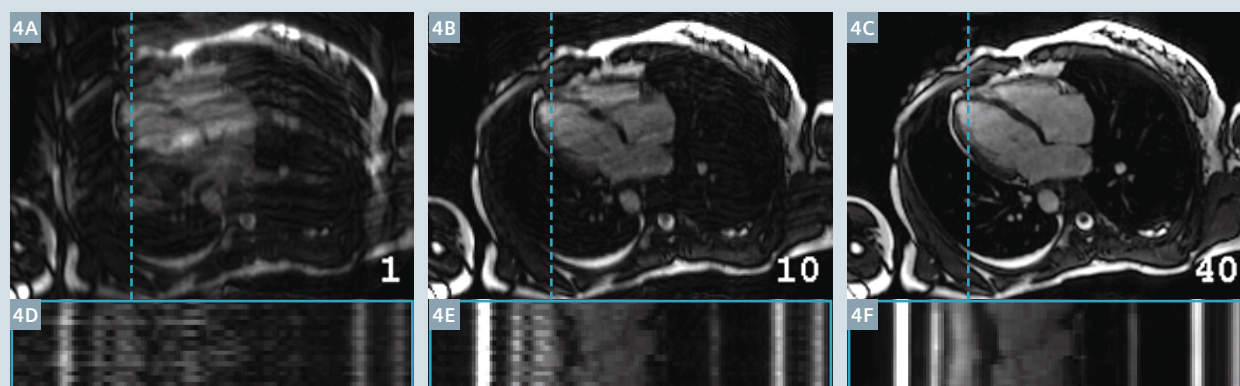
i.e. the bright pixels. The percentage of these pixels relative to the total number of pixels defines the sparsity of the image. For image compression, pixels in this sparse representation that are below a certain threshold can be set to zero, which facilitates a compression of the signal. Once the compressed signal is converted back to its initial domain, the visual difference between the resulting image and its original version is negligible. In particular, the discrete wavelet transform has been shown to be a suitable sparsifying transform for many natural images, including MRI images, and is commonly used in compressed sensing applications. In the case of dynamic imaging, including CINE imaging, this transform can also be applied in the temporal dimension. The redundancy of information along this temporal dimension can be exploited, and often the sparsity is even higher compared to the spatial dimensions.

Incoherent sampling

Unlike the regular sub-sampling patterns used for parallel imaging,

the data acquisition process for compressed sensing requires that k -space sub-sampling is irregular (see Fig. 3C for regular and 3E, 3I for irregular sampling). In conventional Cartesian parallel imaging, regular sub-sampling of k -space is advantageous in that the phase-encoding gradient is increasing linearly during the measurement, which is beneficial for physical and MRI hardware limitation reasons. However, violating the Nyquist sampling theorem in this manner results in a superposition of shifted replicas of the original signal as illustrated in Figure 3D. The number of replicas equals the chosen sub-sampling rate. This aliasing can then be unfolded utilizing the spatial encoding capabilities of the multi-coil receiver array and parallel imaging. In contrast, irregular, incoherent sub-sampling of k -space, as required for compressed sensing, would result in a noise-like appearance of sub-sampling artifacts (see Figs. 3F, 3J). Theoretically, completely random sub-sampling is optimal to ensure this noise-like behavior. However, purely random sampling is impractical in the case of MRI.

On the one hand, large and random steps in k -space may require large-amplitude gradient steps and should be avoided due to hardware limitations and physical reasons. On the other hand, the sampling trajectory must be repeatable to allow the same acquisition to be reproduced with consistent image quality. Therefore, sub-sampling patterns featuring deterministic properties that mimic random sampling within the given constraints are frequently used for compressed sensing data acquisition. In 2D Cartesian imaging with pure spatial coverage, the sub-sampling is limited to one dimension, as only the phase-encoding direction is sub-sampled in MRI. But in case of 2D dynamic imaging, the sampling pattern can be varied from one time frame to the next in order to maintain sufficient incoherence for compressed sensing. In 3D Cartesian imaging, sub-sampling can be applied in two phase-encoding directions. Alternatively, non-Cartesian sampling trajectories can be used, e.g., radial or spiral imaging, that already facilitate an incoherent sampling of k -space for 2D imaging.



4 This Figure shows the progress of the optimization procedure to preserve data fidelity and reduce noise-like artifacts exemplarily in a Cardiac 2D CINE dataset (4A-4C). While the top image shows one image of the time series, a temporal profile along the dashed line is plotted below. The incoherent sub-sampling in the spatio-temporal domain results in incoherent artifacts that dominate the image after the first iteration (4A). Enforcing a sparse representation of the image and exploiting temporal redundancy, these artifacts are reduced with an increasing number of iterations (4B). The compressed sensing reconstruction is terminated after 40 iterations and results in an aliasing-free image (4C).

Nonlinear image reconstruction

If the two above-mentioned requirements are sufficiently met, the image can be recovered from the sub-sampled data by nonlinear, iterative reconstruction. In this reconstruction, a *data fidelity* term ensures consistency of the estimated image to the acquired data and a *transform sparsity* term enforces a sparse representation of the image in the transform domain by solving the following equation:

$$\min_x \underbrace{\|Ax - y\|_2^2}_{\text{data fidelity}} + \lambda \underbrace{\|\Phi(x)\|_1}_{\text{transform sparsity}}$$

The data fidelity term minimizes the least-squares difference ($\| \cdot \|_2^2$) between the estimated image, x , and the acquired k -space data, y . The system matrix, A , describes the data acquisition process, i.e., the transform from spatio-temporal to frequency domain, which is required for the comparison of the image and acquired data. Incorporating parallel imaging, it consists of the coil sensitivity maps of the individual receiver coil elements, the Fourier transform, and the applied

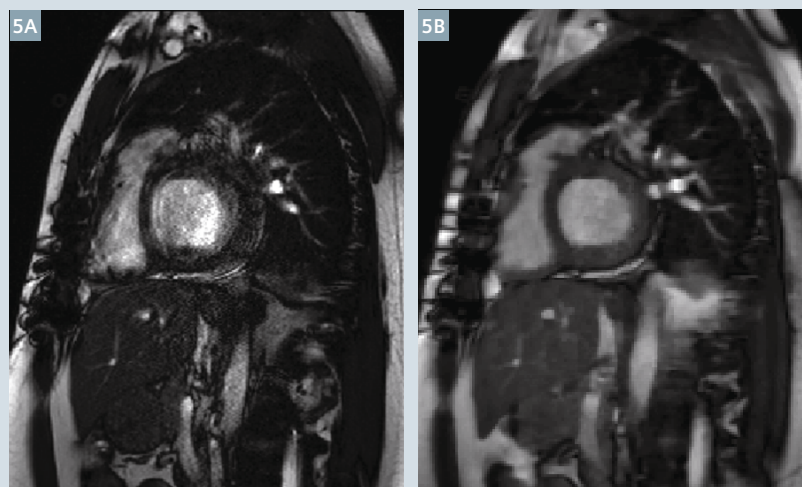
sub-sampling pattern during data acquisition. In the transform sparsity term, the image is transformed into a sparse representation by $\Phi(\cdot)$, for example, using the discrete wavelet transform. In this term, the sum of the absolute values of the pixels in the transform domain, denoted by the ℓ_1 norm ($\| \cdot \|_1$), is minimized. Hence, the optimization procedure minimizing this equation seeks to find a solution that fulfills both criteria, data consistency and transform sparsity. This optimization procedure is more computationally intensive than conventional reconstruction, e.g., parallel imaging. The balance between data fidelity and sparsity is adjusted with the regularization parameter λ , which is usually found empirically. While small values of λ lead to an image that is closer to the acquired data, increasing this value tends to produce an image that is in favor of the sparse solution. When λ is too low, the image will be noisy, and when λ is too high a strongly filtered image appearance may be the consequence. The equation described above is iteratively minimized until a convergence criterion is met or a fixed number of iterations is reached. Figure 4 illustrates this optimization in the example of real-time CINE imaging of the heart.

Transition into clinical routine

Compressed sensing acquisition and reconstruction have been completely integrated into our clinical MRI scanners. Works-in-progress packages have been developed and tested by our clinical cooperation partners world-wide for various applications in the fields of cardiovascular [16-19], neurological [20], musculoskeletal [21-23] and oncological [24] imaging. The additional parameters needed to compose the compressed sensing protocols, for both acquisition and reconstruction, have been seamlessly integrated into our user interface (UI). A selection of possible continuous acceleration factors takes the place of discrete numbers that were familiar from parallel imaging. This facilitates a UI experience with a low level of complexity. The award-winning algorithm for compressed sensing reconstruction [8], ranking first at the ISMRM 2014 "sub-Nyquist" reconstruction challenge, has been fully integrated into the Siemens image reconstruction environment. Without the need for additional hardware, the images are directly calculated inline utilizing the full computational power of the reconstruction computer. Compressed

sensing reconstruction is performed on a graphics processing unit, which provides a significant speed-up in processing time. For example, the image series of one cardiac real-time CINE slice is processed in 10 to 15 seconds.

Thanks to its high acceleration rate due to compressed sensing, real-time sequences allow for a temporal and spatial resolution comparable to that of conventional segmented acquisitions. For example, compressed sensing in cardiac imaging permits fast quantification of left-ventricular (LV) function in a single breath-hold [25]. As demonstrated in Figure 5, this sequence still provides diagnostic images for LV function quantification even in challenging scenarios, such as in the presence of arrhythmia, where conventional sequences usually fail. This sequence may also be applied in free-breathing, which is beneficial for patients who are not able to hold their breath sufficiently and, in general, allows for a simplified and more patient-friendly examination workflow.



5 In cardiac imaging, the high acceleration rate due to compressed sensing enables real-time CINE imaging with a temporal and spatial resolution in a comparable range as conventional segmented acquisitions. While conventional imaging might fail in challenging scenarios, like in case of arrhythmia (5A), the compressed sensing real-time sequence preserves a diagnostic image quality that still enables the quantification of LV function (5B). Images courtesy of Dr. François Pontana, Lille University Hospital, Lille, France.

Conclusion

Compressed sensing facilitates rapid MR imaging by exploiting the fact that medical images have a sparse representation in a certain transfer domain. Representing a team play of data acquisition and image reconstruction, this allows for the reconstruction of artifact-free images following incoherent data acquisition. The acceleration enables a reduction in the acquisition time or an improvement in the spatial and/or temporal resolution. Real-time imaging featuring compressed sensing helps to reduce the need for breath-holding or ECG triggering. The integration of protocols based on compressed sensing in clinical workflows allows a significant reduction in the examination time for each patient. Our generalized integration of compressed sensing in the scanner environment will allow for the straightforward introduction of further applications that are likely to come in the near future.

References

- 1 M. A. Griswold, P. M. Jakob, R. M. Heidemann, M. Nittka, V. Jellus, J. Wang, B. Kiefer, and A. Haase. "Generalized Autocalibrating Partially Parallel Acquisitions (GRAPPA)". *Magnetic Resonance in Medicine*, Vol. 47, No. 6, pp. 1202–1210, June 2002.
- 2 K. Pruessmann, M. Weiger, M. B. Scheidegger, and P. Boesiger. "SENSE: Sensitivity Encoding for Fast MRI". *Magnetic Resonance in Medicine*, Vol. 42, No. 5, pp. 952–962, Nov. 1999.
- 3 D. Donoho. "Compressed Sensing". *IEEE Transactions on Information Theory*, Vol. 52, No. 4, pp. 1289–1306, Apr. 2006.
- 4 E. Candes and J. Romberg. "Sparsity and incoherence in compressive sampling". *Inverse problems*, Vol. 23, No. 3, pp. 969–985, Apr. 2007.
- 5 M. Lustig, D. Donoho, and J. M. Pauly. "Sparse MRI: The Application of Compressed Sensing for Rapid MR Imaging". *Magnetic Resonance in Medicine*, Vol. 58, No. 6, pp. 1182–1195, Dec. 2007.
- 6 D. Liang, B. Liu, J. Wang, and L. Ying. "Accelerating SENSE Using Compressed Sensing". *Magnetic Resonance in Medicine*, Vol. 62, No. 6, pp. 1574–1584, Dec. 2009.
- 7 G. Adluru, L. Chen, S. Kim, N. Burgon, E. G. Kholmovski, N. F. Marrouche, and E. V. R. DiBella. "Three-dimensional late gadolinium enhancement imaging of the left atrium with a hybrid radial acquisition and compressed sensing". *Journal of Magnetic Resonance Imaging*, Vol. 34, No. 6, pp. 1465–1471, Dec. 2011.
- 8 J. Liu, J. Rapin, T.-C. Chang, A. Lefebvre, M. O. Zenge, E. Mueller, and M. S. Nadar. "Dynamic cardiac MRI reconstruction with weighted redundant Haar wavelets". In: *Proceedings of the 20th Annual Meeting of ISMRM*, p. 4249, Melbourne, Australia, May 2012.
- 9 F. Han, S. Rapacchi, S. Kahn, I. Ayad, I. Salusky, S. Gabriel, A. Plotnik, J. P. Finn, and P. Hu. "Four-dimensional, multiphase, steady-state imaging with contrast enhancement (MUSIC) in the heart: A feasibility study in children". *Magnetic Resonance in Medicine*, Vol. 74, No. 4, pp. 1042–1049, Oct. 2015.
- 10 S. T. Ting, R. Ahmad, N. Jin, J. Craft, J. Serafim da Silveira, H. Xue, and O. P. Simonetti. "Fast Implementation for Compressive Recovery of Highly Accelerated Cardiac Cine MRI Using the Balanced Sparse Model". *Magnetic Resonance in Medicine*, doi: 10.1002/mrm.26224.

- 11 D. Stäb, T. Wech, F. A. Breuer, A. M. Weng, C. O. Ritter, D. Hahn, and H. Köstler, "High resolution myocardial first-pass perfusion imaging with extended anatomic coverage". *Journal of Magnetic Resonance Imaging*, Vol. 39, No. 6, pp. 1575–1587, Jun. 2014.
- 12 X. Chen, M. Salerno, Y. Yang, and F. H. Epstein, "Motion-compensated compressed sensing for dynamic contrast-enhanced MRI using regional spatiotemporal sparsity and region tracking: Block low-rank sparsity with motion-guidance (BLOSM)", *Magnetic Resonance in Medicine*, Vol. 72, No. 4, pp. 1028–1038, Oct 2014.
- 13 H. Xue, S. Inati, S. Sørensen, P. Kellman, and M. S. Hansen, "Distributed MRI Reconstruction Using Gadgetron-Based Cloud Computing", *Magnetic Resonance in Medicine*, Vol. 73, No. 3, pp. 1015–1025, March 2015.
- 14 J. Wetzl, F. Lugauer, M. Schmidt, A. Maier, J. Hornegger, and C. Forman. "Free-Breathing, Self-Navigated Isotropic 3-D CINE Imaging of the Whole Heart Using Cartesian Sampling", In: *Proceedings of the 24th Annual Meeting of ISMRM*, p. 411, Singapore, May 2016.
- 15 L. Feng, L. Axel, H. Chandarana, K. T. Block, D. K. Sodickson, and R. Otazo. "XD-GRASP: Golden-angle radial MRI with reconstruction of extra motion-state dimensions using compressed sensing". *Magnetic Resonance in Medicine*, Vol. 75, No. 2, pp. 775–788, Feb. 2016.
- 16 C. Forman, D. Piccini, R. Grimm, J. Hutter, J. Hornegger, and M.O. Zenge. "Reduction of respiratory motion artifacts for free-breathing whole-heart coronary MRA by weighted iterative reconstruction", *Magnetic Resonance in Medicine*, Vol. 73, No. 5, pp. 1885–1895, May 2015.
- 17 A. F. Stalder, M. Schmidt, H. H. Quick, M. Schlamann, S. Maderwald, P. Schmitt, Q. Wang, M. S. Nadar, and M. O. Zenge. "Highly undersampled contrast-enhanced MRA with iterative reconstruction: Integration in a clinical setting", *Magnetic Resonance in Medicine*, Vol. 74, No. 6, pp. 1652–1660, Dec. 2015
- 18 T. Yamamoto, K. Fujimoto, T. Okada, Y. Fushimi, A. Stalder, Y. Natsuaki, M. Schmidt, and K Togashi, "Time-of-Flight Magnetic Resonance Angiography With Sparse Undersampling and Iterative Reconstruction: Comparison With Conventional Parallel Imaging for Accelerated Imaging", *Investigative Radiology*, Vol. 51, No. 6, pp. 372–378, Jun 2016.
- 19 J. Wetzl, C. Forman, B. J. Wintersperger, L. D'Errico, M. Schmidt, B. Mailhe, A. Maier, and A. F. Stalder. "High-resolution dynamic CE-MRA of the thorax enabled by iterative TWIST reconstruction", *Magnetic Resonance in Medicine*, doi: 10.1002/mrm.26146.
- 20 E. Mussard, T. Hilbert, R. Meuli, J.-P. Thiran, and T. Kober. "Accelerated MP2RAGE Imaging Using Sparse Iterative Reconstruction", In: *Proceedings of the 24th Annual Meeting of ISMRM*, p. 4216, Singapore, May 2016.
- 21 R. Otazo, M. Nittka, M. Bruno, E. Raithel, C. Geppert, S. Gyftopoulos, M. Recht, and L. Rybak. "Sparse-SEMAC: Rapid and Improved SEMAC Metal Implant Imaging Using SPARSE-SENSE Acceleration", *Magnetic Resonance Imaging*, July 2016, Early View, DOI: 10.1002/mrm.26342.
- 22 J. Fritz, S. Ahlawat, S. Demehri, G.K. Thawait, E. Raithel, W.D. Gilson, M. Nittka. "Compressed Sensing SEMAC: 8-fold Accelerated High Resolution Metal Artifact Reduction MRI of Cobalt-Chromium Knee Arthroplasty Implants", *Investigative Radiology*, October 2016, Vol. 51, Issue 10, pp 666–676.
- 23 J. Fritz, E. Raithel, G. K. Thawait, W. Gilson, and D. F. Papp. "Six-Fold Acceleration of High-Spatial Resolution 3D SPACE MRI of the Knee Through Incoherent k-Space Under-sampling and Iterative Reconstruction – First Experience". *Investigative Radiology*, Vol. 51, No. 6, pp. 400–409, Jun 2016.
- 24 D. Nickel, X. Chen, B. Mailhe, Q. Wang, Y. Son, J. M. Lee, and B. Kiefer. "Motion-resolved 3D dynamic contrast enhanced liver MRI", In: *Proceedings of the 24th Annual Meeting of ISMRM*, p. 4253, Singapore, May 2016.
- 25 G. Vincenti, P. Monney, J. Chaptinel, T. Rutz, S. Coppo, M.O. Zenge, M. Schmidt, M.S. Nadar, D. Piccini, P. Chèvre, M. Stuber, and J. Schwitter, "Compressed Sensing Single-Breath-Hold CMR for Fast Quantification of LV Function, Volumes, and Mass" *JACC: Cardiovascular Imaging*, Vol. 7, No. 9, pp. 882–892, Sep. 2014.



Contact

Christoph Forman
Siemens Healthcare GmbH
HC DI MR PI TIO CARD
Postbox 32 60
91050 Erlangen
Germany
christoph.forman@siemens.com

For further information,
articles, case studies and keynotes
on the topic of Compressed Sensing
please visit

www.siemens.com/Compressed-Sensing

Compressed Sensing – a Metaphor

Mathias Blasche

Siemens Healthineers, Erlangen, Germany

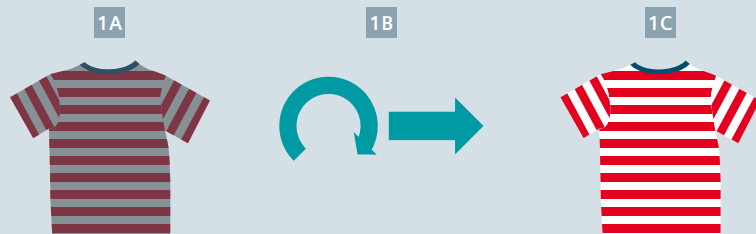
Compressed Sensing (CS)¹ is an exciting new method with the potential to accelerate MR scans beyond what is possible with any other method. However, the CS reconstruction method is more complicated than the straightforward Fourier transform used in conventional MR imaging.

¹ 510(k) pending. Compressed Sensing Cardiac Cine is not commercially available. Future availability cannot be guaranteed.

The three key components of CS – incoherent sub-sampling, transform sparsity, and iterative reconstruction – may sound ‘unwieldy’ to many readers.

The ‘Washing Metaphor’ described below compares the CS mechanism with the washing of a T-shirt. This might look a little funny (and in fact this is intended), but it is actually quite an accurate analogy. It might help understanding CS in a ‘non-technical’ sort of way. Enjoy!

The goal of Compressed Sensing is to remove the (noise-like) aliasing artifacts from the image (that are due to the incoherent sub-sampling of the measured k -space) while ensuring that the reconstructed image is still consistent with the measured data.



1 Goal of Compressed Sensing

(1A) MRI: We measure only a part of k -space (sub-sampling) in an incoherent (‘random’) way. This results in an image with noise-like aliasing artifacts.

Metaphor: We have a dirty T-shirt¹. The dirt is homogeneously grey.

(1B) MRI: By maximizing transform sparsity², we remove the noise (= the aliasing artifacts) from the image. We take care that we keep the reconstructed image consistent with the measured data. The simultaneous improvement of sparsity and data consistency is done in an alternating fashion, iteratively until the optimum is achieved.

Metaphor: We wash the T-shirt in the rotating tub of the washing machine to remove the grey dirt. We take care not to wash out the colors.

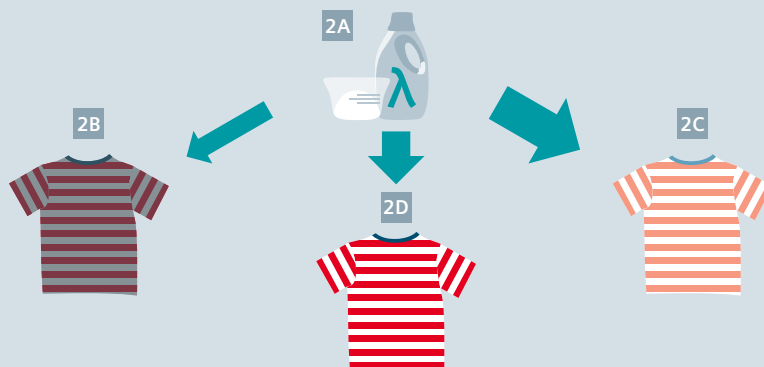
(1C) MRI: The result is an anatomically correct image without aliasing artifacts (noise). The image looks virtually identical to an image with a completely measured k -space – but at much shorter scan time.

Metaphor: The T-shirt is clean, and the colors have been preserved. The T-shirt looks like new.

¹ Note: The red-white striped T-shirt was chosen as an arbitrary example. The stripes have nothing to do with any ‘regular’ sampling of k -space.

² ‘Sparsity’ stands for ‘transform sparsity’ in the remainder of the text, i.e. the sparsity in W -space, e.g. the Wavelet domain. Increasing sparsity in W -space corresponds to decreasing noise in image space.

In order to achieve the optimal result, the sum of sparsity and data consistency is maximized. This corresponds to a minimization of noise (= aliasing artifacts) while keeping anatomical accuracy. The sparsity needs to be optimally balanced with respect to the data consistency.



2 Sparsity vs. Data Consistency

(2A) MRI: For optimal balancing between sparsity and data consistency, the correct weighting factor λ needs to be applied. λ is application dependent and is optimized during the application development.³

Metaphor: The right amount of detergent has to be used.

(2B) MRI: If the sparsity weighting is too low (λ too small), there is still noise (aliasing artifacts) in the image.

Metaphor: With too little detergent, we will not remove the dirt on the T-shirt.

(2C) MRI: If the sparsity weighting is too high (λ too large), we will lose data consistency. The image is noise free but it does not show the true anatomy.

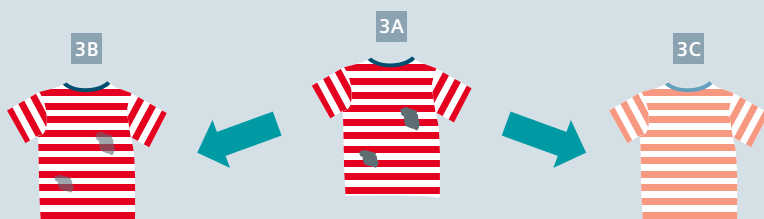
Metaphor: Using too much detergent, the dirt will be gone – but also the colors.

(2D) MRI: The right balance between sparsity and data consistency (optimal λ) results in the anatomy being depicted correctly, without noise (aliasing artifacts). The image looks as if we had measured k -space completely – but at much shorter scan time.

Metaphor: With the right amount of detergent, the dirt can be removed without affecting the colors. The T-shirt looks like new.

³ To avoid misunderstandings: λ is preset, it is optimized for the application. It is not changed in the iterative reconstruction. Rather, the iterative reconstruction improves data consistency and sparsity in an alternating fashion, based on the preset λ .

Finally, we want to emphasize again the importance of incoherent ('random') scanning for a successful CS reconstruction.



3 The Importance of Incoherent Scanning

(3A) MRI: In case we do not sample k -space 'randomly enough', the aliasing artifacts will appear in a discrete way and not noise-like. Without this critical prerequisite for CS, the reconstruction will fail⁴.

Metaphor: If we have concentrated stains instead of 'homogeneous dirt', it will not be possible to wash the stains off without destroying the colors.

(3B) MRI: If we concentrate on data consistency, we will not get rid of the artifacts (which are not noise-like but discrete).

Metaphor: If we concentrate on not washing off the colors (by using a low amount of detergent), we will not succeed in removing the concentrated stains completely.

(3C) MRI: If we emphasize sparsity (complete removal of the discrete high-intensity aliasing artifacts which are not noise-like), this will go at the expense of data consistency. The anatomy is not depicted correctly.

Metaphor: If we use enough detergent to wash off the stains, the colors will also fade out.

⁴ For the sake of simplicity, we are discussing a pure CS reconstruction without the combination with parallel imaging. The combination with parallel imaging would also address discrete aliasing artifacts to a certain degree.

Exercise Cardiac MRI, a Clinical Reality with Compressed Sensing

Wendy Strugnell, BAppSc(MIT) FSMRT; Aaron Lin, MBChB, FRACP

Richard Slaughter Centre of Excellence in Cardiovascular MRI, The Prince Charles Hospital, Brisbane, Australia

Introduction

Non-invasive assessment of ventricular function plays an important role in the diagnosis and management of cardiac diseases. With its high temporal and spatial resolution, cardiac MRI is considered the most accurate non-invasive tool for providing left ventricular (LV) volumes, ejection fraction (EF) and mass at rest [1-3]. Cardiac MRI is also superior to other imaging modalities for quantitative assessment of the complexly shaped right ventricle (RV) [4-6].

Due to practical and technical limitations of imaging, clinical cardiac assessment is conventionally performed with the patient at rest. However, in many heart diseases, symptoms do not occur at rest and ventricular assessment during exercise is necessary to unmask ventricular dysfunction that is not apparent at rest. Despite recent technological advances across imaging modalities, assessment of dynamic ventricular

response during exercise remains challenging. Until now, non-invasive quantitative cardiac assessment during exercise has been performed using echocardiography and nuclear scintigraphy, both of which have significant limitations, particularly in the assessment of the RV. As MRI is superior to other imaging modalities in accuracy and reproducibility of ventricular functional results at rest, there is a clinical need for a reliable MRI assessment of the heart during exercise.

Limitations of cardiac MRI during exercise

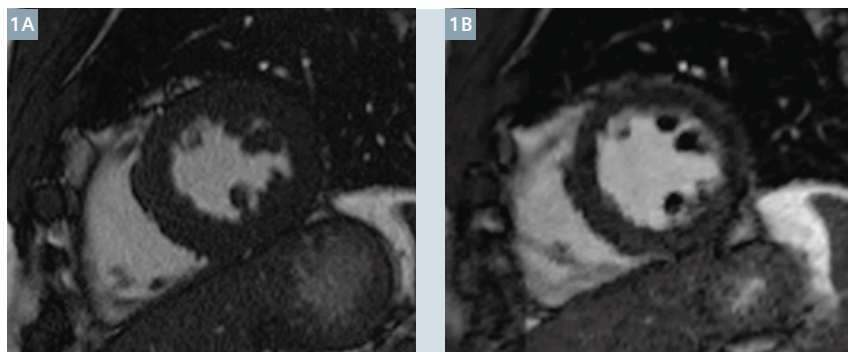
Quantitative MRI assessment of cardiac function requires the acquisition of a stack of ECG-gated, cine ventricular short-axis images [5]. This time-consuming process requires multiple breath-holds to cover the entire ventricle and can be difficult for some patients to complete. This process can be made more

challenging by exercise, particularly in patients with cardiac and pulmonary diseases whose baseline exercise and respiratory capacities are limited.

These limitations have driven the search for faster imaging techniques that maintain acceptable image quality and temporal resolution from resting heart rates through to accelerated heart rates during exercise. Real-time MRI is less susceptible to motion caused either by exercising or breathing and can be performed without ECG gating. La Gerche et al. [7] recently demonstrated that when real-time ungated MRI is combined with *post hoc* analysis incorporating compensation for respiratory motion, accurate biventricular volumes could be measured during maximal exercise. However, the methodology is labor intensive with lengthy post-processing times, and the authors acknowledge that there is significant difficulty in identifying the endocardium at higher levels of exercise. Access to commercially available processing software to enable analysis is another major limitation of this technique. Most real-time sequences also have low temporal resolution, which may affect accuracy at the high heart rates encountered during exercise. Clearly, the pursuit for a fast, clinically feasible MRI technique for evaluating the ventricles during exercise remains.

Compressed Sensing MRI

Compressed Sensing (CS)¹ was recently proposed as a means to considerably



1 Midventricular short-axis images at end-diastole from the conventional bSSFP acquisition (acceleration factor 2) (**1A**) and the high spatial and temporal resolution CS_bSSFP acquisition (acceleration factor 8) (**1B**), from the same patient.

¹ 510(k) pending. Compressed Sensing is not commercially available. Future availability cannot be guaranteed.

accelerate data acquisition through sparse sampling and reconstructing signals or images from significantly fewer measurements than were traditionally thought necessary [8, 9]. Using incoherent sparse sampling, nonlinear reconstruction algorithms and iterative processing, these methods reconstruct undersampled data from significantly fewer measurements whilst maintaining in-plane spatial resolution [10]. Cardiac MRI is ideally suited to CS techniques. Vincenti et al. [11] demonstrated that the application of CS to cardiac imaging enabled several-fold acceleration and achieved a cine acquisition of the whole heart in one breath-hold.

With local institutional review board approval, we recently tested a prototype, ECG-triggered balanced steady-state free precession cine sequence with compressed sensing (CS_bSSFP)¹ (net acceleration of 8) against the conventional bSSFP sequence (net acceleration of 2) on clinical patients using comparable parameters for spatial and temporal resolution. We concluded that accurate and reproducible volumetric quantifications equaling those of conventional bSSFP could be achieved in the assessment of the left ventricle at rest in various cardiac disease states at significantly shorter acquisition times [12] (Fig. 1).

	bSSFP	CS_bSSFP ¹
TR (ms)	3	2.53
TE (ms)	1.25	1
Field-of-view (mm)	380 x 290	380 x 312
Image Matrix	304 x 232	192 x 192
Spatial resolution (mm)	1.25 x 1.25	1.98 x 1.98
Temporal resolution (ms)	~30	~20
Slice thickness/gap (mm)	8 mm / 2 mm	8 mm / 2 mm
Flip angle (°)	70	70
Bandwidth (Hz/pixel)	914	898
Heartbeats per slice	14-20	1 or 2*
Cardiac phases	30	18-25*
ECG triggering	Retrospective	Prospective
Breath-holds	10	1 or 2*
Breath-hold duration (s)	10	5-7*

*Heart rate dependent

Table 1: Imaging parameters of conventional bSSFP and CS_bSSFP¹ sequences.

Exercise cardiac MRI

Patients with cardiac and pulmonary diseases typically have limited exercise tolerance and breath-hold capacity. Quantitation of ventricular function by cardiac MRI during exercise requires:

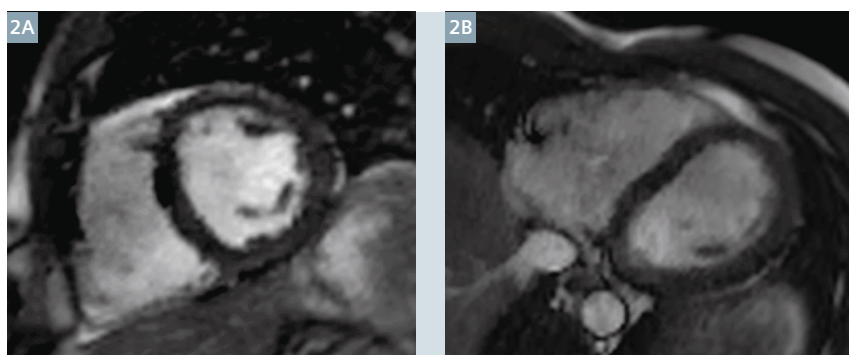
1. Fast acquisition covering the whole ventricle to avoid fatigue from exercise (maximum total exercise time 15 minutes);
2. Short duration of breath-holds to improve patient compliance and to minimize heart rate recovery during suspension of exercise;
3. ECG gating to enable segmented data in discrete cardiac phases for ventricular analysis using commercially available software;
4. Acceptable spatial resolution to delineate ventricular borders for analysis; and
5. Sufficient temporal resolution for accurate determination of end-diastole and end-systole at high heart rates.

To meet all the above requirements, the prototype CS_bSSFP protocol was modified for use under exercise conditions. Typical imaging parameters are given in Table 1. A net acceleration factor of 11.5 was achieved which enables whole heart coverage in one or two breath-holds (5-7 s duration depending on heart rate), with in-plane spatial resolution of 2 mm² and temporal resolution in the order of 20 ms. CS_bSSFP images in the LV short-axis (SAX) and modified RV SAX [13] are shown in Figure 2.

Exercise MRI protocol

Pre-MRI exercise testing

Prior to the exercise cardiac MRI, a cardiopulmonary exercise test (CPET) is performed outside the MRI room using a portable metabolic system (Metamax, Cortex BXB, Leipzig, Germany) and an MRI cycle ergometer (Lode, Groningen, The Netherlands). The maximal workload achievable by the patient is determined and then used to calculate the sub-maximal workloads for exercise cardiac MRI. Typically, this is between 25-60 W.



2 Midventricular LV short-axis and modified RV short-axis images from the highly accelerated CS_bSSFP acquisition (net acceleration 11.5) at end-diastole from the same patient.

During CPET, the patient is coached by the physiotherapist to hold their breath without valsalva breathing. This is to reduce the potential for intra-thoracic pressure increasing during breath-hold, which in turn could cause reduced venous return and cardiac output.

MRI protocol

After a recovery period, the patient is positioned in the MRI scanner (1.5T, MAGNETOM Aera). ECG and blood oxygen saturation (SPO₂) monitoring is used throughout the examination under the supervision of a cardiologist. After cardiac localizers are obtained, both LV short axis and modified RV short axis stacks are acquired at rest and two pre-determined submaximal workloads (Rest: 0 W, Exercise 1: 25 W and Exercise 2: 40-60 W). In order to achieve steady-state exercise response, subjects cycle at each workload for 3 minutes prior to image acquisition. Between breath-holds, subjects resume cycling for 45 s to return to steady-state exercise response (Fig. 3).

Exercise MRI Analysis

Image analysis is performed off-line using cvi⁴² software (Circle Cardiovascular Imaging, Calgary, Canada) and all standard measurements of cardiac function are obtained.

Clinical feasibility

In pilot testing, we demonstrated that this exercise MRI protocol is feasible in patients, healthy controls and in well-trained athletes, with clinically acceptable image quality (Fig. 4). Exercise ergometry within the MRI scanner is well tolerated and breath-holds during image acquisition are achievable at submaximal exertion. Quantitative ventricular data and dynamic ventricular response during exercise can be determined using the ultrafast prototype CS_bSSFP sequence.

Clinical applications and potential

Insights from analysis of pressure-volume loops have demonstrated that a ventricle that adapts well is able to increase its contractility to match the chronic increase in afterload and

its preservation is important in maintaining ventricular efficiency [14]. Ventricular systolic function adaptation to afterload can be tested dynamically to determine a contractile reserve, the capacity to increase contractility at a given level of loading. Contractile reserve has been shown to be a strong prognostic predictor in patients with left heart failure [15].

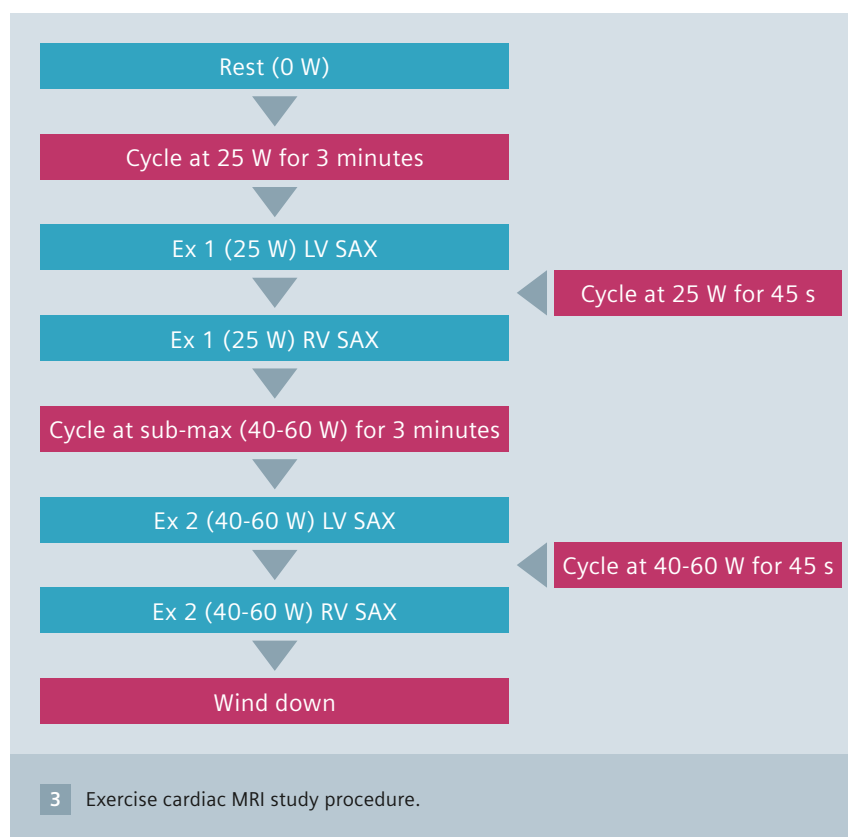
Assessment of RV function during exercise may provide an early indication of RV dysfunction and add incremental value in the clinical assessment of patients with right heart disease. In the setting of a chronic pressure overload state such as in pulmonary arterial hypertension (PAH), RV contractile reserve may be a more sensitive marker of hemodynamic ventricular dysfunction.

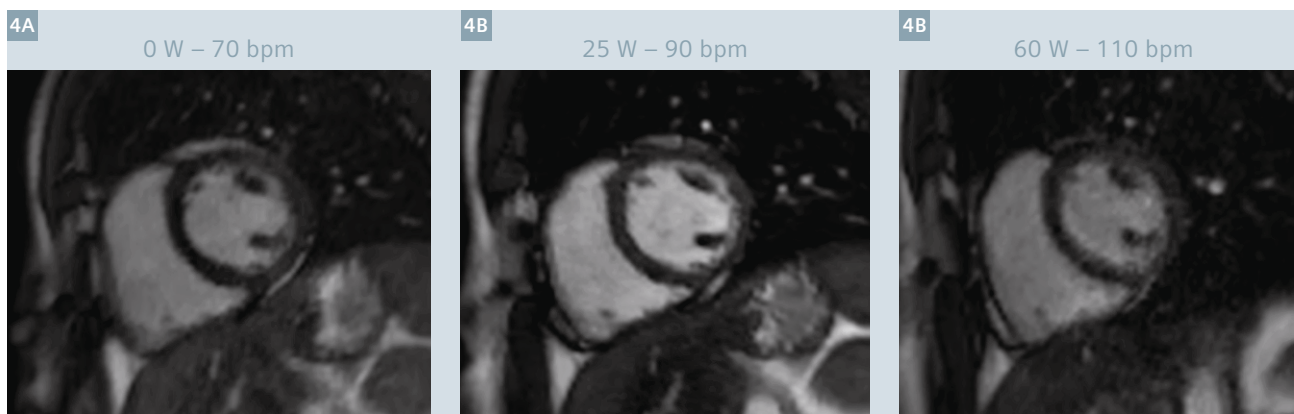
Currently, there is limited data on RV function during exercise and RV contractile reserve, largely due to the limitations of imaging during exercise. In a small study of pulmonary arterial hypertension (PAH) patients and normal controls, we demonstrated that although having near-normal ventricular function at rest, PAH patients were unable to increase their RV contractile function during exercise [16] (Fig. 5).

Exercise MRI also has the potential to predict adverse surgical outcomes in patients with congenital heart disease undergoing valve replacement surgery. The surgical outcome is likely to be better in patients with a ventricle shown to have contractile reserve. Exercise MRI may enable better-informed decisions about the timing of surgical and therapeutic interventions by detecting early ventricular impairment during exercise (particularly in the right ventricle). By providing information on ventricular contractile reserve, exercise MRI may facilitate improved prognostication of patients and has the potential to predict adverse surgical outcomes.

Conclusions

We have demonstrated that a highly accelerated imaging sequence using compressed sensing can facilitate clinically useful dynamic assessment of biventricular response during exercise with a reliability that was not previously possible.

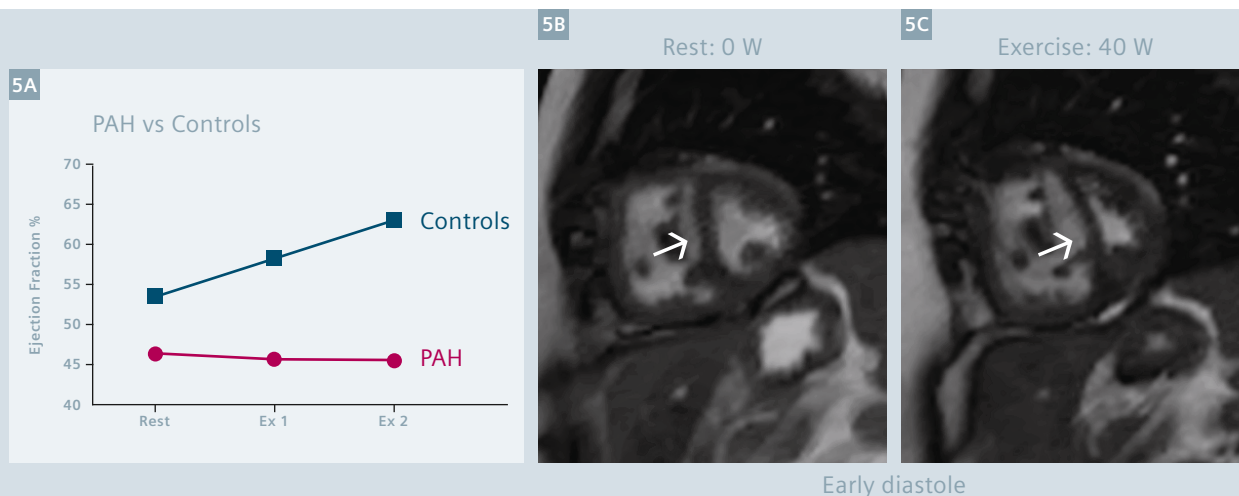




4A-C Midventricular LV short-axis images at rest and two submaximal workloads at end-diastole using the CS_bSSFP acquisition in a male control.



4D-F Midventricular modified RV short-axis images at rest and two submaximal workloads at end-diastole using the CS_bSSFP acquisition in a female control.



5 **5A:** Exercise MRI unmasks RV dysfunction not evident at rest in patients with pulmonary arterial hypertension (PAH): Despite having near-normal RV function at rest, PAH patients were unable to increase their RV contractile function during exercise.

5B, C: Midventricular LV short-axis images showing a left-ward deviation of the interventricular septum in early diastole during sub-maximal workload in a pulmonary arterial hypertension patient.

Acknowledgments

- Dr Benjamin Schmitt, Collaboration Manager & Scientific Team Leader MR, Siemens Healthcare ANZ, for technical support with CS sequence.
- Dr Richard Slaughter, Radiologist, for clinical advice and expertise.
- Mr Andrew Trotter for assistance with MR protocol development and clinical implementation.
- Professor Norman Morris and Ms Helen Seale (physiotherapists) for assistance with exercise protocol development and clinical implementation.
- The Prince Charles Hospital Foundation for support to purchase the MRI cycle ergometer and ongoing support for the exercise MRI program.
- Staff of the Richard Slaughter Centre of Excellence in Cardiovascular MRI for their continued support and dedication.

References

- Grothues F, Smith GC, Moon JC, Bellenger NG, Collins P, Klein HU, et al. Comparison of interstudy reproducibility of cardiovascular magnetic resonance with two-dimensional echocardiography in normal subjects and in patients with heart failure or left ventricular hypertrophy. *The American journal of cardiology*. 2002;90(1):29-34.
- Gardner BI, Bingham SE, Allen MR, Blatter DD, Anderson JL. Cardiac magnetic resonance versus transthoracic echocardiography for the assessment of cardiac volumes and regional function after myocardial infarction: an intrasubject comparison using simultaneous intrasubject recordings. *Cardiovascular ultrasound*. 2009;7:38.
- Rayatzadeh H, Patel SJ, Hauser TH, Ngo LL, Shaw JL, Tan A, et al. Volumetric left ventricular ejection fraction is superior to 2-dimensional echocardiography for risk stratification of patients for primary prevention implantable cardioverter-defibrillator implantation. *The American journal of cardiology*. 2013;111(8):1175-9.
- Jiang, L., Handschumacher, M.D., Hibberd, M.G., et al. (1994). Three-dimensional Echocardiographic Reconstruction of Right Ventricular Volume: In Vitro Comparison with Two-dimensional Methods. *J. Am. Soc. Echocardiography*. 7:150-158.
- Pennell, D.J. (2002). Ventricular Volume and Mass by CMR. *J. Cardiovasc. Magn. Reson.* 4(4):507-513.
- Niwa, K., Uchishiba, M., Aotsuka, H., Tobita, K., Matsuo, K., Fujiwara, T., Tatenno, S., Hamada, H. (1996). Measurement of Ventricular Volumes by Cine Magnetic Resonance Imaging in Complex Congenital Heart Disease with Morphologically Abnormal Ventricles. *Am. Heart Journal*. 131(3):567-575.
- La Gerche A, Claessen G, Van de Bruaene A, et al. Cardiac MRI: a new gold standard for ventricular volume quantification during high-intensity exercise. *Circulation. Cardiovascular imaging*. Mar 1 2013;6(2):329-338.
- Donoho D. Compressed sensing. *IEEE Transactions on Information Theory*. 2006;Vol. 52:1289-1306.
- Candes E, Romberg J, and Tao T. Robust uncertainty principles: Exact signal reconstruction from highly incomplete frequency information. *IEEE Transactions on Information Theory*. 2006;Vol. 52:489-509.
- Lustig M, Donoho D, Pauly JM. Sparse MRI: The application of compressed sensing for rapid MR imaging. *Magnetic resonance in medicine : official journal of the Society of Magnetic Resonance in Medicine / Society of Magnetic Resonance in Medicine*. Dec 2007;58(6):1182-1195.
- Vincenti G, Monney P, Chaptin J, Rutz T, Coppo S, Zenge MO, et al. Compressed sensing single-breath-hold CMR for fast quantification of LV function, volumes, and mass. *JACC Cardiovascular imaging*. 2014;7(9):882-92.
- Lin ACW, Strugnell WE, Riley R, Schmitt B, Zeng M, Schmidt M, et al. High Resolution Cine Imaging with Compressed Sensing for Accelerated Clinical Left Ventricular Evaluation. *JMRI 2016* (under review/revision).
- Strugnell WE, Slaughter RE, Riley RA, Trotter AJ, Bartlett H. Modified RV short axis series--a new method for cardiac MRI measurement of right ventricular volumes. *Journal of cardiovascular magnetic resonance : official journal of the Society for Cardiovascular Magnetic Resonance*. 2005;7(5):769-774.
- Kuehne T, Yilmaz S, Steendijk P, et al. Magnetic resonance imaging analysis of right ventricular pressure-volume loops: in vivo validation and clinical application in patients with pulmonary hypertension. *Circulation*. Oct 5 2004;110(14):2010-2016.
- Haddad F, Vrtovc B, Ashley EA, Deschamps A, Haddad H, Denault AY. The concept of ventricular reserve in heart failure and pulmonary hypertension: an old metric that brings us one step closer in our quest for prediction. *Current opinion in cardiology*. Mar 2011;26(2):123-131.
- Lin ACW, Strugnell WE, Seale H, Schmitt B, Schmidt M, O'Rourke R, et al. Exercise Cardiac MRI Derived Right Ventriculo-Arterial Coupling Ratio Detects Early Right Ventricular Maladaptation in Pulmonary Arterial Hypertension. *ERJ 2016* (in press).

Contact

Ms Wendy Strugnell
Richard Slaughter Centre of Excellence in
Cardiovascular Magnetic Resonance Imaging
The Prince Charles Hospital
627 Rode Rd
Chermside QLD 4032
Australia
Phone: +61-7-3139 6849
wendy.strugnell@health.qld.gov.au



Wendy Strugnell



Aaron Lin

Accelerated Segmented Cine TrueFISP of the Heart on a 1.5T MAGNETOM Aera Using *k-t*-sparse SENSE

Maria Carr¹; Bruce Spottiswoode²; Bradley Allen¹; Michaela Schmidt²; Mariappan Nadar⁴; Qiu Wang⁴; Jeremy Collins¹; James Carr¹; Michael Zenge²

¹Northwestern University, Feinberg School of Medicine, Chicago, IL, USA

²Siemens Healthineers

³Siemens Corporate Technology, Princeton, United States

Introduction

Cine MRI of the heart is widely regarded as the gold standard for assessment of left ventricular volume and myocardial mass and is increasingly utilized for assessment of cardiac anatomy and pathology as part of clinical routine. Conventional cine imaging approaches typically require 1 slice per breath-hold, resulting in lengthy protocols for complete cardiac coverage. Parallel imaging allows some shortening of the acquisition time, such that 2–3 slices can be acquired in a single breath-hold. In cardiac cine imaging artifacts become more prevalent with increasing acceleration factor. This will negatively impact the diagnostic utility of the images and may reduce accuracy of quantitative measurements. However, regularized iterative reconstruction

techniques can be used to considerably improve the images obtained from highly undersampled data. In this work, L1-regularized iterative SENSE as proposed in [1] was applied to reconstruct under-sampled *k*-space data. This technique¹ takes advantage of the de-noising characteristics of Wavelet regularization and promises to very effectively suppress sub-sampling artifacts. This may allow for high acceleration factors to be used, while diagnostic image quality is preserved.

The purpose of this study was to compare segmented cine TrueFISP images from a group of volunteers and patients using three acceleration and reconstruction approaches: iPAT factor 2 with conventional reconstruction; T-PAT factor 4 with conven-

tional reconstruction; and T-PAT factor 4 with iterative *k-t*-sparse SENSE reconstruction.

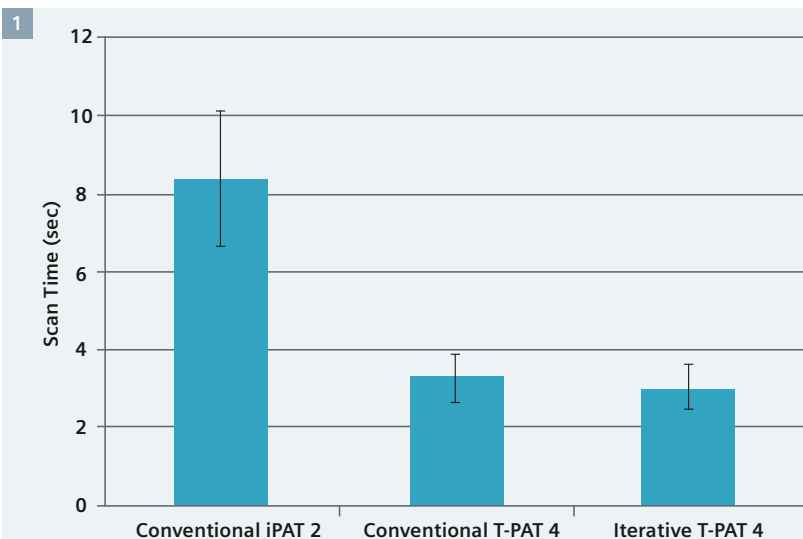
Technique

Cardiac MRI seems to be particularly well suited to benefit from a group of novel image reconstruction methods known as compressed sensing [2] which promise to significantly speed up data acquisition. Compressed sensing methods were introduced to MR imaging [3, 4] just a few years ago and have since been successfully combined with parallel imaging [5, 6]. Such methods try to utilize the

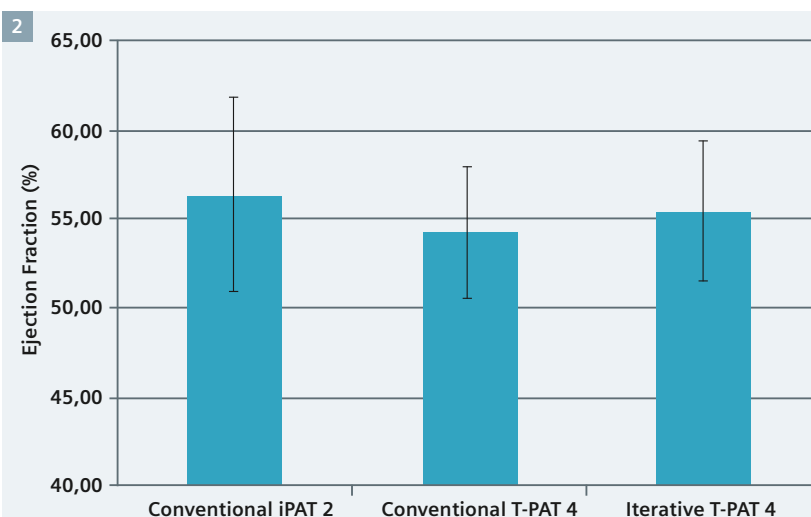
¹ 510(k) pending. Compressed Sensing Cardiac Cine is not commercially available. Future availability cannot be guaranteed.

Table 1: MRI conventional and iterative imaging parameters

Parameters	Conventional iPAT 2	Conventional T-PAT 4	Iterative T-PAT 4
Iterative recon	No	No	Yes
Parallel imaging	iPAT2 (GRAPPA)	TPAT4	TPAT4
TR/TE (ms)	3.2 / 1.6	3.2 / 1.6	3.2 / 1.6
Flip angle (degrees)	70	70	70
Pixel size (mm ²)	1.9 × 1.9	1.9 × 1.9	1.9 × 1.9
Slice thickness (mm)	8	8	8
Temp. res. (msec)	38	38	38
Acq. time (sec)	7	3.2	3.2



1 Single slice scan time in patients and volunteers. There was a statistically significant reduction in scan time compared to the standard iPAT2 for both TPAT4 acceleration and iterative reconstruction TPAT4 acceleration.



2 Ejection fraction in volunteers. Quantitatively measured ejection fractions were comparable across all three techniques.

full potential of image compression during the acquisition of raw input data. In the case of highly subsampled input data, a non-linear iterative optimization avoids sub-sampling artifacts during the process of image reconstruction. The resulting images represent the best solution consistent with the input data, which have a sparse representation in a specific transform domain. In the most favorable case, residual artifacts are not visibly perceptible or are diagnostically irrelevant.

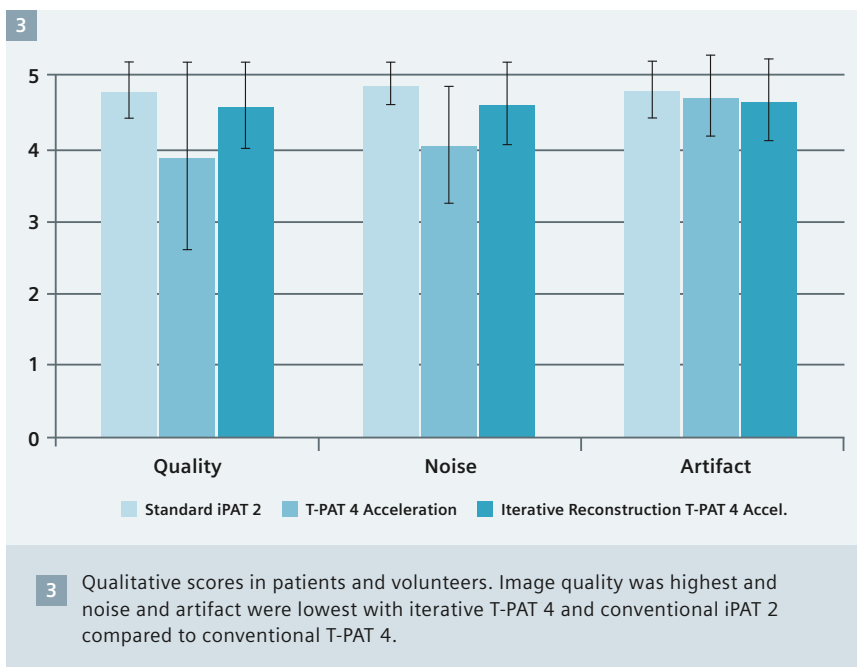
As outlined by Liu et al. in [1], the image reconstruction can be formulated as an unconstrained optimization problem. In the current implementation, this optimization is solved using a Nesterov-type algorithm [7]. The L1-regularization with a redundant Haar transform is efficiently solved using a Dykstra-type algorithm [8]. This allowed a smooth integration into the current MAGNETOM platform and, therefore, facilitates a broad clinical evaluation.

Materials and methods

Nine healthy human volunteers (57.4 male/56.7 female) and 20 patients (54.4 male/40.0 female) with suspected cardiac disease were scanned on a 1.5T MAGNETOM Aera system under an approved institutional review board protocol. All nine volunteers and 16 patients were imaged using segmented cine TrueFISP sequences with conventional GRAPPA factor 2 acceleration (conventional iPAT 2) T-PAT factor 4 acceleration (conventional T-PAT 4), and T-PAT factor 4 acceleration with iterative *k*-t-sparse SENSE reconstruction (iterative T-PAT 4). The remaining 4 patients were scanned using only conventional iPAT 2 and iterative T-PAT 4 techniques. Note that the iterative technique is fully integrated into the standard reconstruction environment.

The imaging parameters for each imaging sequence are provided in Table 1. All three sequences were run in 3 chamber and 4 chamber views, as well as a stack of short axis slices.

Quantitative analysis was performed on all volunteer data sets at a *syngo* MultiModality Workplace (Leonardo) using Argus post-processing software (Siemens Healthcare, Erlangen, Germany) by an experienced cardiovascular MRI technician. Ejection fraction, end-diastolic volume, end-systolic volume, stroke volume, cardiac output, and myocardial mass were calculated. In all volunteers and patients,



blinded qualitative scoring was performed by a radiologist using a 5 point Likert scale to assess overall image quality (1 – non diagnostic; 2 – poor; 3 – fair; 4 – good; 5 – excellent). Images were also scored for artifact and noise (1 – severe; 2 – moderate; 3 – mild; 4 – trace; 5 – none).

All continuous variables were compared between groups using an unpaired t-test, while ordinal qualitative variables were compared using a Wilcoxon signed-rank test.

Results

All images were acquired successfully and image quality was of diagnostic quality in all cases. The average scan time per slice for conventional iPAT 2, conventional T-PAT 4 and iterative T-PAT 4 were for patients 7.7 ± 1.5 sec, 5.6 ± 1.5 sec and 2.9 ± 1.5 sec and for the volunteers 9.8 ± 1.5 sec, 3.2 ± 1.5 sec and 3.0 ± 1.5 sec, respectively. The results in scan time are illustrated in Figure 1. In both patients and volunteers, conventional iPAT 2 were significantly longer than both conventional T-PAT 4 and iterative T-PAT 4 techniques ($p < 0.001$ for each group).

The results for ejection fraction (EF) for all three imaging techniques are provided in Figure 2. The average EF for conventional T-PAT 4 was slightly lower than that measured for conventional iPAT 2 and iterative T-PAT, but the group size is relatively small (9 subjects) and this difference was not significant ($p = 0.34$ and $p = 0.22$ respectively). There was no statistically significant difference in ejection fraction between the conventional iPAT 2 and the iterative T-PAT 4 sequences ($p = 0.48$).

The results for image quality, noise and artifact are provided in Figure 3. The iterative T-PAT 4 images had comparable image quality, noise and artifact scores compared to the conventional iPAT 2 images. The conventional T-PAT 4 images had lower image quality, more artifacts and higher noise compared to the other techniques.

Figures 4 and 5 show an example of 4-chamber and mid-short axis images from all three techniques in a patient with basal septal hypertrophy. In both series, the conventional iPAT 2 and iterative T-PAT 4 images are comparable in quality, while the conventional T-PAT 4 image is visibly noisier.

Discussion

This study compares a novel accelerated segmented cine TrueFISP technique to conventional iPAT 2 cine TrueFISP and T-PAT 4 cine TrueFISP in a cohort of normal subjects and patients. The iterative reconstruction technique provided comparable measurements of ejection fraction to the clinical gold standard (conventional iPAT 2). The accelerated segmented cine TrueFISP with T-PAT 4, which was used as comparison technique, produced slightly lower EF values compared to the other techniques, although this was not found to be statistically significant. The iterative reconstruction produced comparable image quality, noise and artifact scores to the conventional reconstruction using iPAT 2. The conventional T-PAT 4 technique had lower image quality and higher noise scores compared to the other two techniques.

The iterative T-PAT 4 segmented cine technique allows for greater than 50% reduction in acquisition time for comparable image quality and spatial resolution as the clinically used iPAT 2 cine TrueFISP technique. This iterative technique could be extended to permit complete heart coverage in a single breath-hold thus greatly simplifying and shortening routine clinical cardiac MRI protocols, which has been one of the biggest obstacles to wide acceptance of cardiac MRI. With a shorter cine acquisition, additional advanced imaging techniques, such as perfusion and flow, can be more readily added to patient scans within a reasonable protocol length.

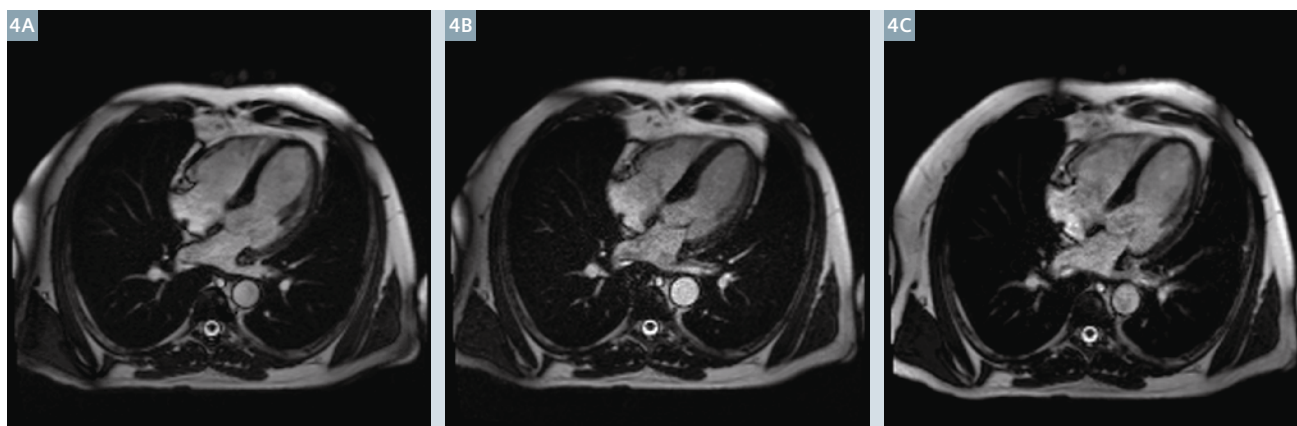
There are currently some limitations to the technique. Firstly, the use of SENSE implies that aliasing artifacts can occur if the field-of-view is smaller than the subject, which is sometimes difficult to avoid in the short axis orientation. But a solution to this is promised to be part of a future release of the current prototype. Secondly, the image reconstruction times of the current implementation seems to be prohibitive for routine clinical use. However, we anticipate future algorithmic

improvements with increased computational power to reduce the reconstruction time to clinically acceptable values.

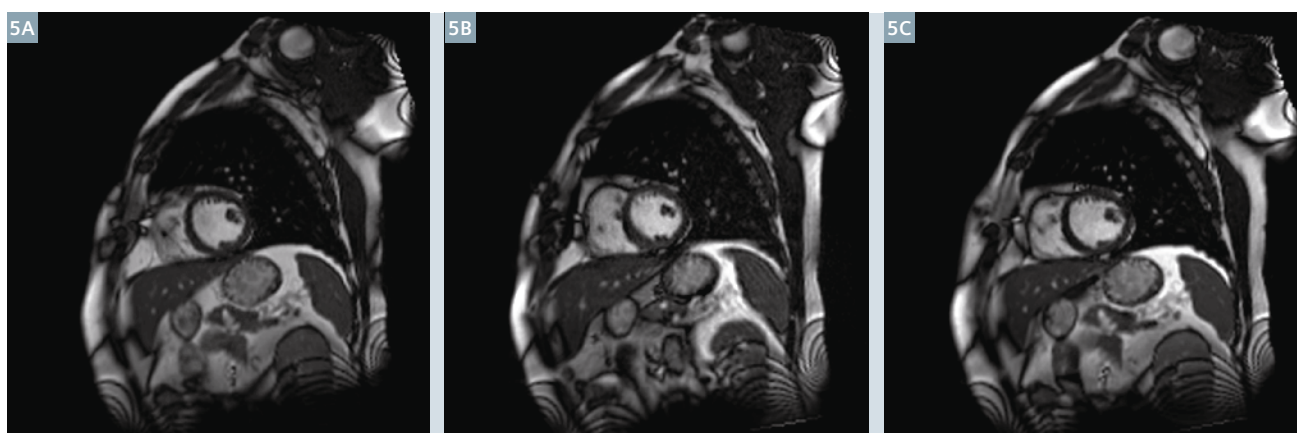
Of course, iterative reconstruction techniques are not just limited to cine imaging of the heart. Future work may see this technique applied to time intense techniques such as 4D flow phase contrast MRI and 3D coronary MR angiography, making them more clinically applicable. Furthermore, higher acceleration rates might be achieved by using an incoherent sampling pattern [9].

With sufficiently high acceleration, the technique can also be used effectively for real time cine cardiac imaging in patients with breath-holding difficulties or arrhythmia. Figure 6 shows that real-time acquisition with T-PAT 6 and *k-t* iterative reconstruction still results in excellent image quality.

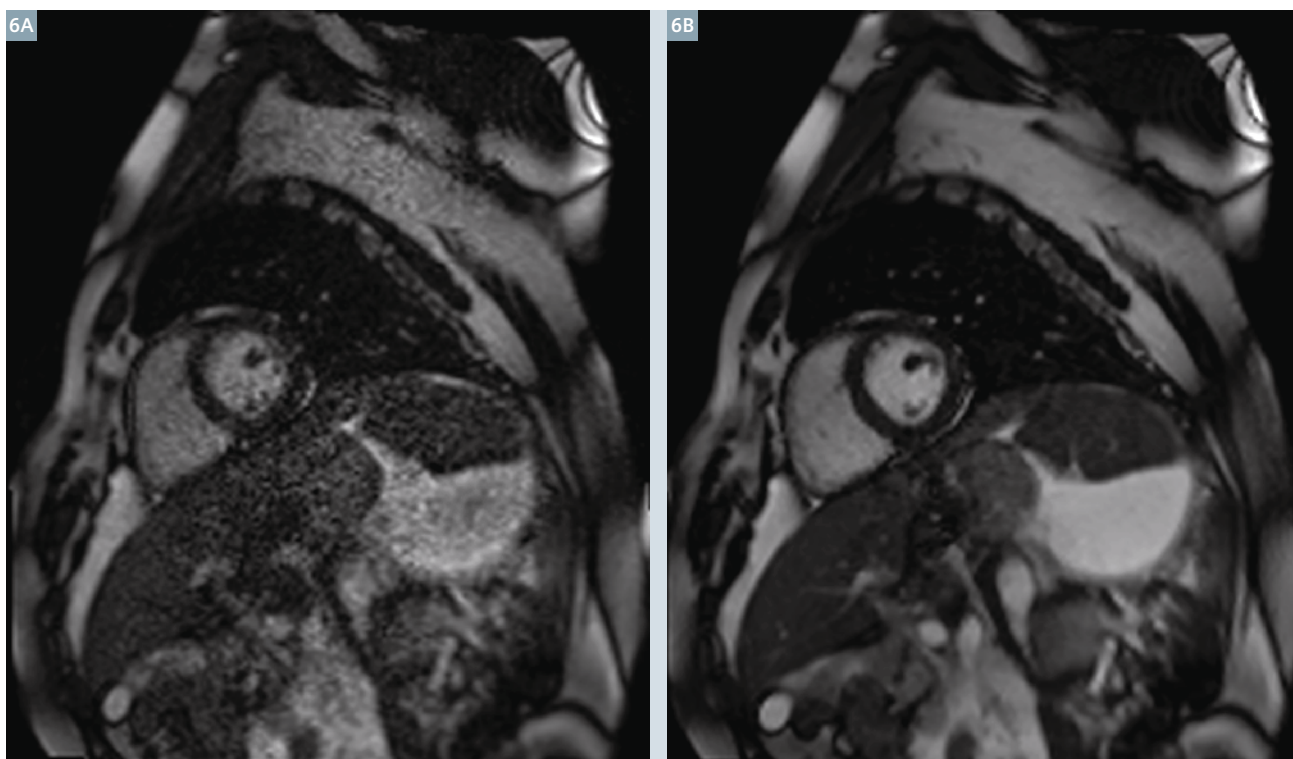
In conclusion, cine TrueFISP of the heart with inline *k-t*-sparse iterative reconstruction is a promising technique for obtaining high quality cine images at a fraction of the scan time compared to conventional techniques.



4 Four chamber cine TrueFISP from a normal volunteer. (4A) Conventional iPAT 2, acquisition time 8 s. (4B) Conventional T-PAT 4, acquisition time 3 seconds. (4C) Iterative T-PAT 4, acquisition time 3 seconds.



5 End-systolic short axis cine TrueFISP images from a patient with a history of myocardial infarction. A metal artifact from a previous sternotomy is noted in the sternum. There is wall thinning in the inferolateral wall with akinesia on cine views, consistent with an old infarct in the circumflex territory. (5A) Conventional iPAT 2, (5B) conventional T-PAT 4, (5C) iterative T-PAT 4.



6 Real-time cine TrueFISP T-PAT 6 images reconstructed using **(6A)** conventional, and **(6B)** iterative techniques.

Acknowledgement

The authors would like to thank Judy Wood, Manger of the MRI Department at Northwestern Memorial Hospital, for her continued support and collaboration with our ongoing research through the years. Secondly, we would like to thank the magnificent Cardiovascular Technologist's Cheryl Jarvis, Tinu John, Paul Magarity, Scott Luster for their patience and dedication to research. Finally, the Resource Coordinators that help us make this possible Irene Lekkas, Melissa Niemczura and Paulino San Pedro.

References

- 1 Liu J, Rapin J, Chang TC, Lefebvre A, Zenge M, Mueller E, Nadar MS. Dynamic cardiac MRI reconstruction with weighted redundant Haar wavelets. In Proceedings of the 20th Annual Meeting of ISMRM, Melbourne, Australia, 2002. p 4249.
- 2 Candes EJ, Wakin MB. An Introduction to compressive sampling. IEEE Signal Processing Magazine 2008. 25(2):21-30. doi: 10.1109/MSP.2007.914731.
- 3 Block KT, Uecker M, Frahm J. Undersampled Radial MRI with Multiple Coils. Iterative Image Reconstruction Using a Total Variation Constraint. Magn Reson Med 2007. 57(6):1086-98.
- 4 Lustig M, Donoho D, Pauly JM. Sparse MRI: The application of compressed sensing for rapid MR imaging. Magn Reson Med 2007. 58(6):1182-95.
- 5 Liang D, Liu B, Wang J, Ying L. Accelerating SENSE using compressed sensing. Magn Reson Med 2009. 62(6):154-84. doi: 10.1002/mrm.22161.
- 6 Lustig M, Pauly, JM. SPIRiT: Iterative self-consistent parallel imaging reconstruction from arbitrary k-space. Magn Reson Med 2010. 64(2):457-71. doi: 10.1002/mrm.22428.
- 7 Beck A, Teboulle M. A fast iterative shrinkage-thresholding algorithm for linear inverse problems. SIAM J Imaging Sciences 2009. 2(1): 183-202.
- 8 Dykstra RL. An algorithm for restricted least squares regression. J Amer Stat Assoc 1983 78(384):837-842.
- 9 Schmidt M, Ekinici O, Liu J, Lefebvre A, Nadar MS, Mueller E, Zenge MO. Novel highly accelerated real-time CINE-MRI featuring compressed sensing with k-t regularization in comparison to TSENSE segmented and real-time Cine imaging. J Cardiovasc Magn Reson 2013. 15(Suppl 1):P36.



Contact

Maria Carr, RT (CT)(MR)
CV Research Technologist
Department of Radiology
Northwestern University
Feinberg School of Medicine
737 N. Michigan Ave.
Suite 1600
Chicago, IL 60611
USA
Phone: +1 312-926-5292
m-carr@northwestern.edu

Preliminary Experiences with Compressed Sensing Multi-Slice Cine Acquisitions for the Assessment of Left Ventricular Function: CV_sparse WIP

G. Vincenti, M.D.¹; D. Piccini^{2,4}; P. Monney, M.D.¹; J. Chaptinel³; T. Rutz, M.D.¹; S. Coppo³; M. O. Zenge, Ph.D.⁴; M. Schmidt⁴; M. S. Nadar⁵; Q. Wang⁵; P. Chevre^{1,6}; M.; Stuber, Ph.D.³; J. Schwitter, M.D.¹

¹Division of Cardiology and Cardiac MR Center, University Hospital of Lausanne (CHUV), Lausanne, Switzerland

²Advanced Clinical Imaging Technology, Siemens Healthcare IM BM PI, Lausanne, Switzerland

³Department of Radiology, University Hospital (CHUV) and University of Lausanne (UNIL) / Center for Biomedical Imaging (CIBM), Lausanne, Switzerland

⁴MR Applications and Workflow Development, Healthcare Sector, Siemens AG, Erlangen, Germany

⁵Siemens Corporate Technology, Princeton, USA

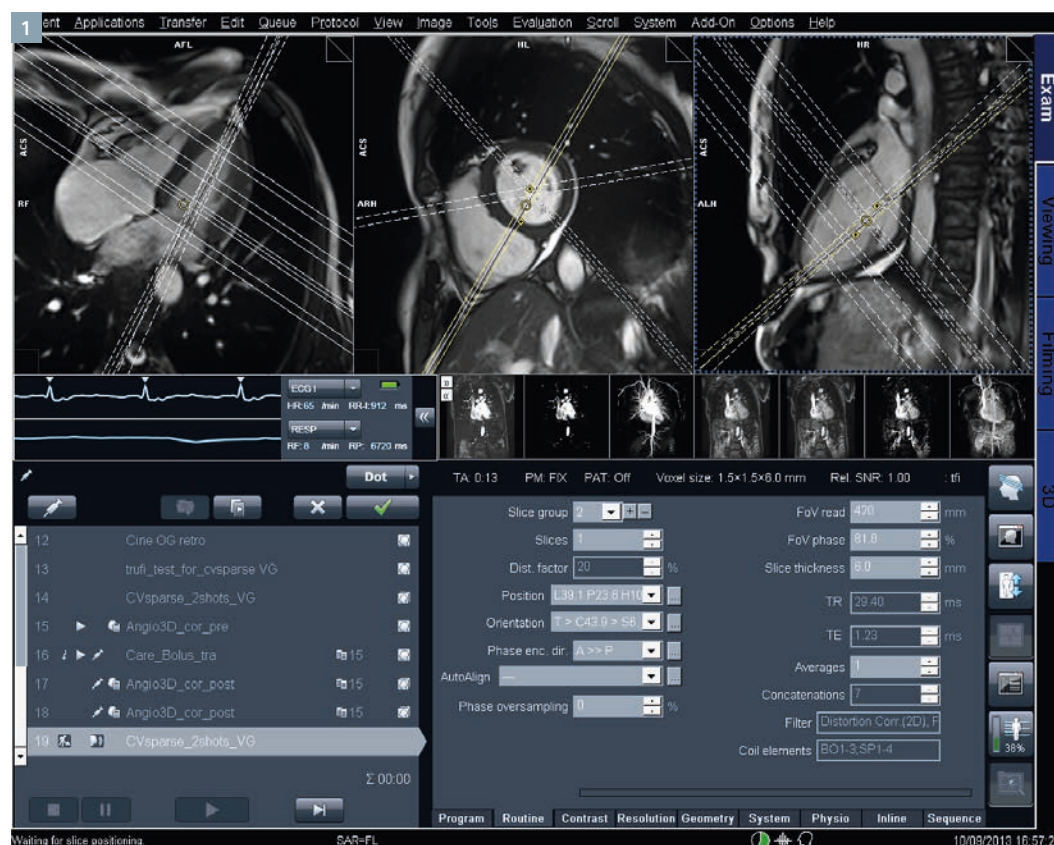
⁶Department of Radiology, University Hospital Lausanne, Switzerland

Introduction

Left ventricular (LV) ejection fraction is one of the most important measures in cardiology and part of every cardiac imaging evaluation as it is recognized as one of the strongest predictors of outcome [1]. It allows to assess the effect of established or novel treatments [2], and it is crucial for

decision making [3] e.g. to start [4] or stop [5] specific drug treatments or to implant devices [6]. CMR is generally accepted as the gold standard method to yield most accurate measures of LV ejection fraction and LV volumes. This capability and the additional value of CMR to character-

ize pathological myocardial tissue was the basis to assign a class 1 indication for patients with known or suspected heart failure to undergo CMR in the new Heart Failure Guidelines of the European Society of Cardiology [3].



1 Display of the planning of the 7 slices (4 short axis and 3 long axis slices) acquired within a single breath-hold with the three localizers.

The evaluation of LV volumes and LV ejection fraction are based on well-defined protocols [7] and it involves the acquisition of a stack of LV short axis cine images from which volumes are calculated by applying Simpson's rule. These stacks are typically acquired in multiple breath-holds. Quality criteria [8] for these functional images are available and are implemented e.g. for the quality assessment within the European CMR registry which currently holds approximately 33,000 patients and connects 59 centers [9].

Recently, compressed sensing (CS) techniques emerged as a means to considerably accelerate data acquisition without compromising significantly image quality. CS has three requirements:

- 1) transform sparsity,
- 2) incoherence of undersampling artifacts, and
- 3) nonlinear reconstruction (for details, see below).

Based on these prerequisites, a CS approach for the acquisition of cardiac cine images was developed and tested¹. In particular, the potential to acquire several slices covering the

heart in different orientations within a single breath-hold would allow to apply model-based analysis tools which theoretically could improve the motion assessment at the base of the heart, where considerable through-plane motion on short-axis slices can introduce substantial errors in LV volume and LV ejection fraction calculations. Conversely, with a multi-breath-hold approach, there are typically small differences in breath-hold positions which can introduce errors in volume and function calculations. The pulse sequence tested here allows for the acquisition of 7 cine slices within 14 heartbeats with an excellent temporal and spatial resolution.

Such a pulse sequence would also offer the advantage to obtain functional information in at least a single plane in patients unable to hold their breath for several heartbeats or in patients with frequent extrasystoles or atrial fibrillation. However, it should be mentioned that accurate quantitative measures of LV volumes and function cannot be obtained in highly arrhythmic hearts or in atrial fibrillation, as under such conditions volumes and ejection fraction change from beat to beat due to variable filling conditions. Nevertheless, rough estimates of LV volumes and function would still be desirable in arrhythmic patients.

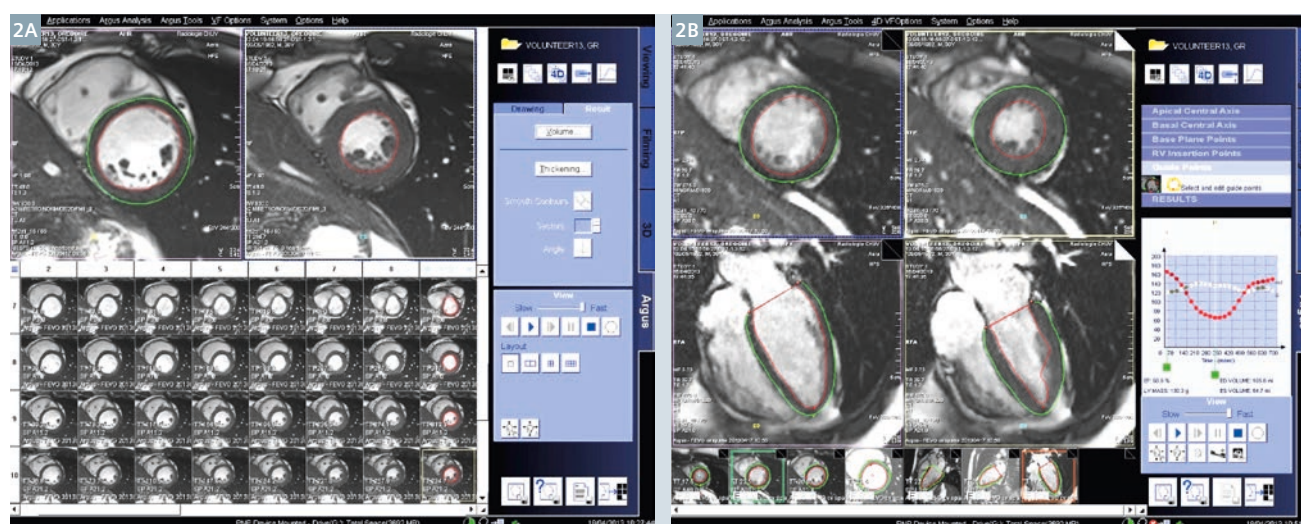
In a group of healthy volunteers and patients with different LV pathologies, the novel single-breath-hold CS cine approach was compared with the standard multi-breath-hold cine technique with respect to measure LV volumes and LV ejection fraction.

The CV_sparse work-in-progress (WIP)

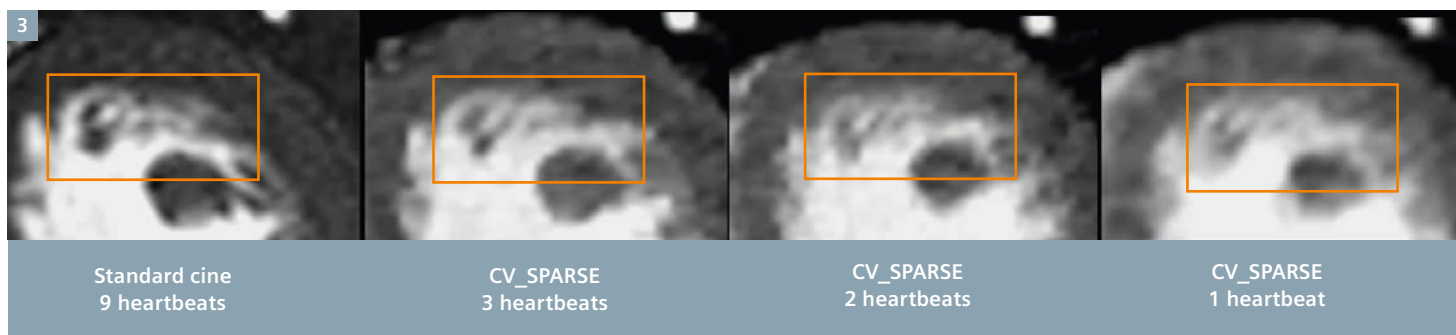
The CV_sparse WIP package implements sparse, incoherent sampling and iterative reconstruction for cardiac applications. This method in principle allows for high acceleration factors which enable triggered 2D real-time cine CMR while preserving high spatial and/or temporal resolution of conventional cine acquisitions. Compressed sensing methods exploit the potential of image compression during the acquisition of raw input data. Three components [10] are crucial for the concept of compressed sensing to work

I. Sparsity: In order to guarantee compressibility of the input data, sparsity must be present in a specific transform domain. Sparsity can be computed e.g. by calculating differences between neighboring pixels or by calculating finite differences in angiograms which then detect primarily vessel contours which typically represent a few percent of the

¹ At the time of publication CV_sparse was works-in-progress. Today, the product sequence Compressed Sensing Cardiac Cine is 510(k) pending and not commercially available. Future availability cannot be guaranteed.



2 Displays of the data analysis tools for the conventional short axis stack of cine images covering the entire LV (2A) and the 4D analysis tool (2B), which is model-based and takes long axis shortening of the LV, i.e. mitral annulus motion into account. Note that with both analysis tools, LV trabeculations are included into the LV volume, particularly in the end-diastolic images (corresponding images on the left of top row in 2A and 2B).



3 Examples of visualization of small trabecular structures in the LV (in the rectangle) with the standard cine SSFP sequence (image on the left) and the accelerated compressed sensing sequences (images on the right). Despite increasing acceleration most information on small intraluminal structures remains visible.

entire image data only. Furthermore, sparsity is not limited to the spatial domain: the acquisition of cine images of the heart can be highly sparsified in the temporal dimension.

II. Incoherent sampling: The aliasing artifacts due to k -space undersampling must be incoherent, i.e. noise-like, in that transform domain. Here, it is to mention that fully random k -space sampling is suboptimal as k -space trajectories should be smooth for hardware and physiological considerations. Therefore, incoherent sampling schemes must be designed to avoid these concerns while fulfilling the condition of random, i.e. incoherent sampling.

III. Reconstruction: A non-linear iterative optimization corrects for subsampling artifacts during the process of image reconstruction yielding to a best solution with a sparse representation in a specific transform domain and which is consistent with the input data. Such compressed sensing techniques can also be combined with parallel imaging techniques [11].

WIP CV_sparse sequence

The current CV_sparse sequence [12] realizes incoherent sampling by initially distributing the readouts pseudo-randomly on the Cartesian grid in k -space. In addition, for cine-CMR imaging, a pseudo-random offset is applied from frame-to-frame which results in an incoherent temporal jitter. Finally, a variable sampling density in k -space stabilizes the iterative reconstruction. To avoid eddy current effects for balanced steady-state free precession (bSSFP) acquisitions, pairing [13] can also be applied. Thus, the tested CV_sparse sequence is characterized by sparse, incoherent sampling in space and time, non-linear iterative reconstruction integrating SENSE, and L1 wavelet regularization in the phase encoding direction and/or the temporal dimension. With regard to reconstruction, the ICE program runs a non-linear iterative reconstruction with k - t regularization in space and time specifically modified for compressed sensing. The algorithm derives from a parallel imaging type reconstruction which takes coil sensitivity maps into account, thus supporting predominantly high acceleration factors. For cine CMR, no additional reference scans are needed because – similar to T-PAT – the coil sensitivity maps are calculated from the temporal average of the input data in a central region of k -space consisting of not

more than 48 reference lines.

The extensive calculations for image reconstruction typically running 80 iterations are performed online on all CPUs on the MARS computer in parallel, in order to reduce reconstruction times.

Volunteer and patient studies

In order to obtain insight into the image quality of single-breath-hold multi-slice cine CMR images acquired with the compressed sensing (CS) approach, we studied a group of healthy volunteers and a patient group with different pathologies of the left ventricle. In addition to the evaluation of image quality, the robustness and the precision of the CS approach for LV volumes and LV ejection fraction was also assessed in comparison with a standard high-resolution cine CMR approach. All CMR examinations were performed on a 1.5T MAGNETOM Aera (Siemens Healthcare, Erlangen, Germany). The imaging protocol consisted of a set of cardiac localizers followed by the acquisition of a stack of conventional short-axis SSFP cine images covering the entire LV with a spatial and tem-

poral resolution of $1.2 \times 1.6 \text{ mm}^2$, and approximately 40 ms, respectively (slice thickness: 8 mm; gap between slices: 2 mm). LV 2-chamber, 3-chamber, and 4-chamber long-axis acquisitions were obtained for image quality assessment but were not used for LV volume quantifications. As a next step, to test the new CS-based technique, slice orientations were planned to cover the LV with 4 short-axis slices distributed evenly over the LV long axis complemented by 3 long-axis slices (i.e. a 2-chamber, 3-chamber, and 4-chamber slice) (Fig. 1). These 7 slices were then acquired in a single breath-hold maneuver lasting 14 heart beats (i.e. 2 heart beats per slice) resulting in an acceleration factor of 11.0 with a temporal and spatial resolution of 30 ms and $1.5 \times 1.5 \text{ mm}^2$, respectively (slice thickness: 6 mm). As the reconstruction algorithm is susceptible to aliasing in the phase-encoding direction, the 7 slices were first acquired with a non-cine acquisition to check for correct phase-encoding directions and, if needed, to adjust the field-of-view

to avoid fold-over artifacts. After confirmation of correct imaging parameters, the 7-slice single-breath-hold cine CS-acquisition was performed. In order to obtain a reference for the LV volume measurement, a phase-contrast flow measurement in the ascending aorta was performed to be compared with the LV stroke volumes calculated from the standard and CS cine data.

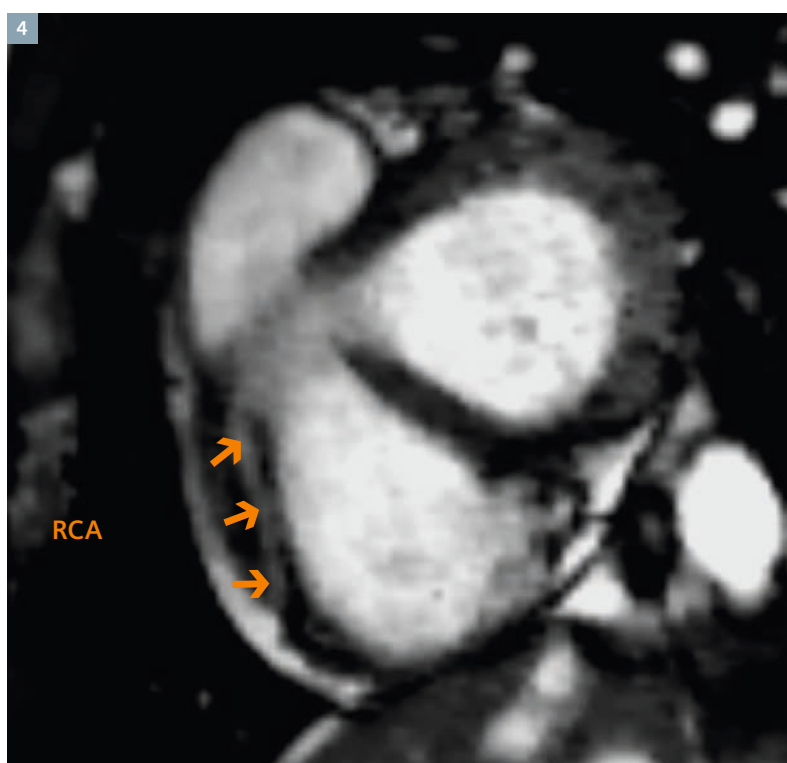
The conventional stack of cine SSFP images was analyzed by the Argus software (Siemens Argus 4D Ventricular Function, Fig. 2A). The CS cine data were analyzed by the 4D-Argus software (Siemens Argus, Fig. 2B). Such software is based on an LV model and, with relatively few operator interactions, the contours for the LV endocardium and epicardium are generated by the analysis tool. Of note, this 4D analysis tool automatically tracks the 3-dimensional motion of the mitral annulus throughout the cardiac cycle which allows for an accurate volume calculation particularly at the base of the heart.

Results and discussion

Image quality – robustness of the technique

Overall, a very good image quality of the single-breath-hold multi-slice CS acquisitions was obtained in the 12 volunteers and 14 patient studies. All CS data sets were of adequate quality to undergo 4D analysis. Small structures such as trabeculations were visualized in the CS data sets as shown in Figures 3 and 4. However, very small structures, detectable by the conventional cine acquisitions, were less well discernible by the CS images. Therefore, it should be mentioned here, that this accelerated single-breath-hold CS approach would be adequate for functional measurements, i.e. LV ejection fraction assessment (see also results below), whereas assessment of small structures as present in many cardiomyopathies is more reliable when performed on conventional cine images. Temporal resolution of the new technique appears adequate to even detect visually the dyssynchronous contraction pattern in left bundle branch block. Also, the image contrast between the LV myocardium and the blood pool was high on the CS images allowing for an easy assessment of the LV motion pattern. As a result, the single-breath-hold cine approach permits to reconstruct the LV in 3D space with high temporal resolution as illustrated in Figure 5. Since these data allow to correctly include the 3D motion of the base of the heart during the cardiac cycle, the LV stroke volume appears to be measurable by the CS approach with higher accuracy than with the conventional multi-breath-hold approach (see results below). With an accurate measurement of the LV stroke volume, the quantification of a mitral insufficiency should theoretically benefit (when calculating mitral regurgitant volume as 'LV stroke volume minus aortic forward-flow volume').

As a current limitation of the CS approach, its susceptibility for fold-over artifacts should be mentioned (Figs. 6A). Therefore, the field-of-view must cover the entire anatomy and thus, some penalty in spatial res-



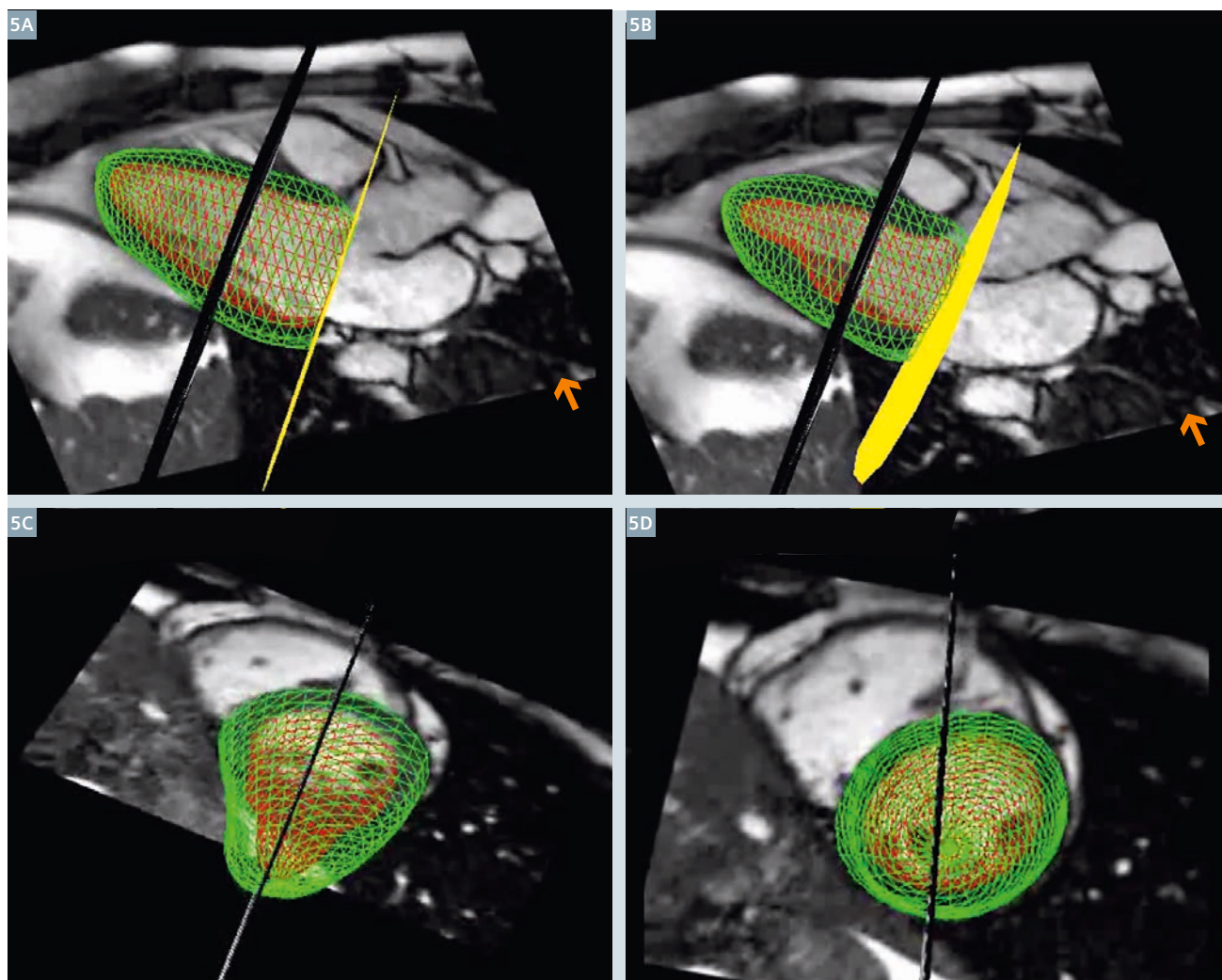
4 Example demonstrating the performance of the compressed sensing technique visualizing small structures such as the right coronary artery (RCA) with high temporal and spatial resolution acquired within 2 heart-beats. Short-axis view of the base of the heart (1 out of 17 frames).

olution may occur in relation to the patient's anatomy. In addition, the sparsity in the temporal domain may be limited in anatomical regions of very high flow, and therefore, in some acquisitions, flow-related artifacts occurred in the phase-encoding direction during systole (Figs. 6B, C). Also, in its current version, the sequence is prospective, thus it does not cover the very last phases of the cardiac cycle and the reconstruction times for the CS images lasted several minutes precluding an immediate assessment of the image data quality or using this image information to plan next steps of a CMR examination.

Performance of the single-breath-hold CS approach in comparison with the standard multi-breath-hold cine approach

From a quantitative point-of-view, the accurate and reliable measurement of LV volumes and function is crucial as many therapeutic decisions directly depend on these measures [3–6]. In this current relatively small study group, LV end-diastolic and end-systolic volumes measured by the single-breath-hold CS approach were comparable with those calculated from the standard multi-breath-

hold cine SSFP approach. LVEDV and LVESV differed by $10 \text{ ml} \pm 17 \text{ ml}$ and $2 \text{ ml} \pm 12 \text{ ml}$, respectively. Most importantly, LV ejection fraction differed by only $1.3 \pm 4.7\%$ (50.6% vs 49.3% for multi-breath-hold and single-breath-hold, respectively, $p = 0.17$; regression: $r = 0.96$, $p < 0.0001$; $y = 0.96x + 0.8 \text{ ml}$). Thus, it can be concluded that the single-breath-hold CS approach could potentially replace the multi-breath-hold standard technique for the assessment of LV volumes and systolic function.



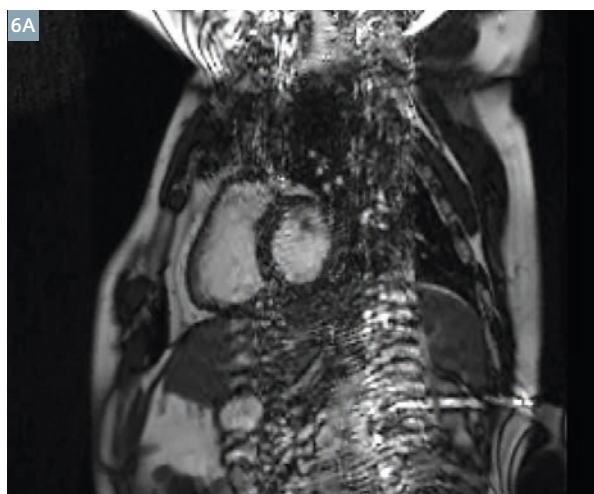
5 Display of the 3D reconstruction derived from the 7 slices acquired within a single breath-hold. Note the long-axis shortening of the LV during systole allowing for accurate LV volume measurements (5A, 5B, yellow plane). Any orientation of the 3D is available for inspection of function (5A–D).

What about the accuracy of the novel single-breath-hold CS technique?

To assess the accuracy of the LV volume measurements, LV stroke volume was compared with the LV output measured in the ascending aorta with phase-contrast MR. As the flow measurements were performed distally to the coronary arteries, flow in the coronaries was estimated as the LV mass multiplied by 0.8 ml/min/g. An excellent agreement was found with a mean of 86.8 ml/beat for the aortic flow measurement and 91.9 ml/beat for the LV measurements derived from the single-breath-hold CS data ($r = 0.93$, $p < 0.0001$). By Bland-Altman analysis, the stroke volume approach overestimated by 5.2 ml/beat versus the reference flow measurement. For the conventional stroke volume measurements, this difference was 15.6 ml/beat (linear regression analysis vs aortic flow: $r = 0.69$, $p < 0.01$). More importantly, the CS LV stroke data were not only more precise with a smaller mean difference, the variability of the CS data vs the reference flow data was less with a standard deviation as low as 6.8 ml/beat vs 12.9 ml/beat for the standard multi-breath-hold approach (Fig. 7). Several explanations may apply for the higher accuracy of the single-breath-hold multi-slice CS approach in comparison to the conventional multi-breath-hold approach:

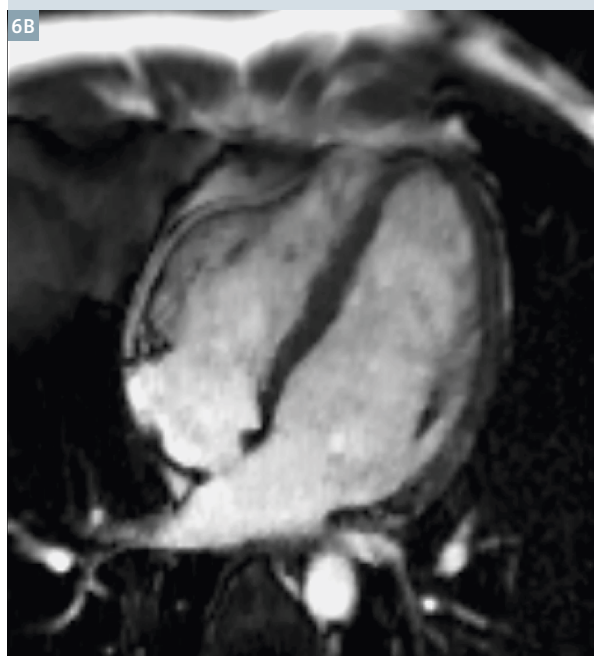
- 1) With the single-breath-hold approach, all acquired slices are correctly co-registered, i.e. they are correctly aligned in space, a prerequisite for the 4D-analysis tool to work properly.
- 2) This 4D-analysis tool allows for an accurate tracking of the mitral valve plane motion during the cardiac cycle

This reprinted article was based on an early works-in-progress CV_sparse prototype. In Compressed Sensing Cardiac Cine¹ the limitations such as fold-over artifacts as shown in Figure 6A have been remedied, and image reconstruction is faster and provides improved image quality.



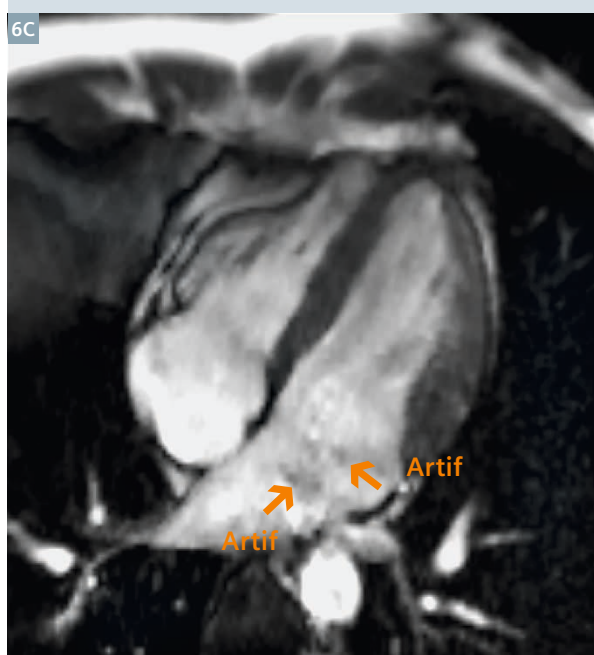
6A

A typical fold-over artifact along the phase-encoding direction in a short axis slice, oriented superior-inferior for demonstrative purpose.

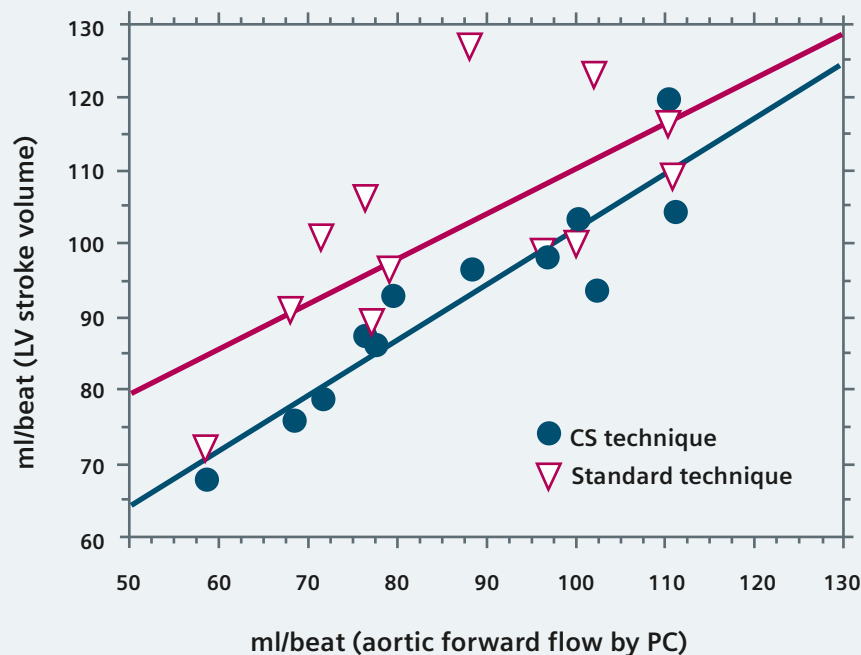


6B

No flow-related artifacts are visible on the end-diastolic phases, while small artifacts in phase-encoding direction (Artif, arrows) occur in mid-systole projecting over the mitral valve (6C).



LV stroke volume: comparison vs aortic forward flow



An excellent correlation is obtained for the LV stroke volume calculated from the compressed sensing data with the flow volume in the aorta measured by phase-contrast technique. Variability of the conventional LV stroke volume data appears higher than for the compressed sensing data.

as shown in Figure 5, which is important as the cross-sectional area of the heart at its base is large and thus, inaccurate slice positioning at the base of the heart with conventional short-axis slices typically translate in relatively large errors. Nevertheless, we observed a systematic overestimation of the stroke volume by the CS approach of 5.2 ml/beat in comparison to the flow measurements. In normal hearts with tricuspid aortic valves, an underestimation of aortic flow by the phase-contrast technique is very unlikely [14]. Thus, overestimation of stroke volume by the volume approach is to consider. In the volume contours, the papillary muscles are excluded as illustrated in Figure 8. As these papillary muscles are excluded in both the diastolic and systolic contours, this aspect should not affect net LV stroke volume. However, as shown in Figure 8, smaller trabecula-

tions of the LV wall are included into the LV blood pool contour in the diastolic phase, while these trabeculations, when compacted in the end-systolic phase, are excluded from the blood pool resulting in a small overestimation of the end-diastolic volume, and thus, LV stroke volume. This explanation is likely as Van Rossum et al. demonstrated a slight underestimation of the LV mass when calculated on end-diastolic phases versus end-systolic phases, as trabeculations in end-diastole are typically excluded from the LV walls [15].

In summary, this novel very fast acquisition strategy based on a CS technique allows to cover the entire LV with high temporal and spatial resolution within a single breath-hold. The image quality based on these preliminary results appears adequate to yield highly accurate measures

of LV volumes, LV stroke volume, LV mass, and LV ejection fraction. Testing of this very fast multi-slice cine approach for the atria and the right ventricle is currently ongoing. Finally, these preliminary data show that compressed sensing MR acquisitions in the heart are feasible in humans and compressed sensing might be implemented for other important cardiac sequences such as fibrosis/viability imaging, i.e. late gadolinium enhancement, coronary MR angiography, or MR first-pass perfusion.

The Cardiac MR Center of the University Hospital Lausanne

The Cardiac Magnetic Resonance Center (CRM) of the University Hospital of Lausanne (Centre Hospitalier Universitaire Vaudois; CHUV) was established in 2009. The CMR center is dedicated to high-quality clinical work-up of car-

diac patients, to deliver state-of-the-art training in CMR to cardiologists and radiologists, and to pursue research. In the CMR center education is provided for two specialties while focusing on one organ system. Traditionally, radiologists have focussed on using one technique for different organs, while cardiologists have concentrated on one organ and perhaps one technique. Now in the CMR center the focus is put on a combination of specialists with different background on one organ. Research at the CMR center is devoted to four major areas: the study of

- 1.) cardiac function and tissue characterization, specifically to better understand diastolic dysfunction,
- 2.) the development of MR-compatible cardiac devices such as pacemakers and ICDs;
- 3.) the utilization of hyperpolarized ^{13}C -carbon contrast media to investigate metabolism in the heart, and

4.) the development of ^{19}F -fluorine-based CMR techniques to detect inflammation and to label and track cells non-invasively.

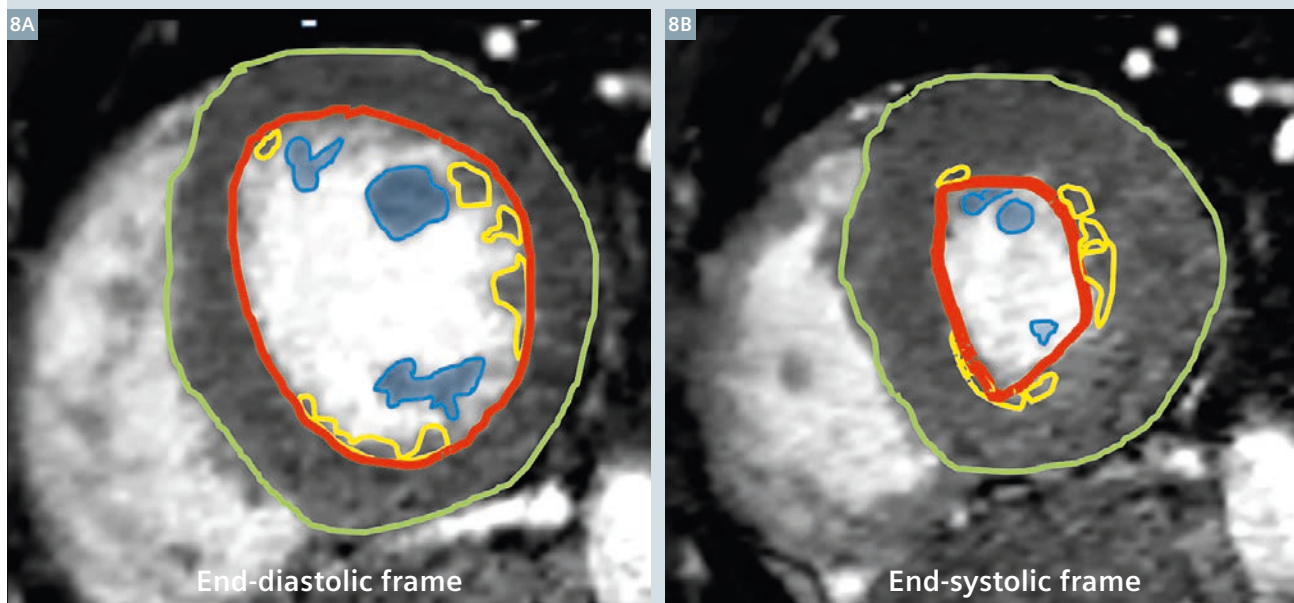
For the latter two topics, the CMR center established tight collaborations with the Center for Biomedical Imaging (CIBM), a network around Lake Geneva that includes the Ecole Polytechnique Fédérale de Lausanne (EPFL), and the universities and university hospitals of Lausanne and Geneva. In particular, strong collaborative links are in place with the CVMR team of Prof. Matthias Stuber, a part of the CIBM and located at the University Hospital Lausanne and with Prof. A. Comment, with whom we perform the studies on real-time metabolism based on the ^{13}C -carbon hyperpolarization (DNP) technique. In addition, collaborative studies are ongoing with the Heart Failure and Cardiac Transplantation Unit led by Prof. R. Hullin (detection of graft rejection by tissue characterization)

and the Oncology Department led by Prof. Coukos (T cell tracking by ^{19}F -MRI in collaboration with Prof. Stuber, R. van Heeswijk, CIBM, and Prof. O. Michielin, Oncology). This structure allows for a direct interdisciplinary interaction between physicians, engineers, and basic scientists on a daily basis with the aim to enable innovative research and fast translation of these techniques from bench to bedside.

The CMRC is also the center of competence for the quality assessment of the European CMR registry which holds currently approximately 33,000 patient studies acquired in 59 centers across Europe.

The members of the CMRC team are: Prof. J. Schwitler (director of the center), PD Dr. X. Jeanrenaud, Dr. D. Locca, MER, Dr. P. Monney, Dr. T. Rutz, Dr. C. Sierro, and Dr. S. Koestner (cardiologists, staff members),

LV short-axis slice: CV_SPARSE



- 8 Overestimation of end-diastolic LV volumes by volumetric measurements. In comparison to ejected blood from the LV as measured with phase-contrast techniques, the volumetric measurements of LV stroke volume overestimated by approximately 5 ml, most likely by overestimation of LV end-diastolic volume. Small trabeculations (yellow contours in 8A) are included into the LV blood volume (red contour in 8A) in diastole, while these trabeculations (yellow contours in 8B) are typically included in the end-systolic phase (red contours in 8B). For the same reasons, LV mass (= green contour minus red contour) is often slightly underestimated in diastole vs systole.

Dr. G. Vincenti (cardiologist) and Dr. N. Barras (cardiologist in training, rotation), PD. Dr. S. Muzzarelli (affiliated cardiologist), Prof. C. Beigelman and Dr. X. Boulanger (radiologists, staff members), Dr. G.L. Fetz (radiologist in training, rotation), C. Gonzales, PhD (¹⁹F-fluorine project leader), H. Yoshihara, PhD (¹³C-carbon project leader), V. Klinké (medical student, doctoral thesis), C. Bongard (medical student, master thesis), P. Chevre (chief CMR technician), and F. Recordon and N. Lauriers (research nurses).

Acknowledgements

The authors would like to thank all the members of the team of MR technologists at the CHUV for their highly valuable participation, helpfulness and support during the daily clinical CMR examinations and with the research protocols. Finally, a very important acknowledgment goes to Dr. Michael Zenge, Ms. Michaela Schmidt, and the whole Siemens MR Cardio team of Edgar Müller in Erlangen.

References

- Curtis JP, Sokol SI, Wang Y, Rathore SS, Ko DT, Jadbabaie F, Portnay EL, Marshalko SJ, Radford MJ, Krumholz HM. The association of left ventricular ejection fraction, mortality, and cause of death in stable outpatients with heart failure. *Journal of the American College of Cardiology*. 2003;42(4):736-42.
- Sürder D, Manka R, Lo Cicero V, Moccetti T, Rufibach K, Soncin S, Turchetto L, Radrizzani M, Astori G, Schwitter J, Erne P, Jamshidi P, Auf Der Maur C, Zuber M, Windecker S, Moschovitis A, Wahl A, Bühler I, Wyss C, Landmesser U, Lüscher T, Corti R. Intracoronary injection of bone marrow derived mononuclear cells, early or late after acute myocardial infarction: Effects on global LV-function: 4 months results of the SWISS-AMI trial. *Circulation*. 2013;127:1968-79.
- McMurray JJV, Adamopoulos S, Anker SD, Auricchio A, Böhm M, Dickstein K, Falk V, Filippatos G, Fonseca C, Sanchez MAG, Jaarsma T, Køber L, Lip GYH, Maggioni AP, Parkhomenko A, Pieske BM, Popescu BA, Rønnevik PK, Rutten FH, Schwitter J, Seferovic P, Stepinska J, Trindade PT, Voors AA, Zannad F, Zeiher A. ESC Guidelines for the diagnosis and treatment of acute and chronic heart failure 2012. *European Heart Journal*. 2012 May 19, 2012(33):1787-847.
- Zannad F, McMurray JJV, Krum H, van Veldhuisen DJ, Swedberg K, Shi H, Vincent J, Pocock SJ, Pitt B. Eplerenone in Patients with Systolic Heart Failure and Mild Symptoms. *New England Journal of Medicine*. 2011;364(1):11-21.
- Gharib MI, Burnett AK. Chemotherapy-induced cardiotoxicity: current practice and prospects of prophylaxis. *European Journal of Heart Failure*. 2002 June 1, 2002;4(3):235-42.
- Bardy GH, Lee KL, Mark DB, Poole JE, Packer DL, Boineau R, Domanski M, Troutman C, Anderson J, Johnson G, McNulty SE, Clapp-Channing N, Davidson-Ray LD, Fraulo ES, Fishbein DP, Luceri RM, Ip JH. Amiodarone or an Implantable Cardioverter-Defibrillator for Congestive Heart Failure. *New England Journal of Medicine*. 2005;352(3):225-37.
- Schwitter J. CMR-Update. 2. Edition ed. Lausanne, Switzerland. www.herz-mri.ch.
- Klinké V, Muzzarelli S, Lauriers N, Locca D, Vincenti G, Monney P, Lu C, Nothnagel D, Pilz G, Lombardi M, van Rossum A, Wagner A, Bruder O, Mahrholdt H, Schwitter J. Quality assessment of cardiovascular magnetic resonance in the setting of the European CMR registry: description and validation of standardized criteria. *Journal of Cardiovascular Magnetic Resonance*. 2013;15(1):55.
- Bruder O, Wagner A, Lombardi M, Schwitter J, van Rossum A, Pilz G, Nothnagel D, Steen H, Petersen S, Nagel E, Prasad S, Schumm J, Greulich S, Cagnolo A, Monney P, Deluigi C, Dill T, Frank H, Sabin G, Schneider S, Mahrholdt H. European Cardiovascular Magnetic Resonance (EuroCMR) registry-multi national results from 57 centers in 15 countries. *J Cardiovasc Magn Reson*. 2013;15:1-9.
- Lustig M, Donoho D, Pauly JM. Sparse MRI: The application of compressed sensing for rapid MR imaging. *Magnetic Resonance in Medicine*. 2007;58(6):1182-95.
- Liang D, Liu B, Wang J, Ying L. Accelerating SENSE using compressed sensing. *Magnetic Resonance in Medicine*. 2009;62(6):1574-84.
- Liu J. Dynamic cardiac MRI reconstruction with weighted redundant Haar wavelets. *Magn Reson Med*. 2012;Proc. ISMRM 2012,abstract.
- Bieri O, Markl M, Scheffler K. Analysis and compensation of eddy currents in balanced SSFP. *Magn Reson Med*. 2005;54:129-37.
- Muzzarelli S, Monney P, O'Brien K, Faletta F, Moccetti T, Vogt P, Schwitter J. Quantification of aortic valve regurgitation by phase-contrast magnetic resonance in patients with bicuspid aortic valve: where to measure the flow? . *Eur Heart J - CV Imaging*. 2013;in press.
- Papavassiliu T, Kühl HP, Schröder M, Süselbeck T, Bondarenko O, Böhm CK, Beek A, Hofman MMB, van Rossum AC. Effect of Endocardial Trabeculae on Left Ventricular Measurements and Measurement Reproducibility at Cardiovascular MR Imaging. *Radiology*. 2005 July 1, 2005;236(1):57-64.



Contact

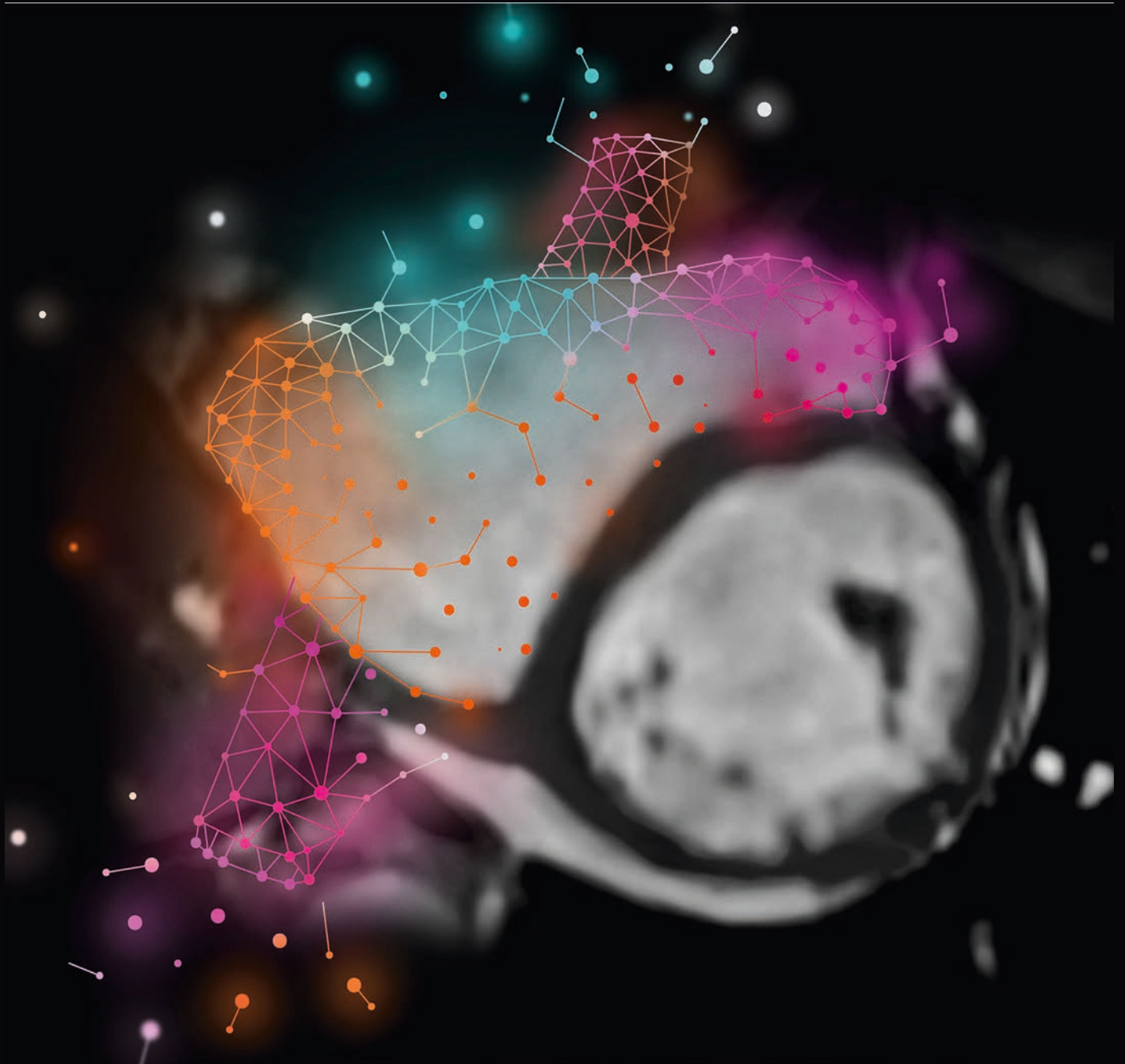
Professor Juerg Schwitter
Médecin Chef Cardiologie
Directeur du Centre de la RM
Cardiaque du CHUV
Centre Hospitalier
Universitaire Vaudois – CHUV
Rue du Bugnon 46
1011 Lausanne
Switzerland
Phone: +41 21 314 0012
jurg.schwitter@chuv.ch
www.cardiologie.chuv.ch

This reprinted article was based on an early works-in-progress CV_sparse prototype. In Compressed Sensing Cardiac Cine¹ the limitations such as fold-over artifacts as shown in Figure 6A have been remedied, and image reconstruction is faster and provides improved image quality.

¹ 510(k) pending. Compressed Sensing Cardiac Cine is not commercially available. Future availability cannot be guaranteed.

Compressed Sensing Cardiac Cine¹

Beyond speed. Beyond breath-holds.



Acquire free-breathing, high-resolution Cardiac Cine images.
Capture the whole cardiac cycle for precise quantification.
Expand patient population eligible for cardiac MRI.

¹ 510(k) pending. Compressed Sensing Cardiac Cine is not commercially available. Future availability cannot be guaranteed.

Compressed Sensing: Application to Time-of-Flight MR Angiography

Takayuki Yamamoto; Tomohisa Okada; Koji Fujimoto; Yasutaka Fushimi; Akira Yamamoto; Kaori Togashi

Department of Diagnostic Imaging and Nuclear Medicine, Kyoto University, Japan

Introduction

Time-of-Flight MR Angiography (TOF MRA) is a reliable method to visualize the cerebral vasculature and is widely used in clinical practice. It is a non-invasive technique, which is free from radiation exposure and adverse effects of contrast materials. The main concerns of high-resolution TOF MRA are its long scan time and decreased signal-to-noise ratio (SNR).

Compressed Sensing (CS) provides a novel approach to restore the original image quality from fewer k -space acquisitions by exploiting intrinsic sparsity in the imaged object combined with iterative reconstruction and its denoising capabilities. MRA is a good candidate for CS because of the high signal in the vessels which are sparse in space [1].

The combination of parallel acquisition (PAT) and CS can significantly reduce the examination time [3].

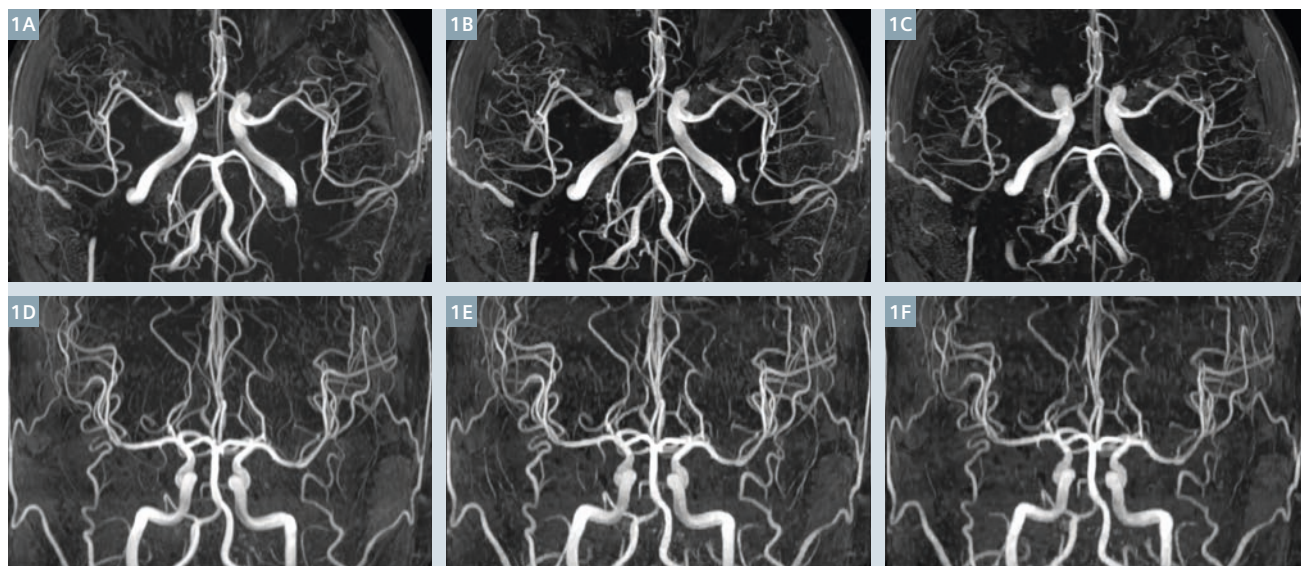
Scan time reduction is important not only for economic reasons but also to reduce the burden on the patient and to limit motion artifacts which can disrupt vascular depictions. In this case study, we will describe our early experiences with Compressed Sensing (CS) TOF¹ MRA in various clinical patients to visualize the cerebral arteries.

Compressed Sensing TOF technique

For data acquisition, a conventional 3D TOF gradient-echo sequence was combined with random sampling. For this purpose, the k -space of

each imaging slab was sub-sampled in the k_y - k_z phase-encoding direction with a variable density Poisson disk sampling pattern. In the pattern, the sampling density was gradually increased from periphery toward the center of k -space to optimize the acquisition of data in high image-energy central k -space regions and hence enhance the signal-to-noise ratio (SNR). The incoherence of the random sampling pattern would lead to artifacts that scatter across the whole image in a 'noise-like' manner after Fourier transform. A fully sampled region in the center of k -space was utilized to estimate the coil sensitivity maps.

¹ WIP, Compressed Sensing TOF is currently under development and is not for sale in the US and in other countries. Its future availability cannot be ensured.



1 Axial (1A-C) and coronal (1D-F) MIP images of a healthy subject (35-year-old, male) reconstructed from full-sampling data (1A, D), 3.4-fold net acceleration (1B, E), and 6.4-fold net acceleration (1C, F), respectively.

After data acquisition, the image can be recovered from the sub-sampled data by nonlinear, iterative reconstruction. In this reconstruction, the images were reconstructed by solving the following minimization problem [4-6]:

$$\min_x \|Ax - y\|_2^2 + \lambda \|\Phi(x)\|_1$$

where y is the acquired k -space data and x the estimated image. The system matrix, A , describes the data acquisition process, which is required for the comparison of the image and acquired data. The transform sparsity term enforces a sparse representation

of the image. For this purpose, the image is transformed a sparse representation by $\Phi(\cdot)$, for example, using the redundant Haar wavelet transform. The balance between data fidelity and sparsity is adjusted with the regularization parameter λ , which was empirically set to 0.0002. The iterative reconstruction process was terminated after 20 iterations.

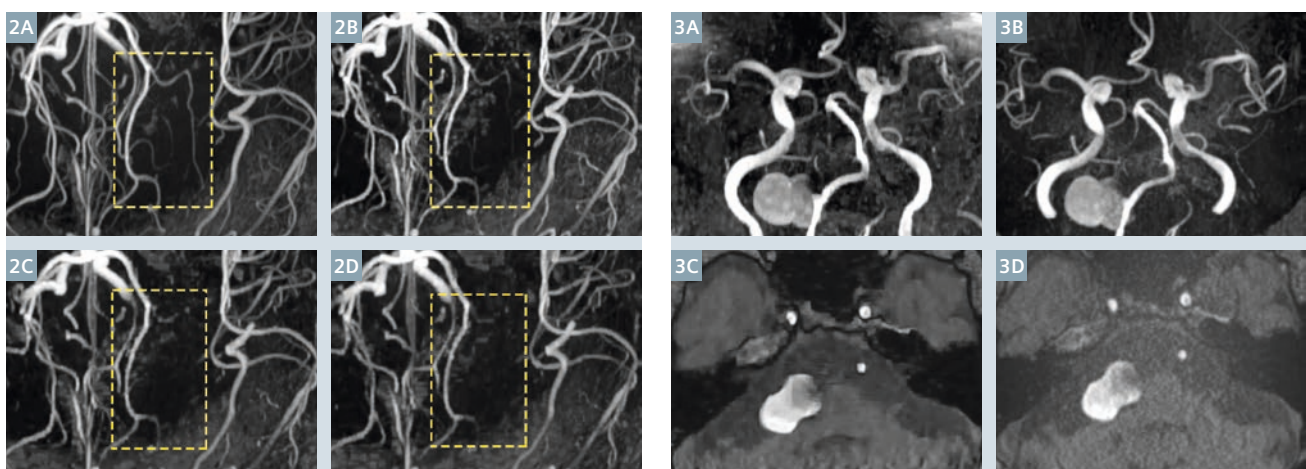
Imaging was performed at a clinical 3T MR scanner (MAGNETOM Skyra, Siemens Healthcare, Erlangen, Germany) with a 32-channel head coil. Parameters for the imaging protocol were TR 20 ms, TE 3.7 ms, flip angle 18° and bandwidth 189 Hz/Px. In total, 5 slabs were acquired with 20% slice oversampling with a matrix of $384 \times 326 \times 90$ and a voxel size

of $0.3 \times 0.3 \times 0.35$ mm (FOV 220×190 cm). The images of conventional TOF imaging with a PAT factor of 2 and 3 were compared to those acquired with CS TOF featuring acceleration rates from 3.4 up to 6.4.

Image reconstruction was done directly on the scanner with standard hardware.

Imaging examples of cerebral angiography with CS TOF

Figures 1 and 2 show images of healthy subjects. On maximum intensity projection (MIP) images, cerebral arteries are well visualized in CS TOF images with acceleration rates from 3.4 up to 6.4 (Fig. 2). Although the



2 Magnified view of MIP images for the same subject as in Figure 1. Net acceleration rates are (2A) full sampling, (2B) 3.4, (2C) 6.4, and (2D) 7.1. Most of the arterial branches are visualized well, but small branch with lower signal is a challenge for CS TOF (shown with rectangles in yellow dashed lines).

3 An aneurysm of the right vertebral artery in a 68-year-old male. (3A, C) CS TOF with net acceleration rate of 6.1, and (3B, D) conventional TOF MRA (using PAT factor of 3 in the phase encoding direction and partial Fourier of 7/8) with a net acceleration rate of 3.

depiction of distal branches becomes weaker at a higher acceleration rate (Fig. 3), the visualization of proximal branches was acceptable, which is important to diagnose the stenocclusive diseases or cerebral aneurysms. We have previously reported that the diagnostic quality of distal branches was maintained with a nominal acceleration factor of 6, which achieved a shorter acquisition time of less than half of the conventional PAT acceleration of 2 [1].

Figures 3 through 6 show cases in clinical practice. The result images of CS TOF and conventional TOF are displayed side by side to facilitate comparison of vascular shape. Conventional TOF used modified GRAPPA (acceleration factor of 3) and partial Fourier technique (7/8 for the phase and the slice direction). A net acceleration rate of 6.1 was used for CS TOF for all cases. The matrix size of conventional TOF was kept the same as CS TOF, but the number of slabs was 3, which was set to 5 for CS TOF. The acquisition time for conventional TOF was 3 min 11 sec.

Conclusion

CS TOF can drastically reduce the scan time while minimizing loss of image quality at high acceleration rates. In some cases, residual sub-sampling artifacts remain in the reconstructed images, however without influencing the image quality of the MIP angiogram remarkably. The first experiences indicate that a diagnostic image quality can be achieved in a clinical setting using highly accelerated CS TOF for the visualization of cerebral arteries. Our results warrants future larger clinical studies in a larger cohort to find the optimal balance between acquisition speed and high resolution.

Acknowledgements

The kind support of Aurelien F. Stalder, Yutaka Natsuaki, and Michaela Schmidt, employees in research and development functions of Siemens Healthineers, is greatly appreciated.

Case 1

68-year-old male was followed up for a large aneurysm of the right vertebral artery for several years (Fig. 4). The aneurysm gradually increased in size, and the patient was admitted to our hospital.

The size and the gourd-like shape of the aneurysm are well depicted in CS TOF. There is almost no difference in the MIP image between CS TOF and conventional TOF, although CS TOF is twice as fast.



4 Two aneurysms of the right internal carotid artery (arrows). (4A) CS TOF with a net acceleration rate of 6.1 and (4B) conventional TOF with a net acceleration rate of 3.

Case 2

78-year-old female was admitted to our hospital because of left hemiplegia. Two aneurysms in the right internal carotid artery (Fig. 5) are

incidentally found. Both aneurysms are well visualized in spite of their small size.

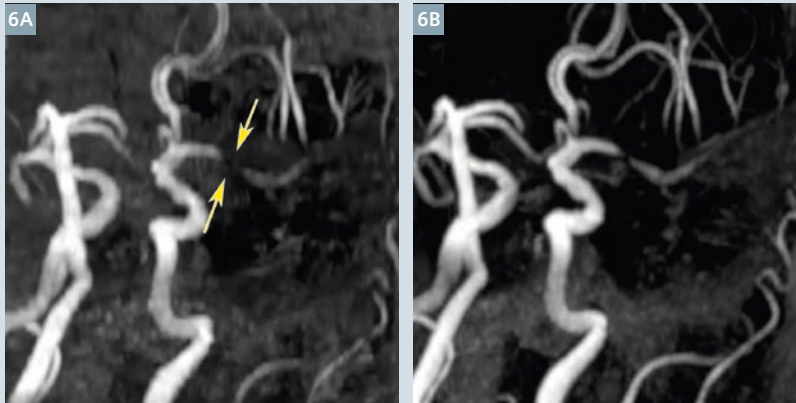


5 Stenosis of the left internal carotid artery (circle). (5A) CS TOF with a net acceleration rate of 6.1 and (5B) conventional TOF with a net acceleration rate of 3.

Case 3

74-year-old male with diabetes mellitus. The routine examination for diabetes revealed a severe stenosis of the left internal carotid artery (Fig. 6). The lesion is similarly depicted both in CS TOF and conventional TOF. Arterial

irregularity is additionally seen at the proximal portion of right internal carotid artery only in CS TOF, which gives the impression of stronger stenotic change. An influence of motion is possibly suspected.



6 Stenosis of the left middle cerebral artery (arrows). **(6A)** CS TOF with a net acceleration rate of 6.1 and **(6B)** conventional TOF with a net acceleration rate of 3.

References

- 1 Yamamoto T, Fujimoto K, Okada T, Fushimi Y, Stalder AF, Natsuaki Y, et al. Time-of-Flight Magnetic Resonance Angiography With Sparse Undersampling and Iterative Reconstruction. *Invest Radiol*. 2015 Nov [epub ahead of print].
- 2 Fushimi Y, Fujimoto K, Okada T, Yamamoto A, Tanaka T, Kikuchi T, et al. Compressed Sensing 3-Dimensional Time-of-Flight Magnetic Resonance Angiography for Cerebral Aneurysms. *Invest Radiol*. 2016 Apr;51(4):228–35.
- 3 Liang D, Liu B, Wang J, Ying L. Accelerating SENSE using compressed sensing. *Magn Reson Med*. 2009 Dec;62(6):1574–84.
- 4 Beck A, Teboulle M. A Fast Iterative Shrinkage-Thresholding Algorithm for Linear Inverse Problems. *SIAM J Imaging Sci*. 2009 Jan;2(1):183–202.
- 5 Liu J, Rapin J, Chang T-C, Lefebvre A, Zenge M, Mueller E, et al. Dynamic cardiac MRI reconstruction with weighted redundant Haar wavelets. *Proceedings of the 20th Annual Meeting of the ISMRM, Melbourne, Australia*; 2012. p. 4249.
- 6 Stalder AF, Schmidt M, Quick HH, Schlamann M, Maderwald S, Schmitt P, et al. Highly undersampled contrast-enhanced MRA with iterative reconstruction: Integration in a clinical setting. *Magn Reson Med*. 2014 Dec 17.



Takayuki Yamamoto



Tomohisa Okada



Koji Fujimoto



Yasutaka Fushimi



Akira Yamamoto



Kaori Togashi

Contact

Tomohisa Okada, M.D., Ph.D.
Human Brain Research Center
Graduate School of Medicine
Kyoto University
54 Shogoin-Kawaharacho,
Sakyo-ku
Kyoto 606-8507
Japan
tomokada@kuhp.kyoto-u.ac.jp

Improving Dynamic MR Angiography: Iterative TWIST

Bernd J. Wintersperger^{1,2}; Luigia D'Errico^{1,2}; Christoph Forman³; Jens Wetzl⁴; Michaela Schmidt³; Aurelien F. Stalder³

¹ Department of Medical Imaging, Peter Munk Cardiac Centre, University Health Network, Toronto, Ontario, Canada

² Department of Medical Imaging, University of Toronto, Toronto, Ontario, Canada

³ Siemens Healthineers, Erlangen, Germany

⁴ Pattern Recognition Lab, Department of Computer Science, FAU Erlangen-Nürnberg, Erlangen, Germany

Introduction

Nowadays, many vascular territories are explored non-invasively for the purpose of diagnosis, therapy planning and surveillance of vascular disease. Invasive catheter angiography is almost exclusively being used during therapy and intervention. However, the benefits of invasive approaches include the ability to visualize dynamics of applied dye and may therefore provide additional information on the potential hemodynamic relevance of vascular disease or stenosis.

In recent years, magnetic resonance angiography (MRA) has become a dominant tool of non-invasive high-resolution delineation of body and peripheral vasculature. With

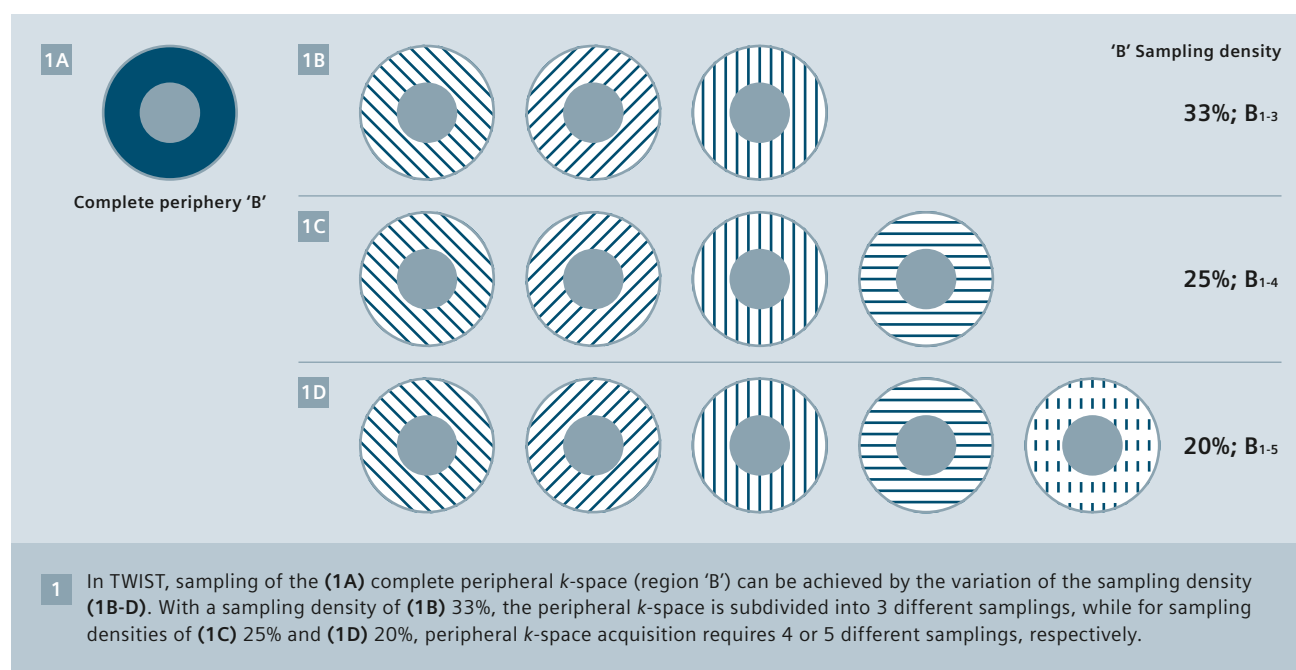
the ever increasing importance of continuous surveillance in genetic aortic disease (e.g. Marfan's, Ehlers-Danlos, Loeys-Dietz, etc.), the role of MRA developed beyond atherosclerotic disease and focuses more often on a younger population.

Most commonly, outside the brain, contrast-enhanced MRA (CE-MRA) techniques are being employed sampling a high-resolution data set after a contrast agent timing bolus.

In order to overcome the limitations of purely static MRA, various techniques such as time-resolved imaging of contrast kinetics (TRICKS) and time-resolved angiography with stochastic trajectories (TWIST) are being employed [1, 2]. The predominant underlying principle of these

approaches relates to keyhole imaging with more frequent sampling of central k -space data vs. peripheral k -space data. In addition to commonly applied acceleration techniques (e.g. partial Fourier, parallel imaging, etc.), dynamic CE-MRA also relies on view-sharing for peripheral k -space coverage in order to improve temporal resolution (Figs. 1-2).

Dynamic CE-MRA using TWIST has proven beneficial and successful in the diagnosis of disease across vessel territories from head to toe [3-5]. Besides a direct vascular focus, the relatively high temporal resolution 3D coverage, combined with prominent T1-weighting and background tissue suppression, has been applied to tissue perfusion studies.



Dynamic contrast-enhanced MRA with iterative TWIST

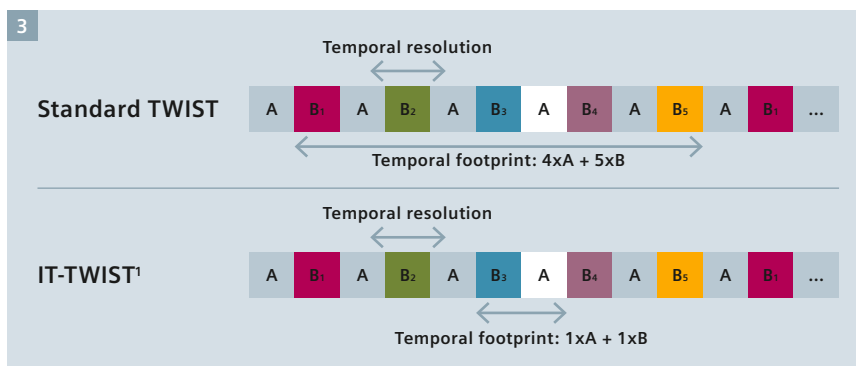
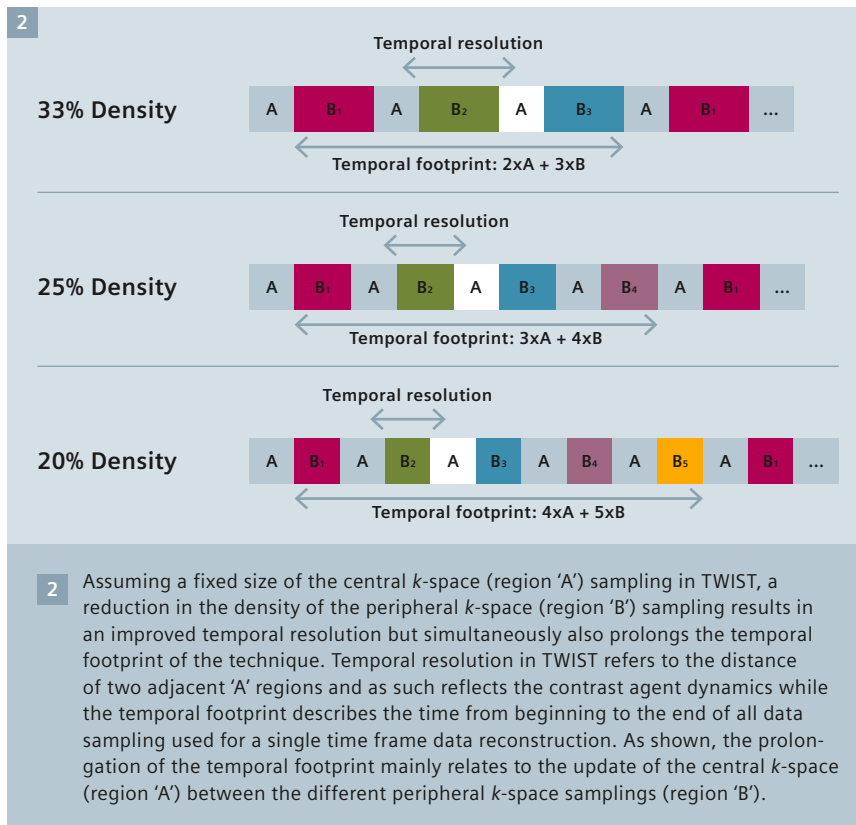
With repeated updates of the central k -space data, the dynamic pass of a Gadolinium-based contrast agent (GBCA) can be followed through the vasculature of interest without the need for a timed bolus. However, while the sharing of peripheral k -space data across multiple time points

provides an improved update rate of images (apparent 'temporal resolution'), it also results in a prolongation of the 'temporal footprint' of TWIST (Fig. 2). Especially in areas of possible motion and fast blood circulation (e.g. chest, pulmonary vasculature), this may result in inconsistencies, temporal blurring and subsequent image degradation, specifically of small vasculature.

Recent interest in Compressed Sensing approaches successfully demonstrated benefits of these techniques in various MR applications including CE-MRA [6] and dynamic CE-MRA [7, 8]. The potential benefits of such iterative reconstruction approaches have recently been explored in clinical scenarios [8, 9].

Iterative TWIST (IT-TWIST)¹ uses the sampling pattern of a regular TWIST acquisition, but does not rely on view sharing during image reconstruction. Instead, the implemented iterative reconstruction algorithm relies on the intrinsic incoherent sampling pattern of the peripheral k -space data and uses a Compressed Sensing approach with spatial and temporal regularization to suppress artifacts arising from k -space undersampling.

More in detail, the TWIST acquisition consists of interleaved acquisitions of central k -space (region 'A') and different incoherent sub-samplings of peripheral k -space (region 'B'). Regular TWIST reconstruction then combines multiple 'B' regions (view sharing) with one 'A' region to form a coherently subsampled k -space suitable for parallel imaging reconstruction (see Figures 1, 2). In contrast, the iterative TWIST reconstruction uses a single region 'A' and region 'B' pair per time frame, thus decreasing the 'temporal footprint' to be identical to the 'image update rate' (apparent 'temporal resolution') (Fig. 3). To recover the individual time frames despite the higher undersampling, a non-linear iterative SENSE reconstruction is being used. The iterative reconstruction uses spatio-temporal regularization based on Haar wavelets [8, 10]. This reconstruction process results in a considerable computational burden and therefore is carried out on the Graphics Processing Unit (GPU) of the standard image reconstruction system. Depending on detailed acquisition parameters and time frames current reconstruction times are about 20 minutes.



3 Iterative TWIST (IT-TWIST¹) allows a substantial shortening of the temporal footprint in data reconstruction. While in standard TWIST a complete coverage of region 'B' is required (sampling density of 20% shown), IT-TWIST reconstruction reduces the temporal footprint to a single 'B' region in addition to the respective central k -space (region 'A'). This is achieved by the incoherent sampling pattern of region 'B' in TWIST and application of a Compressed Sensing reconstruction approach with spatial and temporal regularization.

¹ WIP. IT-TWIST is work in progress and is not commercially available. Future availability cannot be guaranteed.

In order to assess the impact of such improved 'temporal footprints' and increased signal-to-noise ratio (SNR) of the CS reconstruction algorithm due to de-noising, we aimed at patients referred for the assessment of the thoracic aorta and the great thoracic vessels. The applied imaging protocol focused on high temporal and spatial resolution [8] (Table 1). All imaging was performed on a 64-channel MAGNETOM Skyra^{fit} system and contrast enhancement for TWIST was provided by automated injection of Gadobutrol (Gadavist, Bayer Pharma, Berlin, Germany) [8]. All acquired raw data sets were reconstructed twice: using the (1) standard product reconstruction as well as the above described (2) IT-TWIST reconstruction.

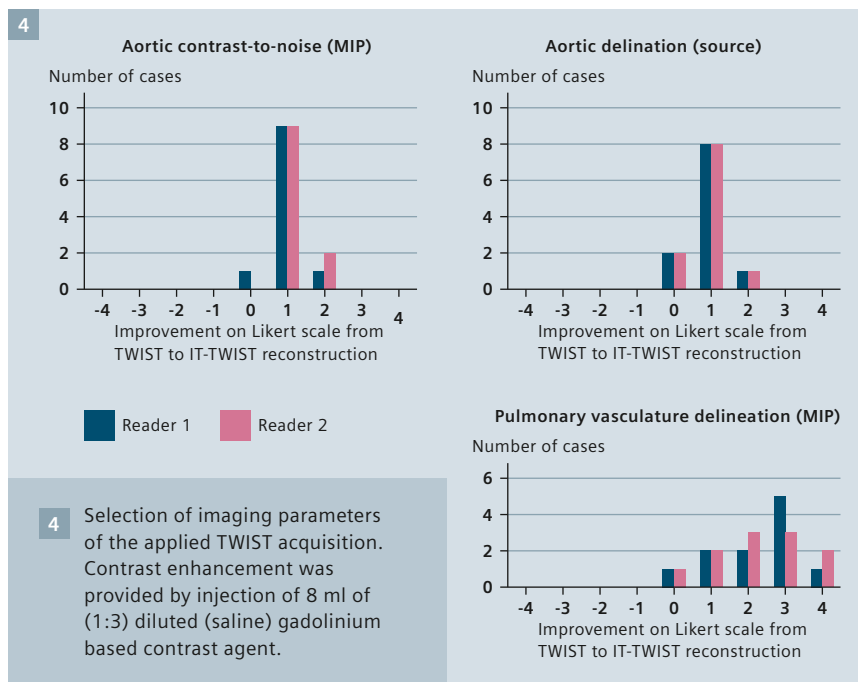
In all patients, IT-TWIST was equal or superior to TWIST reconstruction; in fact, in the vast majority of cases, image quality as assessed by two readers with respect to aortic contrast-to-noise (CNR), aortic delineation and medium-to-small vessel (pulmonary vasculature) delineation improved by at least 1 point on the Likert scale (0 = non-diagnostic; 1 = poor; 2 = fair; 3 = good; 4 = excellent) [9] (Figs. 4-6). The most prominent improvement with IT-TWIST was seen in the area of medium-to-small vessels of the pulmonary vasculature, which also demonstrated an improvement in the signal response amplitude as compared to TWIST [8] (Figs. 4-6).

Conclusion

Initial experiences of IT-TWIST in clinical thoracic imaging with dynamic CE-MRA demonstrate extremely promising results, especially when focusing on the medium-to-small sized pulmonary vasculature. The specific improvement within the pulmonary vasculature most likely relates to the substantially shortened 'temporal footprint' with IT-TWIST. This approach allows to further push temporal resolution by lowering sampling density of the peripheral *k*-space. As the principles of Compressed Sensing maintain a reasonable SNR and CNR level, a further push of spatial resolution by using higher parallel imaging

FOV	333 x 380 x 88 mm ³
Voxel size (measured)	1.2 x 1.0 x 1.2 mm ³
Voxel size (interpolated)	1.0 x 1.0 x 1.0 mm ³
iPAT	4 x 2
TR / TE / Flip angle	2.89 ms / 1.05 ms / 17°
'A' region (sampling density)	15%
'B' region (sampling density)	20%
Temporal resolution (apparent)	2.4 s

Table 1: Imaging protocol

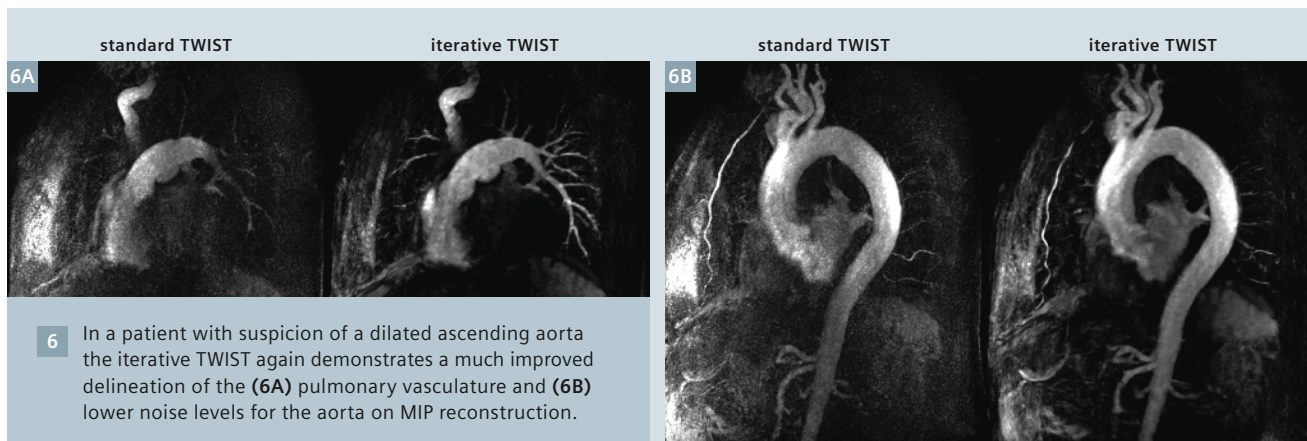
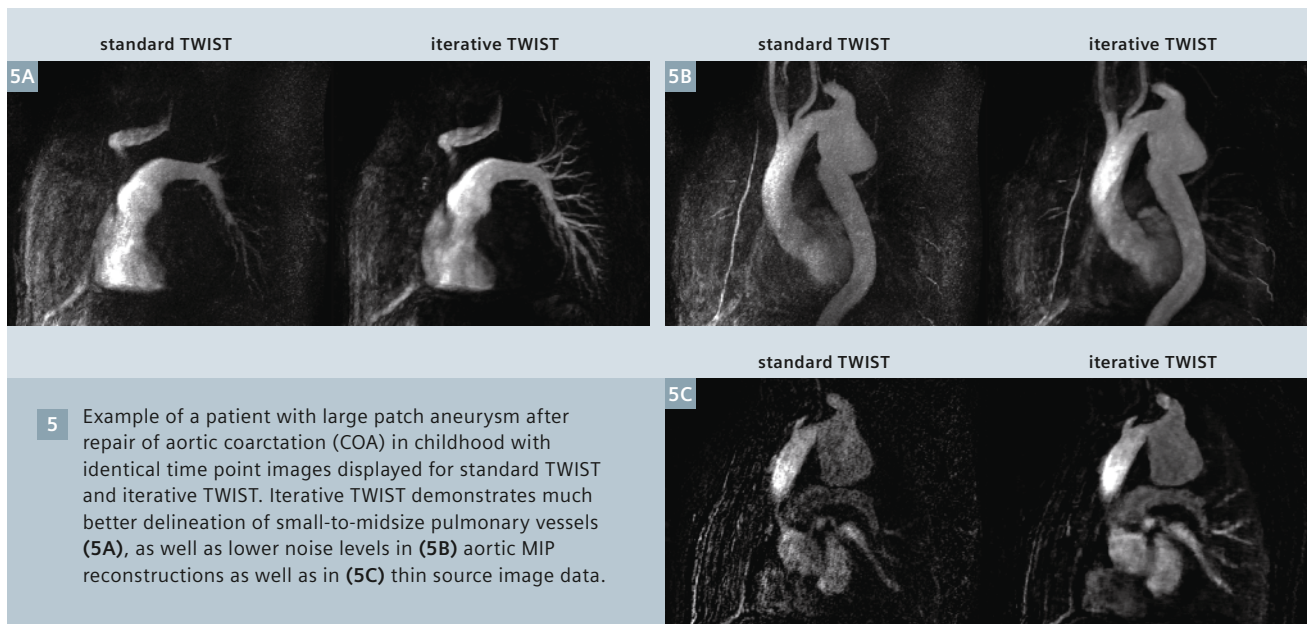


accelerations is possible. While experience in other vascular territories is currently limited at our site, further exploration will determine the possible benefit across the body vasculature and also the impact of IT-TWIST on detailed parameters of vessel boundaries and vessel size. Furthermore, it will provide insights into the possibly required adaptation of specific factors of the reconstruction based on territory, image quality need and acceleration.

Nevertheless, IT-TWIST represents an important step ahead towards high spatial/high temporal resolution dynamic CE-MRA of the future. This will provide a straightforward inject-and-shoot CE-MRA protocol without the need for any bolus timing and quite possibly also result in changes of the required contrast agent volumes.

References

- 1 Korosec FR, Frayne R, Grist TM, Mistretta CA (1996) Time-resolved contrast-enhanced 3D MR angiography. *Magn Reson Med* 36:345-351.
- 2 Song T, Laine AF, Chen Q, Rusinek H, Bokacheva L, Lim RP, Laub G, Kroeker R, Lee VS (2009) Optimal *k*-space sampling for dynamic contrast-enhanced MRI with an application to MR renography. *Magn Reson Med* 61:1242-1248.
- 3 Jeong HJ, Vakil P, Sheehan JJ, Shah SJ, Cuttica M, Carr JC, Carroll TJ, Davarpanah A (2011) Time-resolved magnetic resonance angiography: evaluation of intrapulmonary circulation parameters in pulmonary arterial hypertension. *J Magn Reson Imaging* 33:225-231.
- 4 Kinner S, Quick HH, Maderwald S, Hunold P, Barkhausen J, Vogt FM (2013) Triple-TWIST MRA: high spatial and temporal resolution MR angiography of the entire peripheral vascular system using a time-resolved 4D MRA technique. *Eur Radiol* 23:298-306.



- 5 Lohan DG, Tomasian A, Saleh RS, Singhal A, Krishnam MS, Finn JP (2009) Ultra-low-dose, time-resolved contrast-enhanced magnetic resonance angiography of the carotid arteries at 3.0 tesla. *Invest Radiol* 44:207-217.
- 6 Stalder AF, Schmidt M, Quick HH, Schlamann M, Maderwald S, Schmitt P, Wang Q, Nadar MS, Zenge MO (2015) Highly undersampled contrast-enhanced MRA with iterative reconstruction: Integration in a clinical setting. *Magn Reson Med* 74:1652-1660.
- 7 Rapacchi S, Natsuaki Y, Plotnik A, Gabriel S, Laub G, Finn JP, Hu P (2015) Reducing view-sharing using compressed sensing in time-resolved contrast-enhanced magnetic resonance angiography. *Magn Reson Med* 74:474-481.
- 8 Wetzl J, Forman C, Wintersperger BJ, D'Errico L, Schmidt M, Mailhe B, Maier A, Stalder AF (2016) High-resolution dynamic CE-MRA of the thorax enabled by iterative TWIST reconstruction. *Magn Reson Med*. 10.1002/mrm.26146.
- 9 D'Errico L, Schmidt M, Wetzl J, Forman C, Stalder AF, Wintersperger BJ (2016) Improved Dynamic Contrast-Enhanced Magnetic Resonance Angiography (CE-MRA) using Iterative Data Reconstruction. *Journal of Cardiovascular Magnetic Resonance* 18:O112.
- 10 Forman C, Piccini D, Grimm R, Hutter J, Hornegger J, Zenge MO (2015) Reduction of respiratory motion artifacts for free-breathing whole-heart coronary MRA by weighted iterative reconstruction. *Magn Reson Med* 73:1885-1895.



Contact

Bernd J. Wintersperger, MD EBCR FAHA
Department of Medical Imaging
Toronto General Hospital, 1 PMB-273
585 University Avenue
Toronto, Ontario, M5G 2N2, Canada
+1 416-340-4800 ex. 8593
Bernd.Wintersperger@uhn.ca

GRASP: Tackling the Challenges of Abdominopelvic DCE-MRI

Kai Tobias Block¹; Li Feng¹; Robert Grimm²; Hersh Chandarana¹; Ricardo Otazo¹; Christian Geppert²; Daniel K. Sodickson¹

¹ Department of Radiology, NYU Langone Medical Center, New York, NY, USA

² Siemens Healthcare, Erlangen, Germany

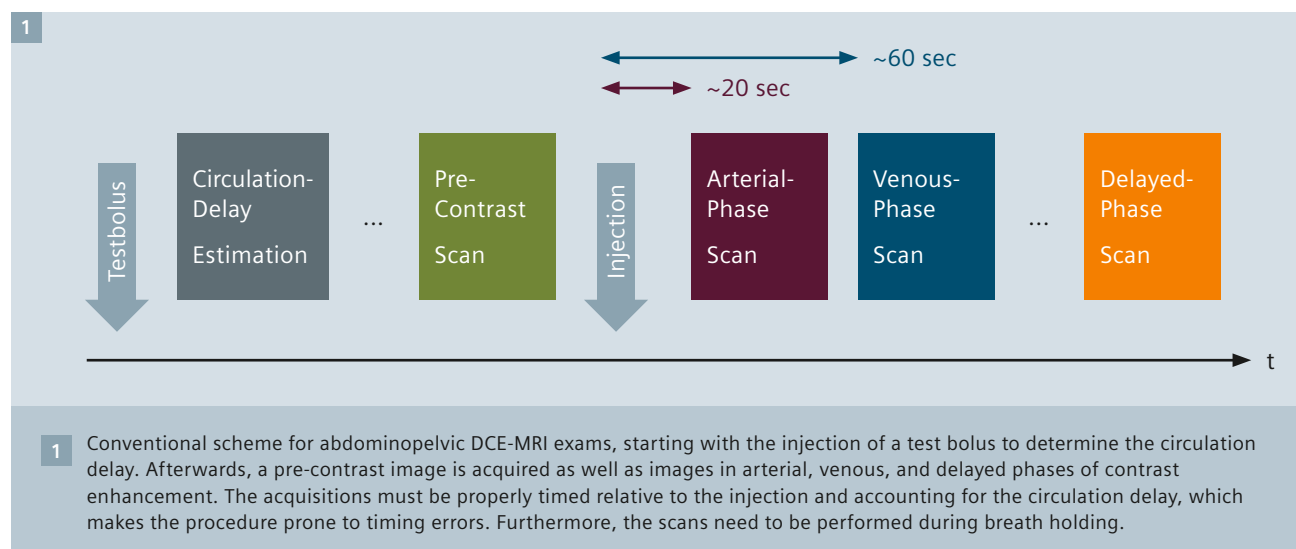
Introduction

Dynamic contrast-enhanced (DCE) T1-weighted acquisition after injection of a gadolinium-based contrast agent is an integral part of most diagnostic abdominopelvic MRI examinations and essential for identifying and properly characterizing lesions and tumors, such as the hepatocellular carcinoma (HCC) or renal cancer [1]. Because tumors show a specific temporal contrast-enhancement pattern, it is necessary to obtain images of the whole region-of-interest at multiple short time points following the injection. While technically infeasible years ago, parallel-imaging acceleration techniques such as GRAPPA [2] have made it possible to achieve the required acquisition speed using standard clinical MRI systems, so that these scans can nowadays be performed at almost all imaging centers.

However, in routine practice abdominopelvic DCE-MRI exams remain challenging and the failure rates are undesirably high.

One main challenge is that the data has to be collected precisely at defined time points relative to the arrival time of the contrast agent in the aorta (see Fig. 1). To this end, usually a small test bolus is injected prior to the actual diagnostic scan and monitored using a bolus-tracking sequence to determine the patient-specific circulation delay [3]. Once estimated, the delay is then incorporated into the timing calculation of the dynamic scans, which are scheduled relative to the injection time of the contrast dose. This procedure is, of course, prone to inaccuracies and mistakes – with the potential risk of missing the important arterial phase (AP) of contrast enhancement. As additional complication, the dynamic acquisitions have to be performed

during a strict breath hold of the patient and, thus, need to be properly synchronized with breath-hold commands. While the latter can be automated using computer-controlled voice instructions [3], it cannot be guaranteed that the patient is actually following these breath-hold instructions. Continued respiration occurs due to various reasons, including inability to hold breath for the scan duration (usually ~15 sec per acquisition), hearing or language problems, and uncertainty when exactly to stop breathing after hearing the command. Especially elderly or severely sick patients often struggle to properly suspend respiration, resulting in compromised or even fully non-diagnostic image quality. A particular problem here is that once the injection has been done, the acquisitions cannot be repeated before the contrast agent has been extracted from the body, which takes several hours and requires



rescheduling of the examination on a different day. Strongly compromised image quality is also obtained when examining sedated or anesthetized patients, where suspending the respiration is not possible at all.

DCE-MRI with continuous radial acquisition

The requirement to perform abdominal scans during breath-holding results from the high motion sensitivity of conventional MRI techniques, as motion translates into appearance of numerous overlapping object copies known as ghosting artifacts. This problem can be ameliorated by using non-Cartesian acquisition techniques such as radial *k*-space sampling, which inherently prevent the appearance of motion-induced ghosting artifacts. Radial scanning techniques, such as the Radial VIBE or StarVIBE sequence [4], have recently become available for routine imaging, and it has been demonstrated that these sequences can be used to image the abdomen during free-breathing [5]. However, the higher motion robustness of radial *k*-space trajectories comes at the price

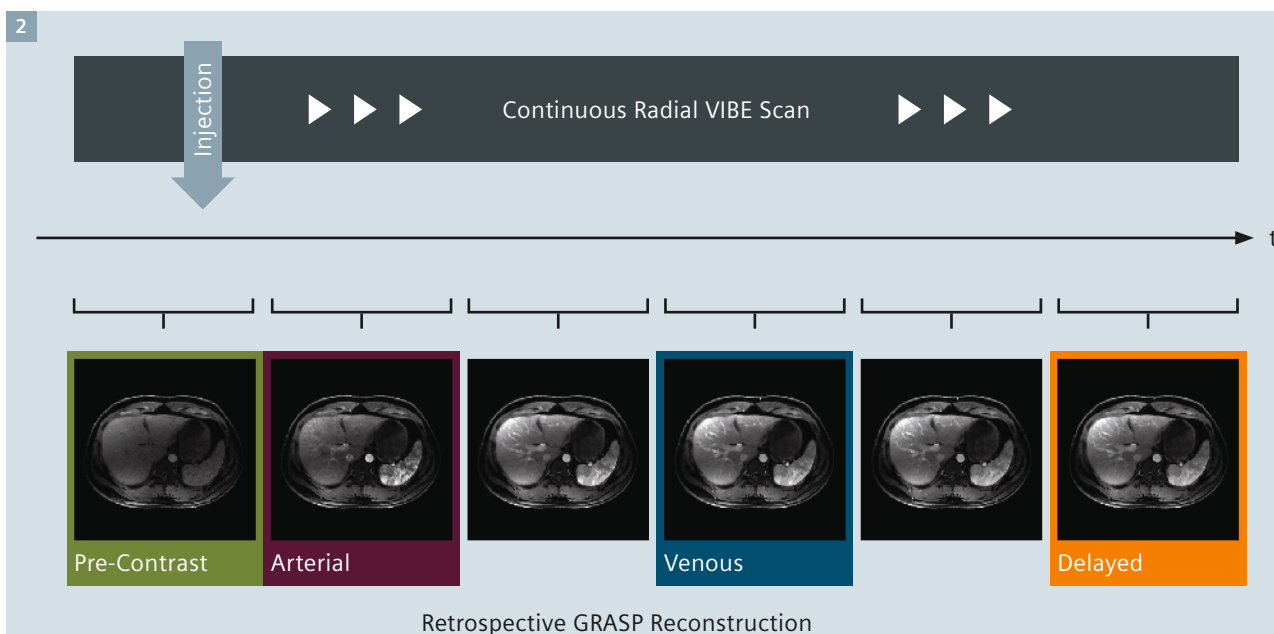
of lower scan efficiency. With typical scan durations of around 60 sec per image volume, sequences such as Radial VIBE are by itself too slow for dynamic abdominopelvic imaging as it would be impossible to separate the arterial and venous phases of enhancement.

To overcome this problem, our group has recently developed a technique called GRASP¹ that enables using the Radial VIBE sequence for DCE-MRI applications and that resolves many of the aforementioned challenges [6]. The key idea of GRASP is that, instead of performing several individual acquisitions for the required time points, data is acquired continuously throughout the whole exam while the contrast agent is injected (see Fig. 2). Image sets for the needed time points are then calculated from the continuously acquired data using an iterative reconstruction procedure (as described in the next section).

This concept leads to a significant simplification of the overall clinical workflow. Because data is acquired all the time during the examination, it is not necessary anymore to determine the circulation delay using a test bolus. Also, the possibility of missing one of the important enhancement phases as a result of a timing or synchronization error is eliminated. Furthermore, because based on radial *k*-space acquisition, GRASP examinations can be performed during continued breathing [7], which removes the need for breath-hold commands, improves patient comfort, and makes the technique well-suited for patients where holding breath is impossible, such as pediatric² patients. Hence, with GRASP, the formerly complex and stressful abdominopelvic DCE-MRI exams now become a simple one-click procedure.

¹ WIP, the product is currently under development and is not for sale in the US and in other countries. Its future availability cannot be ensured.

² MR scanning has not been established as safe for imaging fetuses and infants under two years of age. The responsible physician must evaluate the benefit of the MRI examination in comparison to other imaging procedures.



2 GRASP scheme for DCE-MRI, which uses a single continuous acquisition while the contrast agent is injected. Because radial sampling of *k*-space is used, the data can be acquired during free-breathing. Images are calculated from the continuous data using an iterative reconstruction that allows selecting the desired time points and temporal resolution retrospectively. This eliminates the possibility of timing errors and leads to significant simplification of the workflow.

Technical background

On a technical level, GRASP combines several concepts for MRI scan acceleration that have been described previously as individual techniques. The data acquisition is based on the radial golden-angle ordering scheme, which was originally proposed by Winkelmann et al. [8]. When acquiring radial data with constant angular increment of 111.25 degrees (referred to as 'golden angle' because it corresponds to 180 degrees multiplied by the golden ratio), successively sampled radial spokes always add complementary *k*-space information to the previously acquired data, and any number of grouped spokes cover *k*-space approximately uniformly. This means that if data is acquired continuously over some time, any number of successively acquired spokes can be combined into an individual image (e.g., 144 spokes for low temporal resolution, or 21 spokes for high temporal resolution). Furthermore, the reconstruction window can be placed at any time point of the scan. In other words, it is possible to retrospectively decide which temporal resolution and which time points should be reconstructed.

When grouping only few spokes into each image to achieve high temporal resolution, as needed in DCE-MRI for separating the phases of enhancement, the data available for each time point is highly incomplete or, according to MR terminology, undersampled. For radial sequences, this means that the images are affected by severe 'streak' artifacts, which render the images diagnostically unusable. However, GRASP applies two known tricks to suppress this effect and to recover artifact-free images from the undersampled data: Compressed sensing [9] and parallel imaging [10]. The use of compressed sensing is motivated from the fact that the streak artifacts lead to strongly flickering patterns if viewed along time, whereas the true contrast enhancement occurs in a 'smooth' non-flickering fashion. In other words, flickering pixel intensities can be considered as artificial effects. Therefore, artifact-free

images can be obtained by employing an iterative reconstruction procedure that, during each calculation step, matches the solution with the available undersampled data and, in addition, suppresses flickering pixels. Mathematically, this is achieved by calculating the total variation (TV) of each pixel along time and using this value as penalty measure during the iterations (because the true solution should have low total variation). By running the iterative procedure for a certain number of iterations, the streak artifacts disappear and the underlying true solution is recovered – even for severely undersampled data. As second mechanism, parallel imaging is integrated into the iterative scheme by using a CG-SENSE-type formalism [11], which contributes to the suppression of streaking artifacts by exploiting local coil sensitivities. Due to the synergistic combination of these two MR acceleration techniques, GRASP is able to compensate for the lower scan efficiency of radial sampling and achieves even higher temporal resolution than possible with most conventional DCE-MRI techniques. The key advantage, however, consists in the aforementioned workflow simplification.

Clinical integration and evaluation

The downside of using such an iterative reconstruction approach is that the image calculation involves a very computationally demanding numerical process (because the solution has to be mapped between image space and radial *k*-space over and over again). This property is not specific to GRASP and applies to other compressed-sensing techniques likewise. However, a difference is that the amount of data acquired during continuous GRASP acquisitions is enormous (up to 10 GB per scan). Processing such a vast amount of data with the described algorithm is not feasible using the computer components of current clinical MRI scanners, as the MRI systems would be blocked from clinical scanning for an unacceptable long time. Hence, for validating the feasibility of the GRASP technique in actual clinical practice,

it was necessary for us to derive a workflow-friendly solution that completely circumvents the normal reconstruction pipeline. Therefore, we developed an offline-processing framework [12] that automatically transfers the acquired GRASP data from our various clinical MRI scanners to a central reconstruction server. Incoming reconstruction tasks are queued according to urgency (clinical vs. research scan) and processed with a parallelized and performance-optimized C++ implementation of the GRASP algorithm. Upon completion, the reconstructed images are sent into the clinical PACS without any user interaction. Our radiologists can then read the GRASP exams side-by-side with other scans that were reconstructed directly on the MRI scanner. Using our current reconstruction server with 64 CPU cores, GRASP images are available in the PACS within 5 to 45 minutes after the exam (depending on the exact scan/reconstruction protocol). With this seamless integration of the GRASP prototype into our routine clinical workflow, a stable solution is now in place to evaluate the technique in a large number of patients and across our different MRI systems. Over the last two years, already several thousand GRASP reconstructions have been performed at our institution, and the setup has recently also been disseminated to multiple collaboration sites for an independent evaluation.

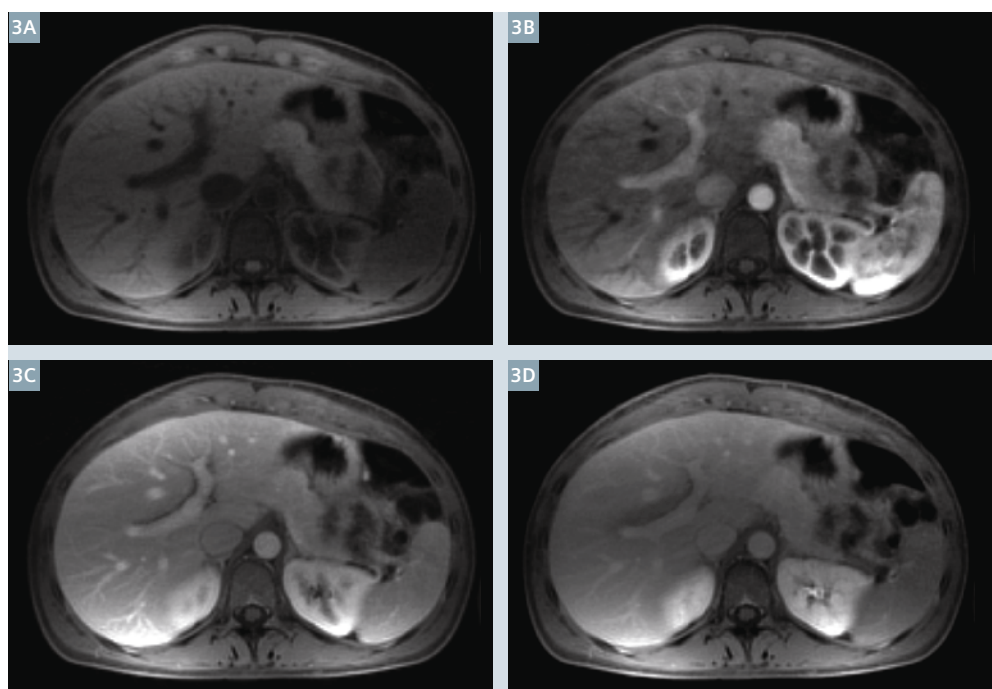
Initial applications

As the development of GRASP was aimed at improving abdominal DCE-MRI, liver and kidney scans are logically among the main applications. Figure 3 shows exemplary images from a free-breathing GRASP liver exam of an adult patient, which are free from the typical MRI ghosting artifacts for continued respiration. In this reconstruction, 55 spokes were combined into each image, which yields a temporal resolution of 8.8 sec per image volume and fulfills the timing requirements for diagnostic abdominal DCE-MRI. However, a very powerful feature of GRASP is that the same dataset can be reconstructed with different temporal resolution as well.

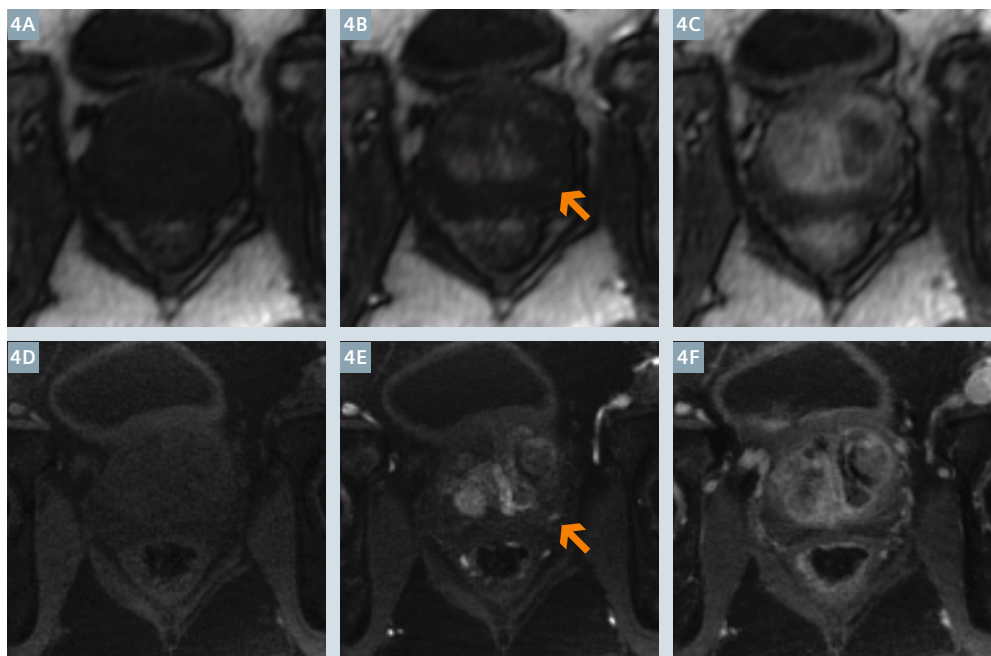
When grouping only 13 spokes into each image, the resulting temporal resolution is 2.1 sec and thus, fast enough for quantitative tissue-perfusion analysis. Researchers in our group are currently exploring this possibility for assessment of the liver function via dual-input dual-compartment modeling [13] and for assessment of the kidney function via estimation of the glomerular filtration rate (GFR). The key advantage here is that the perfusion information is obtained simultaneously without need for additional contrast injection or scan time. Thus, in the future, the GRASP concept might not only help to make abdominal examinations more robust but also provide new diagnostic measures.

Due to the high scan efficiency and simple workflow, GRASP is also very interesting for dynamic imaging of the prostate [14], which has become the GRASP application with the largest clinical scan volume at our institution. In prostate DCE-MRI, which is also with conventional techniques acquired during free breathing due to the required long readout (to properly capture the contrast washout), the main benefit of using GRASP consists in the higher achievable resolution (both spatially and temporally), which translates into an improved detectability and characterization of small tumors. Figure 4 shows images from our current GRASP protocol with $1.1 \times 1.1 \times 3.0$ mm spatial and 2.2 sec temporal resolution, which represents a significant improvement in comparison to our former protocol and allows more precise assessment of the uptake/washout characteristics of suspicious lesions. In this application, data is acquired over a total duration of 5:38 min while the contrast agent is injected 20 sec after the start of the scan to ensure that sufficient pre-contrast data is available. In addition to the higher resolution, also the motion robustness of GRASP contributes to the achieved improvement in image clarity, as conventional prostate scans are often affected by ghosting artifacts caused by motion of the rectum or adjacent bowel loops.

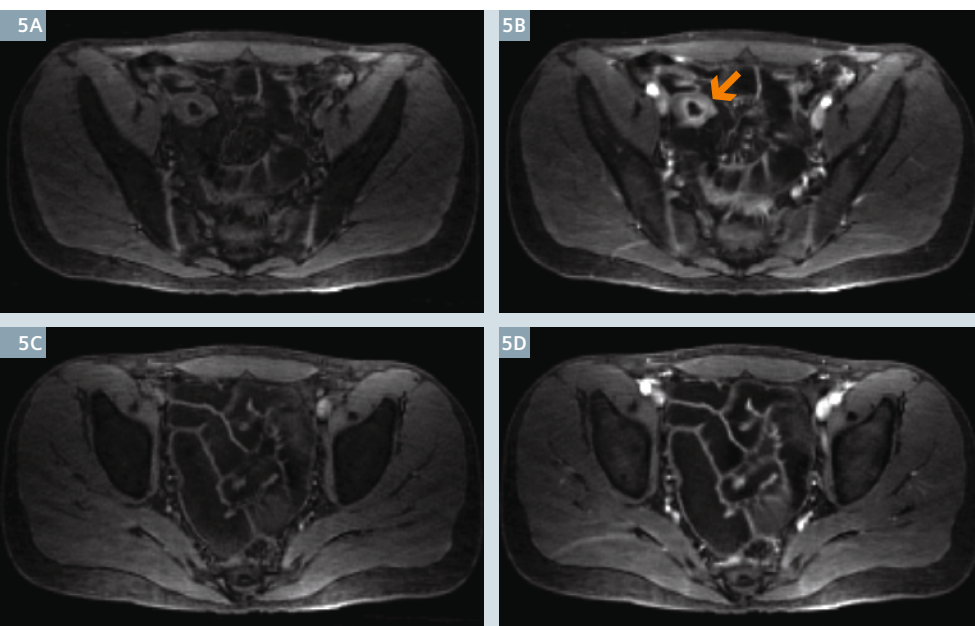
Because GRASP handles such motion effects in a relatively benign manner, our clinical researchers have started



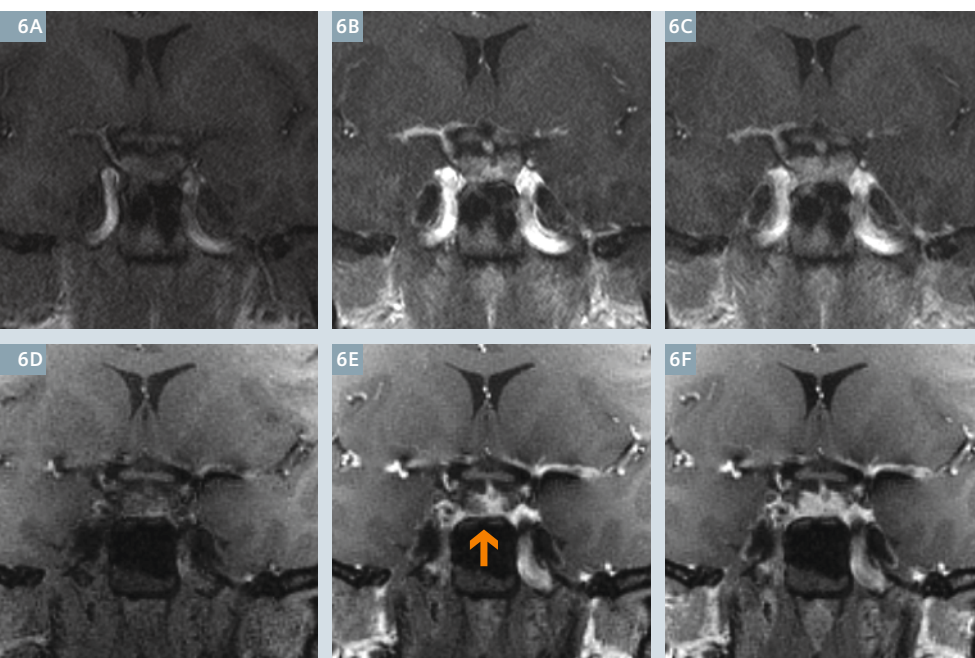
3 Free-breathing dynamic liver GRASP exam in an adult patient. Shown are images of the (3A) pre-contrast, (3B) arterial, (3C) venous, and (3D) delayed phase of enhancement. The reconstruction used 55 spokes per frame, corresponding to 8.8 sec per image (spatial resolution $1.5 \times 1.5 \times 3.0$ mm, acquired at 1.5 Tesla).



4 Dynamic prostate exam in a patient on active surveillance using (4A, B, C) conventional 3D FLASH with 5.5 sec temporal resolution and (4D, E, F) GRASP with 2.2 sec temporal resolution (both acquired at 3 Tesla). Images are shown from (4A, D) before the injection, (4B, E) the time of contrast arrival, and (4C, F) a late phase. Due to the higher spatial resolution (1.1 mm vs. 1.9 mm), a suspicious lesion in the peripheral zone with early enhancement and rapid washout (arrow) is more clearly visible on the GRASP scan. Note that the GRASP acquisition used fat suppression due to the off-resonance behavior of radial k-space sampling [4].



5 Bowel imaging using GRASP in a patient with Crohn's disease (acquired at 1.5 Tesla). Shown are time points (5A, C) before and (5B, D) shortly after the contrast injection. In the upper images (5A, B), a bowel section with increased wall thickness and mucosal hyperenhancement can be seen (arrow), which indicates active inflammation. For comparison, the lower row (5C, D) shows a different slice with normal-appearing bowel sections.



6 Dynamic imaging of the pituitary gland using (6A, B, C) a conventional 2D GRE sequence and (6D, E, F) GRASP (both acquired at 3 Tesla). Shown are images (6A, D) before the injection, (6B, E) shortly after contrast arrival, and (6C, F) at a later phase. A small area with delayed contrast uptake is visible in the inferior right gland (arrow), which likely reflects a microadenoma. Because of much thinner slices (1 mm vs. 3 mm) and higher overall image quality, such findings are easier to identify with GRASP.

using GRASP also for bowel imaging to investigate inflammatory bowel diseases such as Crohn's disease [15]. Inflamed bowel sections are characterized by increased wall thickness and reduced motility, as well as increased vascularity. Therefore, these bowel sections can be easily identified on GRASP scans, as shown in Figure 5. In addition, signal-enhancement curves can be generated from region-of-interests of the dynamic GRASP images and used to calculate quantitative perfusion measures that have been found to correlate with inflammation [15]. These parameters can potentially be used to non-invasively predict disease progression as well as response to treatments. Again, an advantage is that the perfusion images are obtained together with morphologic information from the same dataset through GRASP reconstruction with variable temporal resolution.

Finally, applications of GRASP are of course not confined to abdominopelvic imaging. GRASP can be used as robust imaging technique for any other dynamic T1-weighted examination as well, and a large portion of our recent GRASP scans are actually done in the head and neck region, including dynamic imaging of the orbits, the neck, and the pituitary gland. In the latter application, it is again the improvement in spatial resolution that makes GRASP attractive. When compared to our previously employed 2D GRE protocol (see Fig. 6), GRASP provides much higher spatial resolution along the slice direction and, thus, makes it easier to accurately localize tiny lesions such as microadenomas or small cysts. The possibility to incorporate also perfusion information into the diagnosis adds to its value [16].

Additional motion compensation

So, is GRASP now the ultimate solution for abdominopelvic DCE-MRI? Unfortunately, not quite yet. Our clinical evaluation showed that free-breathing abdominal GRASP exams work well in many patients with convincing results, but in a certain percentage of patients the image quality is still suboptimal. The problem here is that some patients perform deep respiration in

the moment when the contrast agent is injected, most likely because they are surprised by the sudden onset of the injection and the resulting sensation. Some patients even start to cough, so that the liver and adjacent organs rapidly move up and down by up to 10 cm during the initial circulations of the contrast agent. While GRASP handles moderate motion relatively well, compromised image quality is obtained if the data for each time point is affected by strong inconsistencies due to varying motion states. For example, if during 50% of the spokes the liver was in an end-expiratory position and during the other 50% of the data in an end-inspiratory position, GRASP will not be able to find one reconstruction that is consistent with both of these motion states. As a result, the images show motion blurring and streak artifacts.

However, since GRASP is based on radial sampling, it is possible to apply additional tricks to resolve this situation. Because all of the spokes pass through the center of *k*-space, it is possible to extract a respiration curve from the *k*-space center that indicates how the patient was breathing during the examination [17]. This is possible because the percentage of (dark) lung tissue in the field-of-view changes during respiration, which leads to a modulation of the total signal power. The latter is reflected by the signal intensity at the *k*-space center, which therefore can be used to generate the respiration curve. Once it is known from the curve what the respiratory state for each acquired spoke was, the data can be sorted according to the respiratory state and the GRASP reconstruction can be extended to treat the respiratory state as an extra dimension, which allows freezing the respiration in the reconstructed images [18]. This extended approach, which we call XD-GRASP¹, is still under active development and accompanied by a further increase of the computational complexity. However, as shown in Figure 7, initial results look promising and we are convinced that the motion-compensated XD-GRASP approach is a leap towards the future of abdominopelvic DCE-MRI, soon delivering 100% reliability in every patient and at every imaging center, regardless of the

patient's cooperation and regardless of the operator's training level.

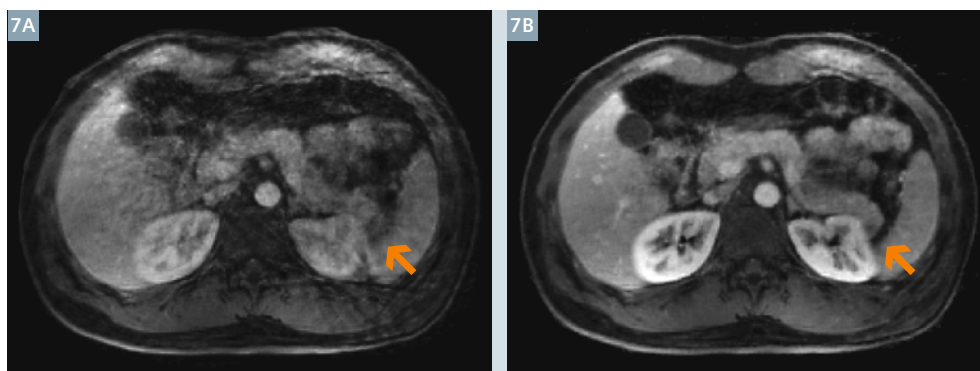
Conclusion

GRASP is a new concept to simplify DCE-MRI exams by acquiring all information using a single continuous scan instead of several individual scans, which eliminates the possibility of timing or synchronization mistakes. Because GRASP is based on radial sampling, acquisitions can be performed during free breathing, thus making abdominal DCE-MRI accessible for patients unable hold breath. Sufficiently high acquisition speed is achieved by synergistically combining the compressed-sensing and parallel-imaging principles. Due to use of the golden-angle scheme, the temporal resolution and desired image time points can be selected retrospectively, which enables reconstructing both morphologic and perfusion information from the same exam. GRASP has already been tested in thousands of patient exams in our routine practice, making it one of the first compressed-sensing techniques that have been evaluated on a large scale for clinical feasibility. While results are convincing for patients with regular breathing activity, limitations still exist for those patients performing deep respiration/coughing during the injection. This remaining issue is now being addressed by integrating active motion compensation based on the radial self-navigation principle.

References

- 1 Elsayes KM, Narra VR, Yin Y, Mukundan G, Lammle M, Brown JJ. Focal hepatic lesions: diagnostic value of enhancement pattern approach with contrast-enhanced 3D gradient-echo MR imaging. *Radiographics*. 2005 Sep-Oct;25(5):1299-1320.
- 2 Griswold MA, Jakob PM, Heidemann RM, Nittka M, Jellus V, Wang J, Kiefer B, Haase A. Generalized autocalibrating partially parallel acquisitions (GRAPPA). *Magn Reson Med*. 2002 Jun;47(6):1202-1210.
- 3 Martin DR, Sharma P, Kitajima H. Challenges and Clinical Value of Automated and Patient-Specific Dynamically Timed Contrast-Enhanced Liver MRI Examination. *Siemens MAGNETOM Flash* 3/2009:40-45.
- 4 Block KT, Chandarana H, Milla S, Bruno M, Mulholland T, Fatterpekar G, Hagiwara M, Grimm R, Geppert C, Kiefer B, Sodickson DK. Towards Routine Clinical Use of Radial Stack-of-Stars 3D Gradient-Echo Sequences for Reducing Motion Sensitivity. *J Korean Soc Magn Reson Med*. 2014 Jun;18(2):87-106.
- 5 Chandarana H, Block TK, Rosenkrantz AB, Lim RP, Kim D, Mossa DJ, Babb JS, Kiefer B, Lee VS. Free-breathing radial 3D fat-suppressed T1-weighted gradient echo sequence: a viable alternative for contrast-enhanced liver imaging in patients unable to suspend respiration. *Invest Radiol*. 2011 Oct;46(10):648-53.
- 6 Feng L, Grimm R, Block KT, Chandarana H, Kim S, Xu J, Axel L, Sodickson DK, Otazo R. Golden-angle radial sparse parallel MRI: Combination of compressed

¹ WIP, the product is currently under development and is not for sale in the US and other countries. Its future availability cannot be ensured.



7 GRASP liver exam of a patient breathing deeply after the injection. Due to the inconsistent motion state of the acquired data, the normal GRASP reconstruction (**7A**) is affected by streak artifacts and motion blurring (arrow). These artifacts are clearly reduced when employing XD-GRASP with additional motion compensation (**7B**).

- sensing, parallel imaging, and golden-angle radial sampling for fast and flexible dynamic volumetric MRI. *Magn Reson Med*. 2014 Sep;72(3):707-717.
- 7 Chandarana H, Feng L, Block TK, Rosenkrantz AB, Lim RP, Babb JS, Sodickson DK, Otazo R. Free-breathing contrast-enhanced multiphase MRI of the liver using a combination of compressed sensing, parallel imaging, and golden-angle radial sampling. *Invest Radiol*. 2013 Jan;48(1):10-16.
 - 8 Winkelmann S, Schaeffter T, Koehler T, Eggers H, Doessel O. An optimal radial profile order based on the Golden Ratio for time-resolved MRI. *IEEE Trans Med Imaging*. 2007 Jan;26(1):68-76.
 - 9 Lustig M, Donoho D, Pauly JM. Sparse MRI: The application of compressed sensing for rapid MR imaging. *Magn Reson Med*. 2007 Dec;58(6):1182-1195.
 - 10 Pruessmann KP, Weiger M, Börner P, Boesiger P. Advances in sensitivity encoding with arbitrary k-space trajectories. *Magn Reson Med*. 2001 Oct;46(4):638-651.
 - 11 Block KT, Uecker M, Frahm J. Undersampled radial MRI with multiple coils. Iterative image reconstruction using a total variation constraint. *Magn Reson Med*. 2007 Jun;57(6):1086-1098.
 - 12 Information and free download available at <http://ktblock.de/yarra>
 - 13 Chandarana H, Block TK, Ream J, Mikheev A, Sigal SH, Otazo R, Rusinek H. Estimating Liver Perfusion From Free-breathing Continuously Acquired Dynamic Gd-EOB-DTPA Enhanced Acquisition With Compressed Sensing Reconstruction. *Invest Radiol*. In press.
 - 14 Rosenkrantz AB, Geppert C, Grimm R, Block TK, Glielmi C, Feng L, Otazo R, Ream JM, Romolo MM, Taneja SS, Sodickson DK, Chandarana H. Dynamic contrast-enhanced MRI of the prostate with high spatiotemporal resolution using compressed sensing, parallel imaging, and continuous golden-angle radial sampling: Preliminary experience. *J Magn Reson Imaging*. 2014 May 16. Epub ahead of print.
 - 15 Ream JM, Doshi AM, Block KT, Kim S, Otazo R, Feng L, Chandarana H. High Spatiotemporal Dynamic Contrast-Enhanced MRI of the Small Bowel in Active Crohn's Terminal Ileitis using Compressed Sensing, Parallel Imaging, and Golden-Angle Radial Sampling. *In Proc. Intl. Soc. Mag. Reson. Med*. 22 (2014): 4292.
 - 16 Espagnet CR, Bangiyev L, Block KT, Grimm R, Feng L, Ruggiero V, Babb J, Davis A, Sodickson DK, Fatterpekar G. High resolution DCE MRI of the Pituitary gland using Radial K space Acquisition with Compressed Sensing Reconstruction. *In Proc. Intl. Soc. Mag. Reson. Med*. 22 (2014): 4669.
 - 17 Grimm R, Bauer S, Kiefer B, Hornegger J, Block KT. Optimal Channel Selection for Respiratory Self-Gating Signals. *In Proc. Intl. Soc. Mag. Reson. Med*. 21 (2013): 3749.
 - 18 Feng L, Liu J, Block KT, Xu J, Axel L, Sodickson DK, Otazo R. Compressed Sensing Reconstruction with an Additional Respiratory-Phase Dimension for Free-Breathing Imaging. *In Proc. Intl. Soc. Mag. Reson. Med*. 21 (2013): 606.



Contact

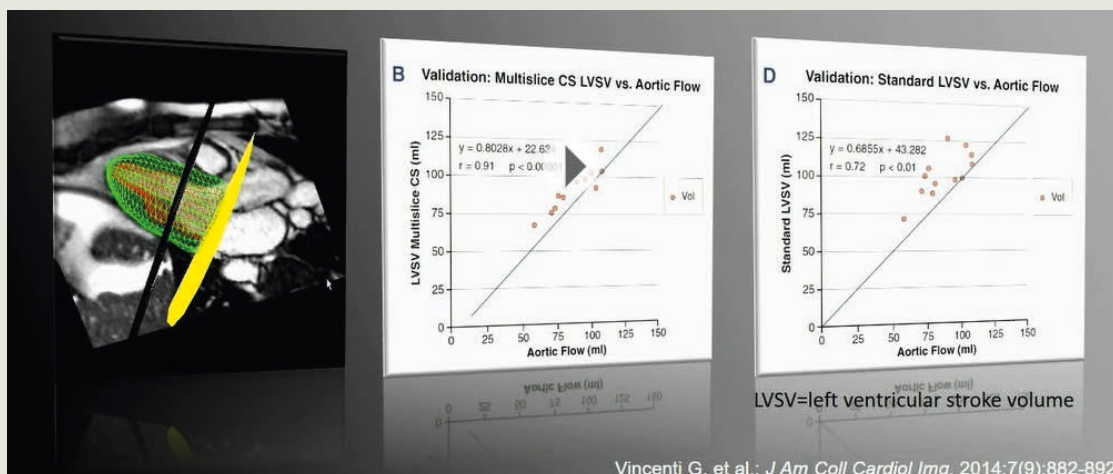
Dr. Kai Tobias Block
Center for Biomedical Imaging
NYU Langone Medical Center
660 First Avenue
New York, NY 10016
USA
tobias.block@nyumc.org

Learn more!

Listen to Professor Stuber's keynote on Compressed Sensing at

www.siemens.com/magnetom-world

go to > **Clinical Corner** > **Clinical Talks**



Matthias Stuber, Ph.D.

Centre Hospitalier Universitaire Vaudois (CHUV), Lausanne, Switzerland

Case Report: Detection of Insulinomas with High Spatiotemporal Resolution Using Compressed Sensing, Parallel Imaging, and Continuous Golden-Angle Radial Sampling

Kwadwo Antwi, M.D.¹; Damian Wild, M.D., Ph.D.¹; Emanuel Christ, M.D., Ph.D.¹; Kai Tobias Block, Ph.D.²; Tobias Heye, M.D.¹

¹ Department of Radiology and Nuclear Medicine, University Hospital Basel, Basel, Switzerland

² Department of Radiology, NYU Langone Medical Center, New York, NY, USA

Patient history

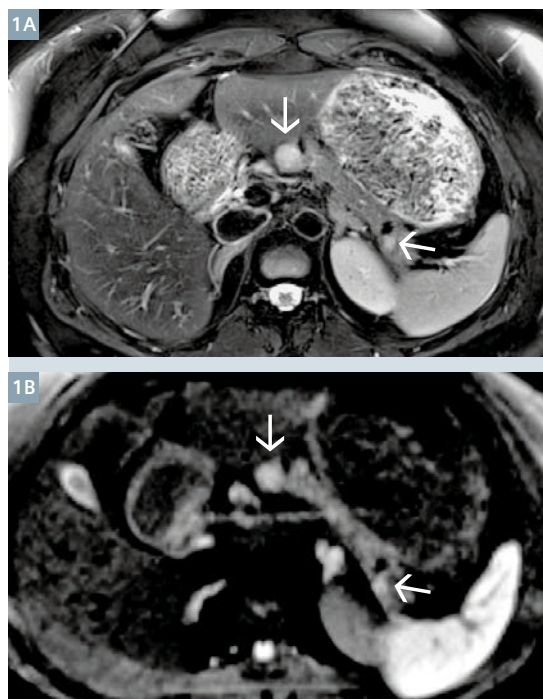
A 45-year-old female presented with recurrent episodes of aphasia, hyperhidrosis and palpitations. Known familiar predisposition led to genetic testing which revealed a germline mutation in the multiple endocrine neoplasia type 1 (MEN1) tumor suppressor gene responsible for the MEN1 syndrome. These patients are known to develop neuroendocrine tumors such as insulinomas in a high incidence [1]. Subsequent fasting test was aborted after 10 hours due to neuroglycopenic symptoms, low blood glucose levels (2.9 mmol/l), elevated insulin (6.9 pmol/l), elevated c-peptide (519 pmol/l) and as proof of an endogenous hyperinsulinism and highly suggestive for an insulinoma. Previously performed magnetic resonance imaging (MRI) and computed tomography (CT) revealed several lesions in the pancreas and duodenum.

Sequence details

Abdominal MRI acquisition was performed on a commercially available 3T system (MAGNETOM Prisma, Siemens Healthcare, Erlangen, Germany) in supine position using a multichannel body surface coil. The protocol aims for high spatial resolution and robustness with regard to breathing and motion artefacts. The body surface coil was placed firmly across the abdomen and the patient was asked to breathe in a calm and shallow way to avoid excessive abdominal excursion during breathing.

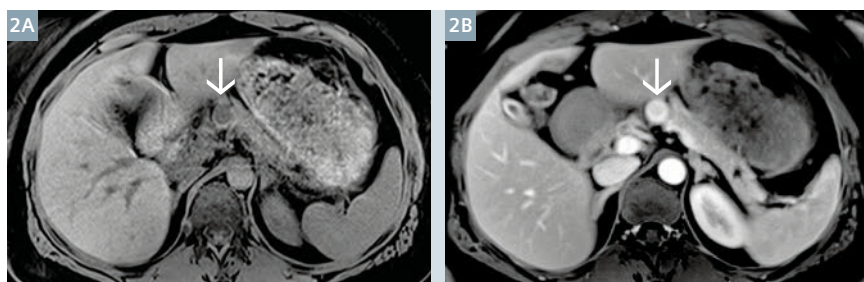
The protocol included standard sequences:

- a) Coronal half fourier acquisition single shot turbo spin echo (HASTE) localizer
- b) Coronal breath-hold T2-weighted HASTE
- c) Transverse breath-hold T2-weighted HASTE
- d) Transverse, fat-suppressed T2-weighted turbo spin echo (TSE) images in breath-hold
- e) Breath-hold in- and out-of-phase T1-weighted gradient-echo sequence
- f) Free-breathing echo planar diffusion-weighted images in the transverse plane using five b-values (0, 50, 200, 400, and 800)
- g) Transverse, free-breathing (respiratory-triggered, navigator-echo technique) fat-suppressed T2-weighted sequence
- h) Fat-suppressed, T2-weighted spin echo sequences images using periodically rotated overlapping parallel lines with enhanced reconstruction (BLADE)
- i) Fat-suppressed, T1-weighted DCE-MRI using a prototype implementation of Golden Angle Radial Sparse Parallel MRI (GRASP)¹ [8].



1 (1A) T2-weighted images depict a 16 mm lesion in the cranial portion of the pancreatic head (arrow) as well as a 6 mm lesion in the dorsal portion of the pancreatic head (arrowhead). (1B) In the diffusion-weighted images both lesions show a diffusion restriction.

¹ WIP, the product is currently under development and is not for sale in the US and in other countries. Its future availability cannot be ensured.



2 (2A) Precontrast T1-weighted images depict the 16 mm hypointense lesion in the cranial portion of the pancreatic head (arrow). The smaller lesion in the dorsal portion of the pancreatic tail is not delineated clearly. (2B) Postcontrast T1-weighted images show early arterial enhancement in the lesion in the pancreatic head (arrow). The lesion in the pancreatic tail is not delineated clearly.

GRASP is based on a fat-suppressed VIBE sequence using the 'stack-of-stars' sampling scheme, which employs radial sampling in-plane and Cartesian sampling in the slice direction [2]. A total of 1,456 radial spokes were acquired continuously using the golden angle scheme (GRASP) over the course of 3 minutes and 45 seconds, which incorporated the precontrast portion of the acquisition; the contrast administration occurred following a 20-second injection delay. Additional parameters were as follows: TR 3.48 ms; TE 1.63 ms; flip angle 12°; matrix 256 x 256; FOV 328 x 328 mm; slice thickness 2.5 mm. Dynamic injection of 0.1 mmol Dotarem (Gd-DOTA) per kilogram body weight was administered through power injector at a rate of 3 ml/s followed by a 20 ml saline flush also at a rate of 3 ml/s. The GRASP dataset can then be sent to a dedicated processing server allowing to set the preferred temporal

resolution, starting from 2 s temporal resolution. A retrospective gating algorithm can be applied to the data processing which rejects 50% of the raw data and keeps the remaining 50% at the lowest position of the diaphragm during expiration.

Imaging findings

A 16 mm lesion is visualized in the cranial portion of the pancreatic body – which is hypointense in T1-weighted images, hyperintense in T2-weighted images, and hyperintense in diffusion-weighted images – shows an early arterial enhancement and venous pooling after contrast media application. Another 6 mm lesion is visualized in the dorsal portion of the pancreatic tail which is hypointense in T1-weighted images, hyperintense in T2-weighted images, and slightly hyperintense in diffusion-weighted images, and shows

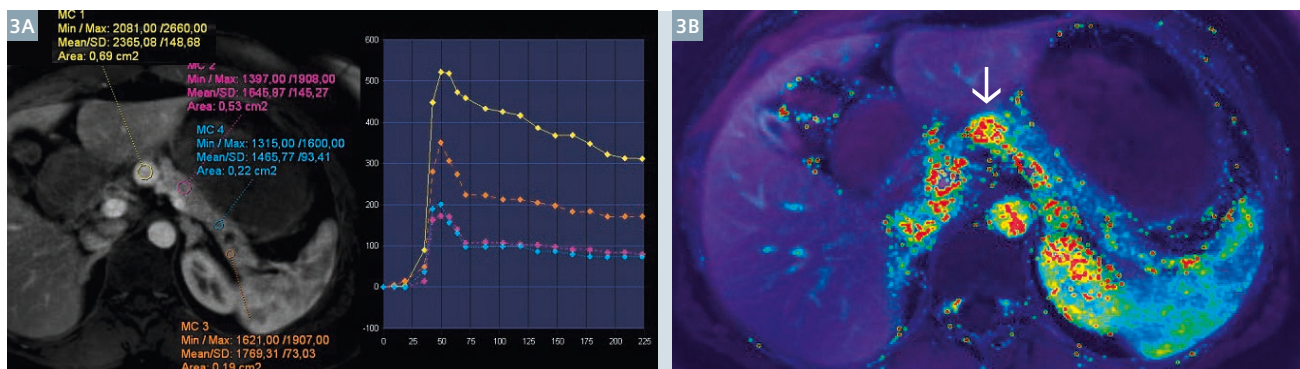
a faint arterial enhancement with venous pooling after contrast media application.

Figure 4 shows continuous imaging with GRASP (Golden-angle Radial Sparse Parallel) starting 20 seconds before injection and ending in the late portal venous phase. Assessment is performed via a region-of-interest placed in the lesions. As reference, a region-of-interest is placed in the proximal and middle portion of the tail. This quantitatively depicts early arterial enhancement and venous pooling of the lesions in comparison to normal pancreatic parenchyma in the tail.

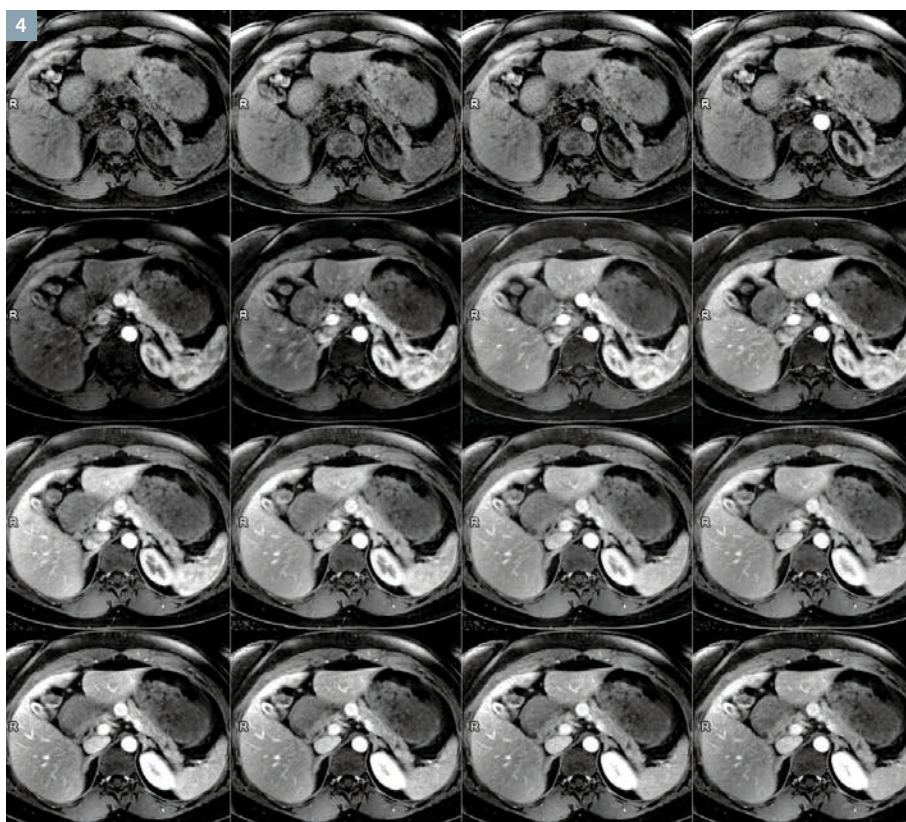
Discussion

Insulinomas are small tumors, usually < 2 cm at presentation [3, 4] predominantly located in the pancreas. As neuroendocrine tumors, a large proportion exhibits an enhancement after contrast media application. The assessment of arterial and venous phases aids lesion detection, characterization and differentiation from normal pancreas parenchyma. The trade-off between spatial and temporal resolution in the detection of these small tumors presents a challenge in dynamic contrast-enhanced MRI.

3-dimensional fat-suppressed T1-weighted interpolated spoiled gradient-echo (VIBE, volumetric interpolated breath-hold examination) sequences are the conventional sequences widely used for contrast-enhanced MR examinations of the



3 (3A) Signal over time evaluation based on mean curve ROIs: A region-of-interest is placed in the lesion in the pancreatic head (yellow) and pancreatic tail (orange). Reference regions-of-interest are placed in the pancreatic tail (purple + blue). The lesion in the pancreatic head and tail shows early arterial enhancement in comparison to normal pancreatic parenchyma. (3B) Color maps with dynamic contrast information.



4 Contrast enhancement changes over time displayed on GRASP datasets, each calculated to represent a temporal resolution of 8 seconds with retrospective gating only including 50% of the data based on the lowest position of expiration.

liver and pancreas [5]. Motion artifacts, such as respiratory motion, cardiac pulsation and bowel peristalsis, however, limit the detectability of small lesions as well as vascularization characterisation and can even render images nondiagnostic [6].

With GRASP a high temporal resolution can be achieved by using Compressed Sensing which exploits spatial correlation within images or spatiotemporal correlations among sequentially acquired images [7]. Thus, in combination with parallel imaging, continuous golden-angle sampling and retrospective gating offers both the high temporal and spatial resolution as depicted in Figures 3 and 4.

This case demonstrates that high spatiotemporal resolution dynamic contrast-enhanced pancreas MRI is possible with GRASP. It has the potential to improve image quality and lesion depiction compared to standard dynamic contrast-enhanced MRI.

References

- 1 Lairmore, T. C. et al. Clinical genetic testing and early surgical intervention in patients with multiple endocrine neoplasia type 1 (MEN 1). *Ann. Surg.* 239, 637–45; discussion 645–7 (2004).
- 2 Chandarana H. et al. Free-breathing radial 3D fat-suppressed T1-weighted gradient echo sequence: a viable

alternative for contrast-enhanced liver imaging in patients unable to suspend respiration. *Invest Radiol.* 2011 Oct; 46(10):648-53.

- 3 Mehrabi, A. et al. A systematic review of localization, surgical treatment options, and outcome of insulinoma. *Pancreas* 43, 675–86 (2014).
- 4 Liu, H. et al. Strategy for the surgical management of insulinomas: Analysis of 52 cases. *Dig. Surg.* 24, 463–468 (2008).
- 5 Thng, C. H. Perfusion magnetic resonance imaging of the liver. *World J. Gastroenterol.* 16, 1598 (2010).
- 6 Ehman, R. L. et al. Influence of physiologic motion on the appearance of tissue in MR images. *Radiology* 159, 777–82 (1986).
- 7 Lustig, M., Donoho, D. & Pauly, J. M. Sparse MRI: The application of compressed sensing for rapid MR imaging. *Magn. Reson. Med.* 58, 1182–95 (2007).
- 8 Feng L, Grimm R, Block KT, Chandarana H, Kim S, Xu J, Axel L, Sodickson DK, Otazo R. Golden-angle radial sparse parallel MRI: Combination of compressed sensing, parallel imaging, and golden-angle radial sampling for fast and flexible dynamic volumetric MRI. *Magn Reson Med.* 2014 Sep;72(3):707-717.
- 9 Block KT, Sodickson DK et al. GRASP: Tackling the Challenges of Abdominopelvic DCE-MRI. *MAGNETOM Flash* 60, 5/2014, 16-22.

Contact

Kwadwo Antwi, M.D.
Department of Radiology and Nuclear Medicine
University Hospital Basel
Petersgraben 4
4031 Basel
Switzerland
Phone: +41 61 32 86684
kwadwo.antwi@ubs.ch
<http://radiologie.unibas.ch>



Permeability Imaging of Parotid Tumors with Golden-Angle Radial Sparse Parallel MR Imaging (GRASP)

Sohil H. Patel, M.D.¹; Hersh Chandarana, M.D.¹; Kai Tobias Block, Ph.D.¹; Robert Grimm, Ph.D.²; Girish Fatterpekar, M.D.¹

¹ Department of Radiology, NYU Langone Medical Center, New York, NY, USA

² Siemens Healthineers, Erlangen, Germany

Introduction

A range of pathologic processes may affect the parotid gland. These vary from benign processes such as reactive lymph nodes, pleomorphic adenoma, and Warthin's tumor, to malignancies such as adenocarcinoma, adenoid cystic carcinoma, and mucoepidermoid carcinoma. Neoplasms of the parotid gland can pose a diagnostic challenge because conventional imaging features cannot differentiate benign from malignant lesions with complete certainty [1]. In conventional MRI examinations, most neoplasms of the parotid gland enhance with intravenous contrast. Therefore, the presence of enhancement, while essential to the identification and mapping of parotid neoplasms, does not differentiate between different

tumor subtypes. To further obfuscate clinical management, the most common benign tumor of the parotid gland (pleomorphic adenoma) can occasionally dedifferentiate into a malignant tumor [2]. Moreover, the accuracy of fine needle biopsy of parotid neoplasms can occasionally be limited due to sampling errors [3].

GRASP

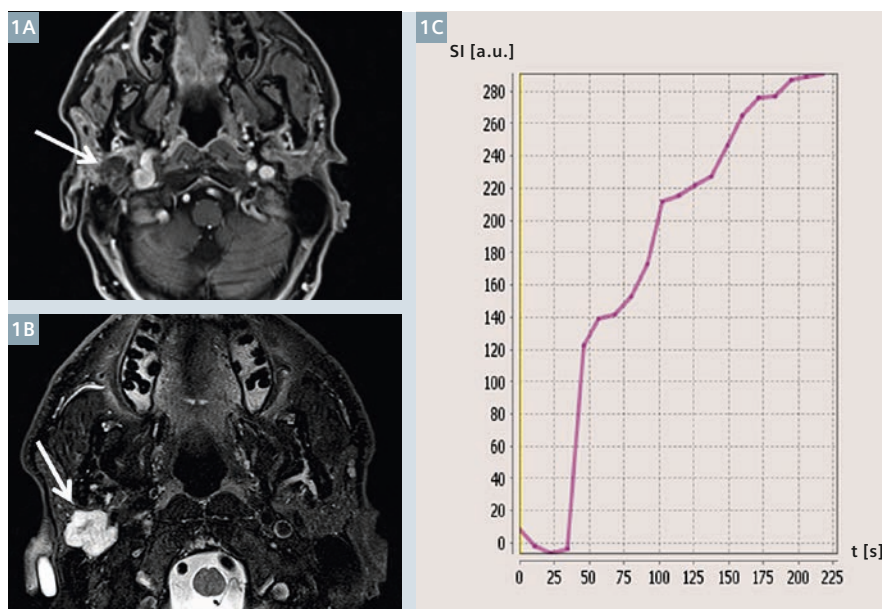
Golden-Angle Radial Sparse Parallel MR Imaging (GRASP)¹ is a novel imaging technique that combines golden-angle radial stack-of-stars sampling with a Compressed Sensing reconstruction [4], enabling motion-robust imaging at high spatial and temporal resolution. GRASP allows

a characterization of the dynamic contrast curve of parotid tumors. Numerous features of the contrast curve can be easily assessed, such as the wash-in and wash-out contrast slopes, the time-to-maximum-enhancement, area under the curve, and peak enhancement. Each of these features may differ amongst various parotid neoplasms, and provide an additional non-invasive method of interrogating parotid neoplasms. In addition, GRASP produces high-resolution, fat-suppressed images with excellent motion robustness allowing for precise localization and mapping of parotid neoplasms.

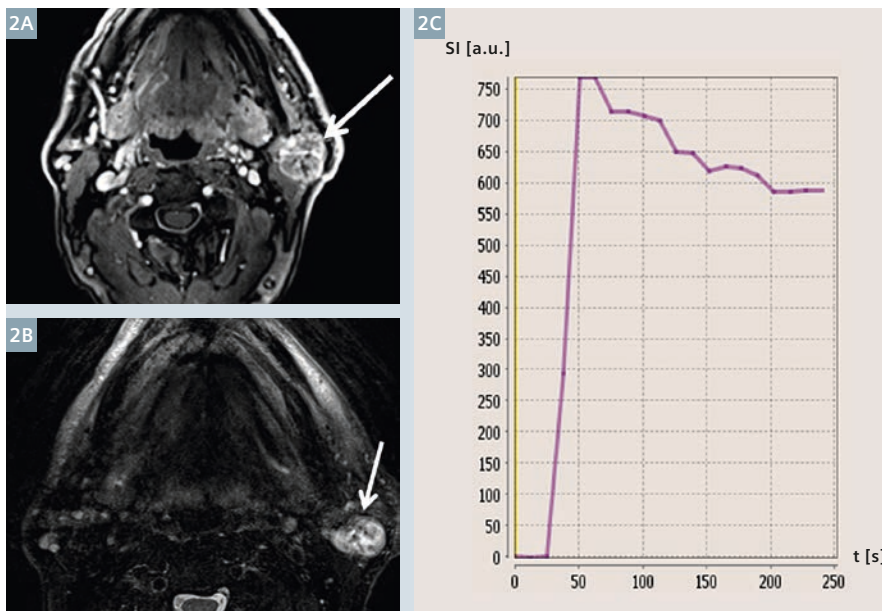
Clinical cases

Two cases are included for illustration. Figure 1 shows GRASP imaging data of a parotid mass in a 67-year-old male.

¹ GRASP is still under development and not commercially available yet. Its future availability cannot be ensured.



1 67-year-old male patient with a right parotid pleomorphic adenoma. (1A) Composite GRASP image shows a lobulated mass in the right parotid gland demonstrating mild enhancement (arrow). (1B) T2-weighted imaging demonstrates hyperintense signal in the lesion (arrow). (1C) Dynamic contrast curve shows continuous gradual wash-in of contrast material during the image acquisition.



- 2 68-year-old male patient with a left parotid Warthin's tumor. (2A) Composite GRASP image shows a lobulated mass in the left parotid gland demonstrating moderate enhancement (arrow). (2B) T2-weighted imaging demonstrates predominantly hyperintense signal in the lesion (arrow). (2C) Dynamic contrast curve shows steep wash-in slope, sharp early peak of contrast enhancement, and more gradual wash-out of contrast material.

Figure 1A is a high-resolution post-contrast image demonstrating that the mass has mild heterogeneous enhancement, and contains lobulated margins. Figure 1B shows that the lesion is hyperintense on T2-weighted imaging. Figure 1C demonstrates the dynamic contrast curve after processing of the GRASP data. The contrast curve demonstrates a gradual and continuously rising wash-in of contrast material. The imaging appearance and contrast curve characteristics were consistent with a pleomorphic adenoma [5], and this proved to be the case on pathologic analysis.

Figure 2 shows GRASP imaging data of a left parotid mass in a 68-year-old male. Figure 2A shows that the mass demonstrates moderately avid heterogeneous enhancement, and contains lobulated margins. Figure 2B shows that the lesion is predominantly hyperintense on T2-weighted imaging. Figure 2C demonstrates the dynamic contrast curve, which is strikingly different than the case shown in Figure 1. In this case, the contrast curve shows a sharp wash-in, an early peak, and relatively early wash-out of contrast material. Though the conventional imaging characteristics in this case were non-specific, the contrast curve was characteristic of a Warthin's tumor [5], which proved to be the case upon pathologic analysis.

Conclusion

Improving the diagnostic specificity in assessing parotid neoplasms is only one among many potential applications for GRASP in the head and neck. Examples include assessment of lymph node status in cancer patients, differentiation of tumor recurrence from inflammation in treated patients, or differentiation of tumor types in other organs of the head and neck. At our institution, GRASP is performed in all of our clinical head and neck MRI scans, and it routinely impacts on our diagnostic performance.

References

- Christe A, Waldherr C, Hallett R, Zbaeren P, Thoeny H. MR imaging of parotid tumors: typical lesion characteristics in MR imaging improve discrimination between benign and malignant disease. *AJNR American journal of neuroradiology*. 2011;32(7):1202-7. doi:10.3174/ajnr.A2520.
- Antony J, Gopalan V, Smith RA, Lam AK. Carcinoma ex pleomorphic adenoma: a comprehensive review of clinical, pathological and molecular data. *Head and neck pathology*. 2012;6(1):1-9. doi:10.1007/s12105-011-0281-z.
- Daneshbod Y, Daneshbod K, Khademi B. Diagnostic difficulties in the interpretation of fine needle aspirate samples in salivary lesions: diagnostic pitfalls revisited. *Acta cytologica*. 2009;53(1):53-70.
- Feng L, Grimm R, Block KT, Chandarana H, Kim S, Xu J, Axel L, Sodickson DK, Otazo R. Golden-angle radial sparse parallel MRI: combination of compressed sensing, parallel imaging, and golden-angle radial sampling for fast and flexible dynamic volumetric MRI. *Magn Reson Med*. 2014.
- Dong Y, Lei GW, Wang SW, Zheng SW, Ge Y, Wei FC. Diagnostic value of CT perfusion imaging for parotid neoplasms. *Dento maxillo facial radiology*.
- Chandarana H, Feng L, Block TK, Rosenkrantz AB, Lim RP, Babb JS, Sodickson DK, Otazo R. Free-breathing contrast-enhanced multiphase MRI of the liver using a combination of compressed sensing, parallel imaging, and golden-angle radial sampling. *Invest Radiol* 2013 Jan;48(1):10-6.
- Chandarana H, Block TK, Ream J, Mikheev A, Sigal SH, Otazo R, Rusinek H. Estimating liver perfusion from free-breathing continuously acquired dynamic gadolinium-ethoxybenzyl-diethylenetriamine pentaacetic acid-enhanced acquisition with compressed sensing reconstruction. *Invest Radiol*. 2015 Feb;50(2):88-94. 2014;43(1):20130237. doi:10.1259/dmfr.20130237.

Contact

Sohil H. Patel, M.D.
Department of Radiology
New York University
Langone Medical Center
660 1st Ave
New York, NY 10016
USA
sohil.patel@nyumc.org

Free-breathing DCE-MRI of the Kidney using GRASP

Philipp Riffel¹, Kai Tobias Block²

¹ Institute of Clinical Radiology and Nuclear Medicine, University Medical Center Mannheim, University of Heidelberg, Germany

² Center for Advanced Imaging Innovation and Research (CAI²R), Department of Radiology, New York University School of Medicine, New York, NY, USA

Challenges in abdominal DCE-MRI

Dynamic Contrast-Enhanced Magnetic Resonance Imaging (DCE-MRI) is a relevant part of standard renal MRI examination and indispensable for the evaluation of renal pathologies, such as renal masses [1-4]. It also enables the measurement of renal perfusion as well as glomerular filtration rate (GFR), since gadolinium-based contrast agents are excreted almost only by the kidneys [5-11]. However DCE-MRI exams remain challenging and the failure rates are undesirably high. Especially in sick patients unable to hold their breath adequately, respiratory-motion artifacts compromise achievable image quality. Another challenge is the tradeoff between spatial and temporal resolution of DCE-MRI data for measuring perfusion parameters [12, 13]. On the one hand, a high spatial resolution without motion artifacts is beneficial for a diagnostic image

quality of morphological images. On the other hand, a high temporal resolution (less than 4 s per volume) is desirable for an accurate calculation of perfusion parameters [13].

Solution approaches

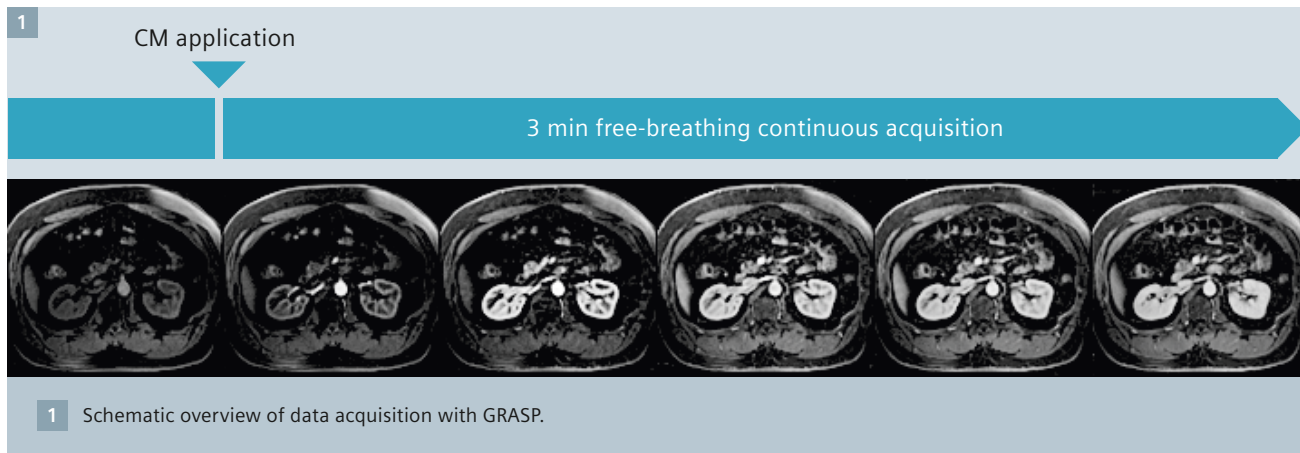
For acceleration of image acquisition, several parallel imaging techniques, such as generalized autocalibrating partially parallel acquisition (GRAPPA) or controlled aliasing in parallel imaging results in higher acceleration (CAIPRINHA) are available. However, the inverse correlation of the acceleration factor and signal-to-noise ratio (SNR) leads to a loss in SNR. Additionally, several techniques have been introduced to reduce respiratory-motion artifacts and to manage the tradeoff between spatial and temporal resolution such as keyhole [14], k-t broad-use linear acquisition speed-up technique (k-t BLAST) [15] and time-resolved angiography with stochastic trajectories (TWIST) [16].

The GRASP approach

The recent introduction of a new approach, golden-angle radial sparse parallel MRI (GRASP)¹ [17, 18], could potentially address all of the above mentioned issues. By using non-Cartesian acquisition techniques, specifically radial *k*-space sampling, motion-induced ghosting artifacts can be reduced. The radial sampling is performed using the golden-angle radial sampling scheme for a flexible spatiotemporal resolution [18].

To improve the temporal resolution and to suppress undersampling artifacts, iterative reconstruction with through-time total variation regularization is applied. A 2016 study showed that multiphase MRI of the kidney is a suitable candidate for the application of GRASP [17], probably because of the high amount of spatiotemporal data correlations, which is a premise for the application of that technique.

¹ WIP, GRASP is currently under development and is not for sale in the US and in other countries. Its future availability cannot be ensured.



Improved workflow and increased efficiency

As data are acquired continuously with a native phase prior to contrast medium (CM) application (Fig. 1), timing and synchronization errors are no longer possible. Acquiring all information using a single continuous scan instead of several individual scans simplifies workflow even further.

Full flexibility by retrospective choice of temporal resolution

With GRASP, data are acquired continuously during free-breathing. The sampling scheme uses the golden angle as radial increment, which allows that basically any number of radial spokes can be combined into an image providing the possibility to retrospectively decide which temporal resolution should be reconstructed. For morphological images, a poorer temporal resolution (e.g. 55 spokes per image for a temporal resolution of 6.2 seconds) can be reconstructed. For perfusion assessment, images can be reconstructed from the same data set with 13 spokes per image, resulting in a temporal resolution of 1.5 seconds (Fig. 2).

Role model for the combination of morphological and functional imaging

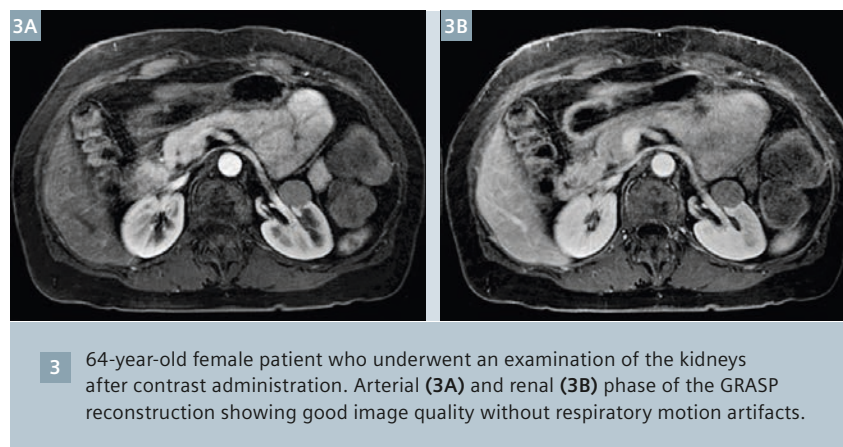
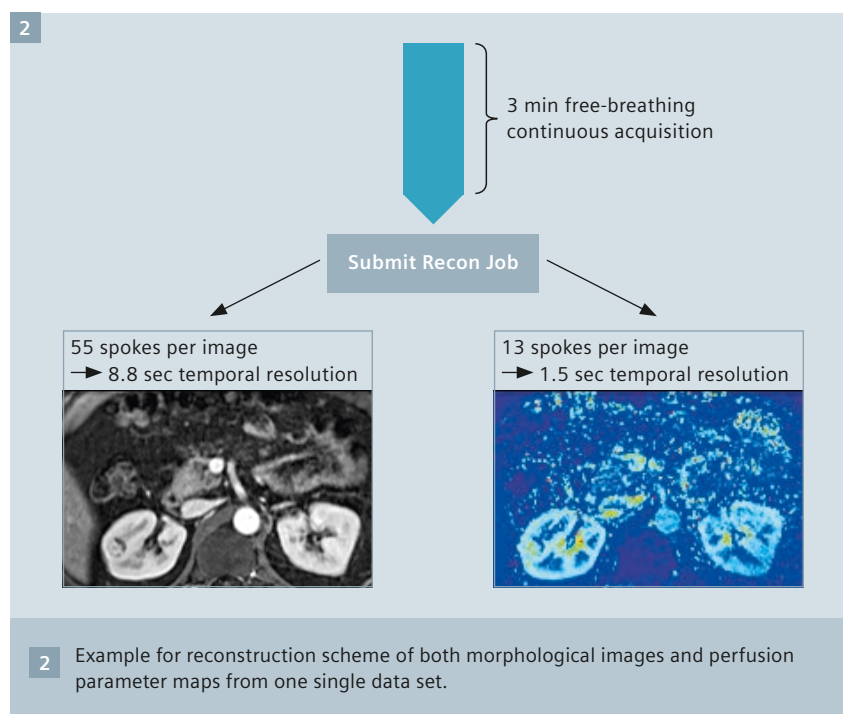
One major strength of MRI is the possibility of acquiring both morphologic and functional information. Perfusion imaging thus represents a cornerstone of functional imaging and is critical for achieving greater diagnostic specificity in terms of lesion characterization and assessment of organ function. The GRASP technique is an excellent example of the combination of morphological and functional imaging and shows considerable potential for overcoming some of the inherent

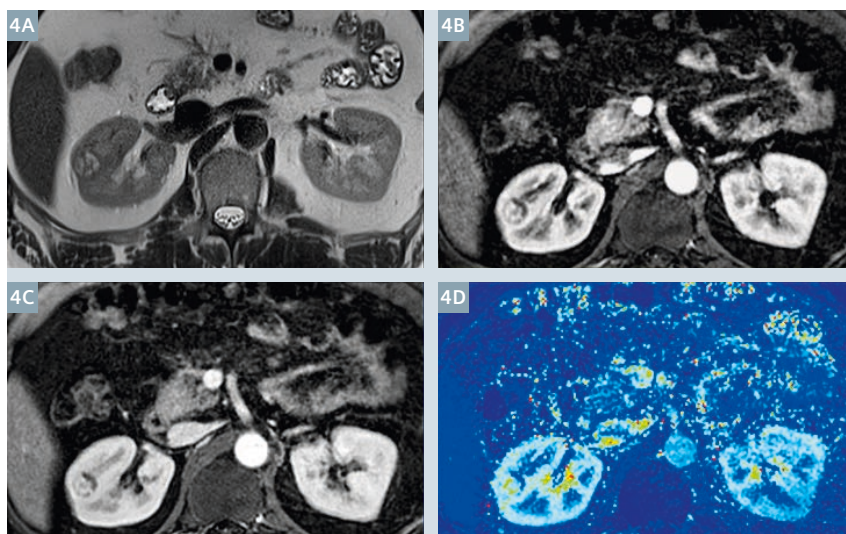
limitations of conventional DCE-MRI. In particular, the technique delivers an overall good image quality and high diagnostic confidence of morphological images (Fig. 3) [17]. Due to use of radial k -space sampling, motion-induced ghosting artifacts are minimal although data is acquired during free-breathing.

Additionally, the motion insensitive technique has been shown to be a

valuable tool to achieve valid and reproducible perfusion parameter maps (Fig. 4) [17].

In conclusion, this technique has the potential to become an integral part of renal MRI. The combination of morphological imaging and functional imaging helps to further entrench MRI as a qualitative and quantitative imaging modality.





4 48-year-old male patient with histologically proven clear cell RCC. T2w HASTE sequence (4A), arterial (4B) and renal (4C) phase of the GRASP reconstruction, estimated renal plasma flow (RPF) parameter map (4D) showing hypervascularity of the lesion.

References

- Scialpi M, Brunese L, Pisciolli I, et al. Dynamic contrast-enhanced MR imaging for differentiation of renal cell carcinoma subtypes: myth or reality? *Radiology*. 2009;252:929; author reply 30-1. doi:10.1148/radiol.2523090695.
- Sun MR, Ngo L, Genega EM, et al. Renal cell carcinoma: dynamic contrast-enhanced MR imaging for differentiation of tumor subtypes--correlation with pathologic findings. *Radiology*. 2009;250:793-802. doi:10.1148/radiol.2503080995.
- Ho VB, Allen SF, Hood MN, et al. Renal masses: quantitative assessment of enhancement with dynamic MR imaging. *Radiology*. 2002;224:695-700. doi:10.1148/radiol.2243011048.
- Notohamiprodjo M, Sourbron S, Staehler M, et al. Measuring perfusion and permeability in renal cell carcinoma with dynamic contrast-enhanced MRI: a pilot study. *J Magn Reson Imaging*. 2010;31:490-501. doi:10.1002/jmri.22028.
- Kang SK, Huang WC, Wong S, et al. Dynamic contrast-enhanced magnetic resonance imaging measurement of renal function in patients undergoing partial nephrectomy: preliminary experience. *Invest Radiol*. 2013;48:687-92. doi:10.1097/RLI.0b013e3182909e7b.
- Wentland AL, Sadowski EA, Djamali A, et al. Quantitative MR measures of intrarenal perfusion in the assessment of transplanted kidneys: initial experience. *Acad Radiol*. 2009;16:1077-85. doi:10.1016/j.acra.2009.03.020.
- Ludemann L, Nafz B, Elsner F, et al. Absolute quantification of regional renal blood flow in swine by dynamic contrast-enhanced magnetic resonance imaging using a blood pool contrast agent. *Invest Radiol*. 2009;44:125-34. doi:10.1097/RLI.0b013e318193598c.
- Michaely HJ, Herrmann KA, Nael K, et al. Functional renal imaging: nonvascular renal disease. *Abdom Imaging*. 2007;32:1-16. doi:10.1007/s00261-005-8004-0.
- Grenier N, Hauger O, Cimpean A, et al. Update of renal imaging. *Semin Nucl Med*. 2006;36:3-15. doi:10.1053/j.semnuclmed.2005.08.001.
- Vallee JP, Lazeyras F, Khan HG, et al. Absolute renal blood flow quantification by dynamic MRI and Gd-DTPA. *Eur Radiol*. 2000;10:1245-52. doi:10.1007/s003300000434.
- Sourbron SP, Michaely HJ, Reiser MF, et al. MRI-measurement of perfusion and glomerular filtration in the human kidney with a separable compartment model. *Invest Radiol*. 2008;43:40-8. doi:10.1097/RLI.0b013e31815597c5.
- Kuhl CK, Schild HH, Morakkabati N. Dynamic bilateral contrast-enhanced MR imaging of the breast: trade-off between spatial and temporal resolution. *Radiology*. 2005;236:789-800. doi:10.1148/radiol.2363040811.
- Michaely HJ, Sourbron SP, Buettner C, et al. Temporal constraints in renal perfusion imaging with a 2-compartment model. *Invest Radiol*. 2008;43:120-8. doi:10.1097/RLI.0b013e3181583b0c.
- van Vaals JJ, Brummer ME, Dixon WT, et al. "Keyhole" method for accelerating imaging of contrast agent uptake. *J Magn Reson Imaging*. 1993;3:671-5.
- Tsao J, Boesiger P, Pruessmann KP. k-t BLAST and k-t SENSE: dynamic MRI with high frame rate exploiting spatiotemporal correlations. *Magn Reson Med*. 2003;50:1031-42. doi:10.1002/mrm.10611.
- Herrmann KH, Baltzer PA, Dietzel M, et al. Resolving arterial phase and temporal enhancement characteristics in DCE MRM at high spatial resolution with TWIST acquisition. *J Magn Reson Imaging*. 2011;34:973-82. doi:10.1002/jmri.22689.
- Riffel P, Zoellner FG, Budjan J, et al. "One-Stop Shop": Free-Breathing Dynamic Contrast-Enhanced Magnetic Resonance Imaging of the Kidney Using Iterative Reconstruction and Continuous Golden-Angle Radial Sampling. *Invest Radiol*. 2016. doi:10.1097/RLI.0000000000000299.
- Chandarana H, Feng L, Block TK, et al. Free-breathing contrast-enhanced multiphase MRI of the liver using a combination of compressed sensing, parallel imaging, and golden-angle radial sampling. *Invest Radiol*. 2013;48:10-6. doi:10.1097/RLI.0b013e318271869c.

Contact

Philipp Riffel, M.D.
Institute of Clinical Radiology and Nuclear Medicine
University Medical Center Mannheim
Medical Faculty Mannheim – University Heidelberg
Theodor-Kutzer-Ufer 1-3
68167 Mannheim
Germany
Phone: +49 621 383 2067
Fax: +49 621 383 3817
Philipp.Riffel@umm.de



The entire editorial staff at Siemens Healthineers extends their appreciation to all the radiologists, technologists, physicists, experts and scholars who donate their time and energy – without payment – in order to share their expertise with the readers of MAGNETOM Flash.

MAGNETOM Flash – Imprint

© 2016 by Siemens Healthcare GmbH,
All Rights Reserved

Publisher:

Siemens Healthcare GmbH
Magnetic Resonance,
Karl-Schall-Straße 6, D-91052 Erlangen,
Germany

Editor-in-chief:

Antje Hellwich
(antje.hellwich@siemens.com)

Editorial Board:

Reto Merges; Wellesley Were;
Sunil Kumar S.L., Ph.D.;
Gary R. McNeal, MS (BME)

Review Board:

Lisa Chuah, Ph.D.; Christoph Forman;
Berthold Kiefer, Ph.D.; Edgar Müller;
Heiko Meyer, Ph.D., Michaela Schmidt;
Gregor Thörmer, Ph.D.

Production:

Norbert Moser,
Siemens Healthcare GmbH

Layout:

Agentur Baumgärtner,
Friedrichstraße 4, D-90762 Fürth,
Germany

Printer:

G. Peschke Druckerei GmbH,
Taxetstraße 4,
D-85599 Parsdorf b. Munich,
Germany

Note in accordance with § 33 Para.1 of the German Federal Data Protection Law: Despatch is made using an address file which is maintained with the aid of an automated data processing system.

MAGNETOM Flash is sent free of charge to Siemens MR customers, qualified physicians, technologists, physicists and radiology departments throughout the world. It includes reports in the English language on magnetic resonance: diagnostic and therapeutic methods and their application as well as results and experience gained with corresponding systems and solutions. It introduces from case to case new principles and procedures and discusses their clinical potential. The statements and views of the authors in the individual contributions do not necessarily reflect the opinion of the publisher.

The information presented in these articles and case reports is for illustration only and is not intended to be relied upon by the reader for instruction as to the practice of medicine. Any health care practitioner reading this information is reminded that they must use their own learning, training and expertise in dealing with their individual patients. This material does not substitute for that duty and is not intended by Siemens Healthcare to be used for any purpose in that regard. The drugs and doses mentioned herein are consistent with the approval labeling for uses and/or indications of the drug. The treating

physician bears the sole responsibility for the diagnosis and treatment of patients, including drugs and doses prescribed in connection with such use. The Operating Instructions must always be strictly followed when operating the MR system. The sources for the technical data are the corresponding data sheets. Results may vary.

Partial reproduction in printed form of individual contributions is permitted, provided the customary bibliographical data such as author's name and title of the contribution as well as year, issue number and pages of MAGNETOM Flash are named, but the editors request that two copies be sent to them. The written consent of the authors and publisher is required for the complete reprinting of an article.

We welcome your questions and comments about the editorial content of MAGNETOM Flash. Please contact us at magnetomworld.med@siemens.com.

Manuscripts as well as suggestions, proposals and information are always welcome; they are carefully examined and submitted to the editorial board for attention. MAGNETOM Flash is not responsible for loss, damage, or any other injury to unsolicited manuscripts or other materials. We reserve the right to edit for clarity, accuracy, and space. Include your name, address, and phone number and send to the editors, address above.

MAGNETOM Flash is also available online:

www.siemens.com/magnetom-world

On account of certain regional limitations of sales rights and service availability, we cannot guarantee that all products included in this brochure are available through the Siemens sales organization worldwide. Availability and packaging may vary by country and is subject to change without prior notice. Some/All of the features and products described herein may not be available in the United States.

The information in this document contains general technical descriptions of specifications and options as well as standard and optional features which do not always have to be present in individual cases, and which

may not be commercially available in all countries. Due to regulatory reasons their future availability cannot be guaranteed. Please contact your local Siemens organization for further details.

Siemens reserves the right to modify the design, packaging, specifications, and options described herein without prior notice. Please contact your local Siemens sales representative for the most current information.

Note: Any technical data contained in this document may vary within defined tolerances. Original images always lose a certain amount of detail when reproduced.

Not for distribution in the US

Siemens Healthineers Headquarters

Siemens Healthcare GmbH
Henkestr. 127
91052 Erlangen
Germany
Phone: +49 9131 84-0
[siemens.com/healthineers](https://www.siemens.com/healthineers)